

# UC Riverside

## UC Riverside Electronic Theses and Dissertations

### Title

Hybrid Molecule-Nanocrystal Photon Upconversion Across the Visible and Near-Infrared

### Permalink

<https://escholarship.org/uc/item/1bb3z0sc>

### Author

Huang, Zhiyuan

### Publication Date

2017

Peer reviewed|Thesis/dissertation

UNIVERSITY OF CALIFORNIA  
RIVERSIDE

Hybrid Molecule-Nanocrystal Photon Upconversion Across the Visible and Near-  
Infrared

A Dissertation submitted in partial satisfaction  
of the requirements for the degree of

Doctor of Philosophy

in

Chemistry

by

Zhiyuan Huang

September 2017

Dissertation Committee:

Dr. Ming Lee Tang, Chairperson

Dr. Yadong Yin

Dr. Chia-en Chang

Copyright by  
Zhiyuan Huang  
2017

The Dissertation of Zhiyuan Huang is approved:

---

---

---

Committee Chairperson

University of California, Riverside

## Acknowledgement

I'm really excited about the accomplishment of my five-year Ph.D. study. This is an unforgettable experience full of challenges, excitement, struggling, happiness. It is amazing to work with my advisor and lab mates in UC Riverside. I have learnt a lot from this experience both as a scientist, and on a personal level, and it will be the memory of my whole life. Here, I would like to appreciate people who have helped me so much throughout my Ph.D. study.

First, I would like to sincerely appreciate the help from my advisor Dr. Ming Lee Tang. Thanks for offering me the opportunity to work in this lab, and training me on both experimental techniques and the logical thinking needed to accomplish a research project. Her being knowledgeable in expertise helps me solve numerous problems I have met in my research, and her diligence and passions for your work motivates me greatly every day. She showed me the critical thinking and endeavor a qualified scientist should have.

I would like to thank my committee members, Dr. Yadong Yin and Dr. Chia-en Chang. They gave me valuable suggestions in my research. I want to thank Dr. De-en Jiang and Dr. Ming Liu, who are the committee members of my qualifying exam. Thanks for their useful comments and good questions during the exam.

I want to thank all my lab mates who provided me a lot of help in my research. They are Xin Li, Melika Mahboub, Pan Xia, Emily Moses, Daryl Hawks, Carter Gerck,

Narek Megerdich, Beverly Ru, and Helen Thayer, and all the alumni who have helped me both in lab and daily life. It's so great making friends and working with them.

I would like to thank all my collaborators from whom I have learnt a lot. They are Dr. Chris Bardeen, Dr. Tianquan Lian, Dr. Troy Van Voorhis, Dr. Val Vullev, Dr. Dimtry Fishman, Dr. Hill Harman, Dr. Juchen Guo, Dr. David Bocian, Zihao Xu, Alex Fast, Alex Kohn, and Nadav Geva, Linxiao Geng, Jordan Taylor, and Dr. Jieying Jiao. Thanks for teaching me the knowledge in the field that I was not familiar with, and showing me the experimental techniques with patience.

Last but not least, I want to show my appreciation to my families. Thank my dad Yongxiang Huang and my mom Lixin Cui. Thanks for giving me life, love and raising me up. Thanks for their unconditional support on all the decisions I made. Without their love, tolerance and encouragement I wouldn't be able to make it.

### Acknowledgement of previously published material

1. Chapter 1 has been published in “Huang, Z.; Tang, M. L. *J. Am. Chem. Soc.* **2017**, *139*, 9412”.
2. Chapter 2 has been published in “Huang, Z.; Li, X.; Mahboub, M.; Hanson, K. M.; Nichols, V. M.; Le, H. Tang, M. L.; Bardeen, C. J. *Nano Lett.* **2015**, *15*, 5552”.
3. Chapter 3 has been published in “Huang, Z.; Simpson, D. E.; Mahboub, M.; Li, X. Tang, M. L. *Chem. Sci.* **2016**, *7*, 4104”.
4. Chapter 4 has been published in “Huang, Z.; Li, X.; Yip, B. D.; Rubalcava, J. M.; Bardeen, C. J.; Tang, M. L. *Chem. Mater.* **2015**, *27*, 7503”.
5. Chapter 8 is referred from the supporting information of the above 4 publications.

## ABSTRACT OF THE DISSERTATION

Hybrid Molecule-Nanocrystal Photon Upconversion Across the Visible and Near-Infrared

by

Zhiyuan Huang

Doctor of Philosophy, Graduate Program in Chemistry  
University of California, Riverside, September 2017  
Dr. Ming Lee Tang, Chairperson

The sequential absorption of two low energy photons, followed by the emission of one higher energy photon, is known as photon upconversion. This two-photon process has potential applications in biological imaging, solar energy conversion and photocatalysis etc. Two existing strategies to realize upconversion are an inorganic system based on lanthanide doping, and an organic system based on triplet-triplet annihilation. This dissertation introduces a novel hybrid molecule-nanocrystal system that upconverts photons across visible to near-infrared. It combines the advantages of high photostability and low excitation intensity, and overcomes the limits in the previous systems. Here, the absorption of low energy photons by the semiconductor nanocrystals (NCs) is followed by the energy transfer to molecular triplet states. Triplet-triplet annihilation then occurs to create high energy singlet states that emit the upconverted light. I show the introduction of functionalized acene molecules on NC surfaces greatly enhances the upconversion



quantum yields (QYs) by up to three orders of magnitude in different systems. As one of the efficiency limiting steps in upconversion, TET is systematically studied by modifying both NC donor and molecular acceptor. TET is characterized by steady state upconversion, time-resolved transient absorption and photoluminescence spectroscopies. TET is dependent on the anchoring groups of the transmitter molecules due to different binding affinities, docking geometries, sterics, intra-molecular spin-orbit couplings and molecule-NC triplet-triplet couplings. Transmitters with phosphonic acid, carboxylic acid and imidazole as binding groups show the best upconversion performance. For the NC donors, small sizes lead to high upconversion QYs due to the large driving force. While the growth of inorganic shells passivates surface traps, TET from core-shell NCs to transmitters is dependent on the shell composition and thickness. TET is improved when submonolayer shells suppress charge transfer and decrease exciton-phonon coupling.

## Table of Contents

Chapter 1	Introduction.....	1
1.1	Introduction to photon upconversion .....	1
1.2	Current status and challenges.....	4
1.3	Molecular design of transmitters.....	8
1.3.1	Molecular energetics: Balancing the trade-off between upconversion QY and energy conservation.....	8
1.3.2	Bulky or rigid transmitters with high fluorescence QYs. ....	10
1.3.3	Decreasing the tunneling barrier during TET .....	11
1.3.4	Increasing the binding affinity of transmitters to NCs.....	14
1.3.5	Stability of the transmitter .....	17
Chapter 2	Hybrid molecule-nanocrystal photon upconversion across the visible and near-infrared. ....	19
2.1	Introduction .....	19
2.2	Results and discussion.....	21
2.3	Conclusion.....	30
Chapter 3	Ligand enhanced NIR photon upconversion.....	31
3.1	Introduction .....	31
3.2	Results and discussion.....	33
3.3	Conclusions .....	40
Chapter 4	CdSe Size and PLQYs in photon upconversion .....	41
4.1	Introduction .....	41

4.2	Results and discussion.....	43
4.3	Conclusion.....	49
Chapter 5 PbS/CdS core/shell QDs suppress charge transfer and enhance triplet energy transfer yield .....		
		50
5.1	Introduction .....	50
5.2	Results and discussion.....	52
5.3	Conclusion.....	61
Chapter 6 ZnS shells enhance triplet energy transfer from CdSe nanocrystals for photon upconversion.....		
		63
6.1	Introduction .....	63
6.2	Results and discussion.....	64
6.3	Conclusion.....	75
Chapter 7 The Goldilocks effect for triplet transfer from CdSe nanocrystals for photon upconversion: anchoring groups.....		
		77
7.1	Introduction .....	77
7.2	Results .....	78
7.3	Discussion .....	85
7.4	Conclusion.....	89
Chapter 8 Supporting Information.....		
		90
8.1	Chemicals.....	90
8.2	Instrument.....	90
8.3	Nanocrystal synthesis.....	93

8.3.1	Synthesis of CdSe nanocrystals .....	93
8.3.2	Synthesis of PbS nanocrystals <sup>3</sup> .....	94
8.3.3	Synthesis of PbSe nanocrystals.....	95
8.3.4	Synthesis of CdSe/CdS and CdSe/ZnS core-shell NCs .....	96
8.3.5	Synthesis of PbS and PbS/CdS QD. ....	97
8.4	Synthesis of transmitter ligands .....	98
8.4.1	Synthesis of 5-CPT .....	98
8.4.2	Synthesis of CdSe NCs and anthracene ligands with different functional groups. ....	99
8.5	Preparation of samples for upconversion, TA and TRPL measurements .....	101
8.6	Quantum yield calculation .....	103
8.6.1	Absolute Quantum Yield Calculation for CdSe.....	103
8.6.2	Quantum Yield Calculation for PbSe (800 nm).....	104
8.6.3	Quantum Yield Estimation for PbSe (980 nm).....	106
8.7	Time-resolved photoluminescence measurement .....	107
8.7.1	Characterization of delayed fluorescence from PbSe/RUB.....	107
8.7.2	Characterization of quenching of CdSe photoluminescence by 9-ACA ligand. ....	107
8.7.3	TRPL measurement of CdSe/CdS and CdSe/ZnS core-shell NCs with 9-ACA .....	109
8.8	Transient absorption measurements and analysis for CdSe/An-X.....	111
8.8.1	Power dependence .....	111

8.8.2	Transient absorption spectra .....	112
8.8.3	Analysis of the kinetics of triplet energy transfer (TET), extracting the rate constant, $k_{TET}$ , and TET efficiency, $\Phi_{TET}$ for the anthracene transmitters. ....	113
8.8.4	Normalizing the initial amplitude of the CdSe NC's exciton bleach at 463 nm by the absorption of the excitation wavelength .....	118
8.9	Transient absorption for CdSe/ZnS//9-ACA and CdSe/CdS//9-ACA .....	118
8.9.1	Power dependence .....	118
8.9.2	Analysis of the kinetics of triplet energy transfer (TET), extracting the rate constant, $k_{TET}$ , and TET efficiency, $\Phi_{TET}$ . ....	119
8.10	Transient absorption of PbS/5-CT and PbS/CdS/5-CT .....	124
8.10.1	Transient absorption spectra of 5-carboxylic acid tetracene (5-CT) .....	124
8.10.2	Spectrum fit for relative population .....	125
8.10.3	Fitting model for transient kinetics. ....	126
8.10.4	Fitting parameters .....	127
8.11	Phosphorescence spectra of anthracene ligands with different functional groups. ....	129
8.12	Cyclic voltammetry (CV) measurements of the highest occupied molecular orbital (HOMO) and lowest unoccupied molecular orbital (LUMO) of NCs and ligands .....	129
8.13	Electronic Structure Calculations .....	132
8.13.1	Time-Dependent Density Functional Theory (TDDFT) Calculations .....	132

8.13.2	Constrained Density Functional Theory with Configuration Interaction (CDFT-CI) Calculations .....	133
8.14	Methods and techniques .....	134
8.14.1	How to average transient absorption spectra .....	134
8.14.2	How to combine the decay in picosecond and microsecond time scales in transient absorption spectra.....	136
8.14.3	How to extract the individual decay from a mixture of two decays .....	137
8.14.4	Extract transient absorption difference spectra.....	139
8.14.5	Synthesis and purification of 5-tetracene carboxylic acid (5-CT) .....	141

## List of Figures

Figure 1.1. (a) Schematic illustration of the energy transfer for CdSe/9-ACA/DPA based photon upconversion of green to violet light. The green arrow indicates the photoexcitation of sensitizer CdSe nanocrystals (NCs, green ball). Energy is transferred to the transmitter, i.e. the bound 9-ACA ligands (red ball), and then to the annihilator DPA (yellow ball), followed by the annihilation between two triplet DPA molecules and subsequent emission from the singlet state of DPA (blue arrow). The same process for the upconversion of near-infrared (NIR) light is shown in (d), with PbX (X=S or Se), CPT and rubrene as the sensitizer, transmitter and annihilator respectively. (b) Photograph of visible upconversion in a cuvette containing CdSe/9-ACA/DPA, with the excitation by a cw 532 nm green laser and 430 nm violet emission. (c) Photograph of NIR upconversion in a cuvette containing PbSe/rubrene. The sample is excited with a cw 800 nm laser, and the yellow emission at 560 nm can be seen. .... 3

Figure 1.2. The upconversion QY,  $\Phi_{UC}$ , is a convolution of four factors, the efficiencies of: (1) intersystem crossing (ISC) within the NC,  $\Phi_{ISC}$ , (2) triplet energy transfer (TET) from NCs to transmitters,  $\Phi_{TET}$ , (3) triplet-triplet annihilation (TTA) between two annihilators,  $\Phi_{TTA}$ , and (4) the fluorescence quantum yield of the annihilators,  $\Phi_A$ . Strategies to enhance  $\Phi_{TET}$  from NC donors to molecular acceptors by synthetic control of the binding group, X, the bridge between the donor and acceptor, and the functionalized conjugated core of the transmitter are discussed in this Perspective..... 8

Figure 1.3. (a) Schematic of the energy transfer in the hybrid CdSe-anthracene photon upconversion platform. The energy diagram depicts the triplet excitonic states of the CdSe

NC donor, the p-phenylene bridges when  $n=1$  and 2, and the anthracene acceptor, which also serves as the transmitter ligand. (b) Absorption (solid line) and fluorescence spectra (dotted line) for different transmitters and CdSe NCs. (c) The rate of triplet energy transfer ( $k_{et}$ , red squares) and the maximum upconversion QY (blue triangles) are shown versus the length of the phenylene bridge in the covalently bound anthracene transmitter ligands on CdSe nanocrystals. Reproduced from reference 33 with permission from the American Chemical Society. .... 10

Figure 1.4. Dexter energy transfer across the bridge between the donor (D) and acceptor (A) can occur via two different pathways. (a) For long bridges or bridges with energy levels that may be resonant with the donor or acceptor, the triplet exciton moves across the bridge as an unseparated hole and electron.<sup>52</sup> (b) The Closs model where the triplet energy transfer consists of individual charge transfer events, typically through short bridges with high tunneling barriers.<sup>53</sup> ..... 13

Figure 2.1. Schematic illustration of NC-organic upconversion strategies. In Strategy A, the organic ligands of the PbSe NC are electronically inert and energy must be transferred directly to the triplet state of the organic emitter RUB. In Strategy B, the energy is first transferred to the triplet state of an anthracene-based ligand, 9-ACA, which then transfers it to the DPA emitter. .... 21

Figure 2.2. a) Absorption and emission spectra of 2.7 nm CdSe/DPA sensitizer/emitter pair in hexane at room temperature. Inset is the full absorption spectrum of CdSe b) Absorption and emission spectra of 2.1 nm PbSe/RUB sensitizer/emitter pair taken in



toluene at room temperature. Inset is the absorption of PbSe's first exciton. Arrows indicate excitation wavelengths for photon upconversion. .... 22

Figure 2.3. a) Photograph of upconversion in a cuvette containing the 2.1 nm PbSe/RUB mixture. The yellow spot is emission from the RUB originating from an unfocused cw 800 nm laser with an intensity of 1 W/cm<sup>2</sup>. b) Log-log plot of upconversion signal versus laser intensity (W/cm<sup>2</sup>) for the PbSe/RUB mixture, showing the transition from quadratic (slope = 2) to linear (slope = 1) regimes. (a) and (b) were conducted in dry and degassed toluene with 3.84 mM rubrene and 58.1 μM PbSe NCs at room temperature. .... 23

Figure 2.4. a) Prompt fluorescence decay of PbSe/RUB (red line) and RUB (black line) samples in a 100 ns time window. Inset: logarithmic plot of decay along with exponential fits (crosses). The singlet decay time decreases from 16.2 ns for RUB alone to 14.3 ns in the PbSe mixture. b) Logarithmic plot of the delayed fluorescence decay of PbSe/RUB (red) and RUB (black) samples on the μs timescale. The spike at time=0 is due to prompt fluorescence due to direct two-photon excitation of the RUB. Inset: logarithmic plot of delayed fluorescence component overlaid with fit with 41 μs decay time and a 5% offset. .... 25

Figure 2.5. a) Photographs of upconversion in a cuvette containing an optimized CdSe/9-ACA sample (top) and a CdSe/ODPA sample (bottom). The spectra of these samples are shown in the Chapter 8. The violet DPA output in the 9-ACA sample (top) swamps the green CdSe emission and laser scatter that is clearly seen in the ODPA sample (bottom). (b) Log-log plot of upconversion versus laser intensity for the 3.3 nm CdSe/9-ACA/DPA sensitizer/ligand/emitter system, showing the transition from quadratic (slope = 2) to linear

(slope = 1) regimes. All experiments were conducted in dry and degassed hexanes respectively with 1 mM DPA and 5 $\mu$ M CdSe NCs at room temperature.....	28
Figure 2.6. a) The relative upconversion efficiency with different transmitter anthracene ligands and the ODPa ligand attached to the CdSe NCs in toluene. b) Decay of CdSe/ODPA sample (black) and extracted CdSe component from CdSe/9-ACA sample (red). Details of the data analysis can be found in the Chapter 8. Inset: Logarithmic comparison of the decays.....	29
Figure 3.1. (a) Schematic of energy transfer during upconversion in this hybrid system with PbX (X=S, Se) as sensitizer, CPT as transmitter and rubrene as annihilator. (b) Absorption and emission spectra of CPT (purple), rubrene (dark cyan), 2.9 nm PbS (red) and 2.5 nm PbSe (black) in toluene at room temperature, with excitation wavelength (808 nm) indicated by the black arrow.....	33
Figure 3.2. The relative upconversion QY is plotted with the upconversion fluorescence intensity normalized by the absorption at the excitation wavelength of 808 nm (black squares), and the number of bound CPT transmitter ligands per NC (hollow blue triangles) for (a) PbS, and (b) PbSe NC versus [CPT] in the ligand exchange solution. Both of the samples contain 1 mM rubrene and were measured in 200 $\mu$ m thick capillary tubes sealed in air-free cuvettes. Ligand exchange condition: PbS: stirring 10 $\mu$ M PbS with CPT in designated concentration for 40 min; PbSe: stirring 29 $\mu$ M PbSe with CPT in designated concentration for 20 min.....	36
Figure 4.1. (a) In this hybrid system, the CdSe nanocrystals sensitizers are functionalized with a 9-ACA transmitter ligand. DPA serves as the annihilator. The green arrow indicates	

photo-excitation of CdSe NCs of different sizes, followed by energy transfer from CdSe to 9-ACA, then triplet-triplet energy transfer to DPA. Two DPA triplets annihilate to one singlet state and emit an upconverted photon (blue arrow). (b) Absorption (solid line) and emission (dashed line) spectra of DPA and CdSe NCs with 7 sizes measured in hexane at RT. Blue and green arrows indicate excitation wavelengths. .... 42

Figure 4.2. Log-log plot of the upconversion signal versus absorption at excitation wavelengths, showing the transition from quadratic (slope=2) to linear (slope=1) regimes. Measurements were conducted with 2.7 nm CdSe in dry and degassed hexanes at room temperature, with excitation wavelengths of 19.8 W/cm<sup>2</sup> 488 nm (black solid square) and 12.7 W/cm<sup>2</sup> 532 nm (red hollow square). The concentration of DPA is 2.15 mM. .... 44

Figure 4.3. All measurements were conducted at RT with 1 mM DPA and a 532 nm laser at 12.7 W/cm<sup>2</sup>. (a) Upconverted DPA emission in toluene decreases as the concentration of 9-ACA transmitter in the ligand exchange solution with 3.2 nm CdSe NCs decreases. (b) Upconversion photoluminescence spectra of 1.5 μM 2.7 nm CdSe/9-ACA in different solvents. (c) The upconversion signal versus the solubility limit of 9-ACA in the solvents in (b). .... 47

Figure 4.4. (a) Upconverted DPA photoluminescence spectra using CdSe NC sensitizers excited with a 12.7 W/cm<sup>2</sup> 532 nm cw laser. (b) Plot of upconversion QY versus CdSe NC PLQY, with the diameter (nm) of each NC labelled. (c) Plot of the UCQY normalized by PLQY versus size of CdSe NCs. All measurements were done with 488 nm (black cross) and 532 nm (red hollow square) excitation at RT with 2 μM CdSe and 1.7 mM DPA in dry, degassed hexane. .... 47

Figure 5.1. (a) Schematic of the energy transfer processes during photon upconversion using a hybrid PbS quantum dot (QD)-tetracene-rubrene platform. (b) Redox potential of PbS/CdS QD and 5-CT (vs vacuum) measured by cyclic voltammetry in dichloromethane at -50°C for the QD and RT for free 5-CT. (c) Energy level of various energy and charge transfer states involved in the decay of QD excitons. Also shown is the initial excitation (orange arrow), hole transfer (HT), hot hole transfer (HHT) and triplet energy transfer (TET)..... 51

Figure 5.2. Comparison of TA spectra of QD//OA and QD//5-CT. TA spectra of (a) PbS QD capped with oleic acid, PbS//OA; (b) PbS QD capped with 5-carboxylic acid tetracene (5-CT), PbS//5-CT; (c) PbS/CdS core-shell QD capped with oleic acid, PbS/CdS//OA, and (d) PbS/CdS core-shell QD capped with 5-CT, PbS/CdS//5-CT. Samples are dissolved in toluene and excited at 800nm. Each curve in the figure is the average of the spectra within the indicated delay time window. Spectra from 785 to 815 nm are truncated due to the saturation of probe on the spectrometer..... 55

Figure 5.3. TA spectra and kinetics of triplet energy transfer. (a) TA spectra of 5-CT in tetrahydrofuran at the indicated delay times; Double difference TA spectra of (b) bound 5-CT on PbS/CdS QD at 1-2ps (blue) and 10-100 ns (black), (c) bound 5-CT on PbS QD at 1-2 ps (blue) and 3-4  $\mu$ s (black); (d) The inverted steady state electronic absorption spectrum of bound 5-CT. The QD//5-CT samples were excited at 800 nm while the free 5-CT at 400 nm. The double difference TA spectra of bound 5-CT are obtained by subtracting the contribution of the QD from the TA spectra shown in Fig. 5.2b and d (see Chapter 8 for details). ..... 56

Figure 5.4. Kinetics of QD exciton bleach (XB, blue circles) at 820 nm and 5-CT triplet (red circles) at 489 nm for (a) PbS//5-CT and (b) PbS/CdS//5-CT. Also shown for comparison are the XB kinetics of QDs without 5-CT (green circles). Solid lines are a global fit to the kinetics according to the model in the main text..... 59

Figure 6.1. (a) Illustration of the triplet energy transfer (TET) in this hybrid photon upconversion system. Green and blue arrows denote photoexcitation of the nanocrystals (NCs) and emission from diphenylanthracene (DPA) respectively. Dotted black and red curved arrows denote the triplet-triplet annihilation and TET. The absorption (solid line) and emission (dashed line) spectra of (b) 9-ACA (top), DPA (middle), 2.9 nm diameter CdSe NCs (bottom); (c) CdSe/ZnS and (d) CdSe/CdS core-shell NCs with different shell thickness (ML =monolayer). The black arrow in the bottom panel of Fig. 6.1b indicates the excitation wavelength used (488 nm). Measurements are performed in hexane at room temperature. .... 65

Figure 6.2. The (a) Intensity weighted average lifetimes; (b) Radiative ( $k_r$ ) and nonradiative ( $k_{nr}$ ) rate constants normalized relative to the CdSe core; (c) Photon upconversion QYs of the NC sensitizers with surface bound 9-ACA and 2.15 mM DPA with respect to shell thickness. CdSe/ZnS and CdSe/CdS core/shell nanocrystals (NCs) are denoted by the red square and black triangle respectively. Data in (a) and (b) are obtained from lifetime measurements (see Chapter 8) with a 406 nm pulsed laser and (c) with a 488 nm CW laser at 19.8 W/cm<sup>2</sup>. All samples are dissolved in hexane and measured at room temperature.68

Figure 6.3. Femtosecond transient absorption (TA) spectra of (a) CdSe; (b) CdSe/(0.5ML)CdS; and (c) CdSe/(0.5ML)ZnS nanocrystals (NCs); (d)-(f) TA spectra of

the same NCs with surface bound 9-anthracenecarboxylic acid. Samples are dissolved in hexane and excited with a 540 nm pulsed laser. The black dashed curves in (a) and (c) are the linear absorption spectra of CdSe core and 0.5 ML CdSe/ZnS core-shell NCs, and the magenta and black dashed curves in (b) are that of CdSe core and 0.5 ML CdSe/CdS core-shell NCs respectively..... 70

Figure 6.4. (a) The initial ground state bleach at 523 nm for CdSe, CdSe/(0.5ML)ZnS, and CdSe/(0.5ML)CdS with and without surface bound 9-ACA. The curves for NCs only are normalized with the initial minimum O.D. to be -1, and curves for NCs capped with 9-ACA are normalized based on the NC concentration, i.e. the O.D. at 540 nm in the linear absorption spectra. Green curves are the global fits to the recovery of the GSB at 433 nm (averaged over 430-435 nm) and 523 nm (averaged over 520-525 nm) for CdSe//9-ACA and 0.5 ML CdSe/ZnS//9-ACA. Measurements were performed in hexane at room temperature, with the excitation of 540 nm pulsed laser. (b) The energy diagram describing the physical processes during TA measurements. .... 73

Figure 7.1. (a) Schematic of the energy transfer in this hybrid photon upconversion platform. Upon excitation with a 488 nm cw laser, triplet energy transfer (TET) occurs from CdSe nanocrystals (NCs) to the bound anthracene transmitter, and subsequently to 9,10-diphenylanthracene (DPA, yellow box). Two DPA triplets fuse to form a singlet, followed by emission at 430 nm. (b) Illustration of TET from CdSe NCs to bound anthracene ligands through anchoring groups, X. The absorption (solid line) and emission (dashed line) spectra of (c) 2.4 nm diameter CdSe NCs, (d) DPA, and (e)-(m) transmitter ligands with different anchoring groups measured in hexane at room temperature. .... 78

Figure 7.2. (a) The HOMO and LUMO energy levels (red solid line) and  $T_1$  state (relative to HOMO, red dashed line) versus vacuum for CdSe NCs (left), anthracene ligands with functional group X (An-X) and DPA (right) and the photon upconversion QYs (black square) from Table 7.1. See text for details. (b) Femtosecond transient absorption spectra of CdSe NCs capped with native ligand octadecylphosphonic acid (ODPA), and (d) An- $PO_3H_2$ . (c) The initial ground state bleach at 463 nm corresponding to CdSe/ ODPA (red), CdSe/ An- $PO_3H_2$  (blue) and CdSe/ An-CSSH (black) in hexane at RT. Samples are dissolved in hexane and excited with a 505 nm pulsed laser..... 83

Figure 7.3. (a) Histogram of the photon upconversion QY for anthracene ligands (yellow bars), plotted with the relative decrease of initial exciton bleach of the CdSe NC donor ( $\Delta_{XB}$ , red triangles, left), and the TET efficiency  $\Phi_{TET}$  (blue squares, right) listed in Table 7.1 and 7.2. (b) The energetics of the reaction path on the  $T_1$  surface of An-Py going from the  $T_1$  minimum-energy geometry to the  $T_1/S_0$  minimum-energy crossing point geometry, as computed using nodes and the freezing string method.<sup>200</sup> The first node is at the global minimum and the final node is at the intersection between the  $T_1$  and  $S_0$  potential energy surfaces. The lower-left structure displays the geometry of An-Py near the global minimum (node 1 on the reaction path above); the lower-right structure is of the local minimum near the minimum-energy crossing point (node 16 on the reaction path above) with the  $S_0$  surface, only 0.20 eV above the global minimum. This local minimum seems to be caused by steric clashing between the ortho hydrogens on the aryl groups and the hydrogens in the 1 and 8 positions on the anthracene. This local minimum on the  $T_1$  surface can confine the

anthracene near a $T_1/S_0$ conical intersection, accelerating intersystem crossing between the two states and lowering the triplet lifetime.....	85
Figure 7.4. Structures of An-Py and An-Py <sub>2</sub> transmitters and their upconversion QYs, $\Phi_{UC}$ , in the presence of CdSe light absorbers and DPA emitters. ....	88
Figure 8.1. Setup of NIR upconversion measurements. Photos of a cuvette containing the sample in a 100 $\mu\text{m}$ thick capillary tube (left) and the upconversion measurement setup (right). Each part is described under the Instrumentation section. ....	93
Figure 8.2. TEM of the 3.28 nm diameter CdSe NCs. ....	94
Figure 8.3. TEM image of the 3.10 nm diameter PbS nanoparticles.....	95
Figure 8.4. TEM image of 2.10 nm diameter PbSe nanoparticles.....	96
Figure 8.5. The TEM images of (a) 2.9 nm diameter CdSe core, (b-d) CdSe/ZnS and (e-k) CdSe/CdS core-shell NCs of different shell thickness. ....	97
Figure 8.6. (a) Intrinsic (red) and detected (black) upconversion fluorescence spectra of DPA. The intrinsic fluorescence spectrum is scaled to match the upconversion spectrum at 450 nm. (b) Intrinsic (red) and detected (black) Rhodamine 6G fluorescence spectra. The intrinsic spectrum of the Rhodamine 6G standard is scaled to match the experimental spectrum at 550 nm.....	104
Figure 8.7. Comparison of early time (0-100 ns, black) and late time (0.6-390 $\mu\text{s}$ , red) fluorescence from the PbSe/RUB sample after excitation with 800 nm laser pulse. The early spectrum reflects prompt fluorescence due to nonresonant two-photon excitation of the RUB, while the delayed fluorescence is due to upconverted signal after TTA by RUB molecules sensitized by PbSe NC's. The slightly different spectral shapes reflect additional	



self absorption of the prompt (two-photon) fluorescence due to the deeper penetration of the two-photon excitation mode into the sample cuvette..... 107

Figure 8.8. Comparison of the fluorescence decays of DPA by itself (black) and the CdSe/9-ACA/DPA sample (red). Inset: Logarithmic comparison of the decay. Both are single exponential with a lifetime of  $6.5 \pm 0.1$  ns for the CdSe/9-ACA/DPA sample and  $6.3 \pm 0.1$  ns for the DPA sample. .... 108

Figure 8.9. (a) The CdSe emission peak (centered at 570 nm) with overlapping 9-ACA fluorescence (centered at 490 nm) is fit with a dual Gaussian fit (red line) in the time window 54-75 ns. The amplitude of the Gaussian centered at 570 nm is taken to be the amplitude of the CdSe luminescence in this time window. (b) Decay of the CdSe/ODPA sample (black) and extracted CdSe component from the CdSe/9-ACA sample (red). Inset: Logarithmic comparison of the decays. Both decays are multiexponential, as typically seen for CdSe NCs, but the CdSe/9-ACA sample diverges from the CdSe/ODPA sample after 10 ns and decays more rapidly..... 108

Figure 8.10. Photoluminescence decay of (a) 2.9 nm diameter CdSe core, (b-d) CdSe/ZnS and (e-k) CdSe/CdS core-shell NCs of different shell thickness. Samples are dissolved in hexane and excited with a 406 nm pulsed laser. The raw data is shown as black hollow circle, with the red curves the triexponential fits..... 109

Figure 8.11. The absorption intensity of CdSe/ODPA NCs at 463 nm versus the excitation power plotted in log scale obtained from the TA difference spectra. The laser power of 220 nJ was used to excite all samples to avoid exciton-exciton annihilation processes observed at higher powers (slope=0.5). Samples were excited at 505 nm..... 111

Figure 8.12. Picosecond TA difference spectra of CdSe NCs capped with (a) native octadecylphosphonic acid, CdSe/ODPA, (b) 9-anthracenephosphonic acid, CdSe/An-PO<sub>3</sub>H<sub>2</sub>, (c) 9-anthraceneimidazole, CdSe/An-Im, (d) 9-anthracenepyridine, CdSe/An-Py, (e) 9-anthracene-p-aniline, CdSe/An-PhNH<sub>2</sub>, (f) 9-anthraceneamine, CdSe/An-NH<sub>2</sub>, (g) 9-anthracenethiol, CdSe/An-SH, (h) 9-anthracenedithiolcarbamate CdSe/An-NHCSSH, and (i) 9-anthracenedithioic acid, CdSe/An-CSSH. Samples were selectively excited with a 505nm pulsed laser. .... 112

Figure 8.13. The recovery of the ground state bleach (GSB) at 463 nm (red) and the normalized decay of the excited state absorption (ESA) at 437 nm (blue) shows the same kinetics for unfunctionalized CdSe/ODPA. These trajectories are extracted from Fig. 8.12a and can be fit with two exponentials..... 113

Figure 8.14. Global fitting (black) of the decay of the ESA at 437 nm (green) and recovery of the GSB at 463 nm (red) for CdSe NCs capped with (a) 9-anthracenephosphonic acid, CdSe/An-PO<sub>3</sub>H<sub>2</sub>, (b) 9-anthraceneimidazole, CdSe/An-Im, (c) 9-anthracenepyridine, CdSe/An-Py, (d) 9-anthracene-p-aniline, CdSe/An-PhNH<sub>2</sub>, (e) 9-anthraceneamine, CdSe/An-NH<sub>2</sub>, (f) 9-anthracenethiol, CdSe/An-SH, (g) 9-anthracenedithiolcarbamate CdSe/An-NHCSSH, and (h) 9-anthracenedithioic acid, CdSe/An-CSSH, based on Eq. 8.8 and Eq. 8.9. The measurements were performed in hexane at room temperature, with the excitation of 505 nm pulsed laser. .... 115

Figure 8.15. The initial ground state bleach at 463 nm corresponding to CdSe/ODPA, and CdSe NCs capped with different anthracene ligands. Measurements were performed in

hexane at room temperature with the excitation of a 505 nm pulsed laser. All the data has been normalized by the O.D. at 505 nm in the steady state absorption spectra..... 118

Figure 8.16. The absorption intensity of CdSe NCs at 441 nm at 3 ps versus the excitation power plotted in log scale obtained from the TA difference spectra. The laser power of 220 nJ was used to excite all samples to avoid exciton-exciton annihilation processes observed at higher powers (slope=0.5). Samples were dissolved in hexane and excited with a 540 nm pulsed laser at room temperature. .... 118

Figure 8.17. Kinetic traces at 433 nm for 0.5 ML CdSe/CdS with (black hollow square) and without (red hollow circle) surface bound 9-ACA. The subtraction of the decay for CdSe/CdS only (as background signal) from CdSe/CdS//9-ACA yields the 9-ACA triplet (blue hollow triangle)..... 119

Figure 8.18. The recovery of the ground state bleach (GSB) at 433 nm (black hollow circle, averaged over 430-435 nm) and the normalized GSB at 523 nm (red hollow triangle, averaged over 520-525 nm) show the same kinetics for CdSe core (a) and CdSe/ZnS core shell NCs (b). The normalization was performed based on the O.D. at 433 nm at 100 ps. .... 120

Figure 8.19. Global fitting (black) of the decay of the ESA at 433 nm (red) and 523 nm (green) for CdSe//9-ACA (a) and 0.5 ML CdSe/ZnS//9-ACA (b) based on Eq. 8.11 and Eq. 8.12. The measurements were performed in hexane at room temperature, with the excitation of 540 nm pulsed laser. .... 122

Figure 8.20. TA spectra and kinetics of 5-carboxylic acid tetracene (5-CT) in solution. (a) Nanosecond transient absorption spectra of 5-CT in tetrahydrofuran at room temperature

measured with 400 nm excitation. (b) Transient kinetics of 5-CT probed at 465 nm (open symbols) and biexponential fit (solid line), yielding a singlet lifetime of 10.19 ns and triplet lifetime of 108.4  $\mu$ s (c) and (d) provide an expanded view of triplet excited state absorption of 5-CT..... 124

Figure 8.21. Nanosecond TA spectra of 5-CT in a) PbS/OA and b) PbS//5-CT. (c) Double difference spectra of PbS/5-CT obtained by subtracting the PbS/OA TA signal from the TA signal of PbS//5-CT. Also shown for comparison is the static absorption spectra of 5-CT on PbS QD (blue line, inverted). Vertical lines indicate the position of the ground state bleach. (d) Relative population of the charge separated state (blue square) and 5-CT triplet excited state (red dot) in PbS//5-CT. These populations were obtained by fitting double difference spectra to a model that accounts for both charge separated state and triplet state (see below for details). The black solid line represents a single exponential fit of the decay of the charge separated state. The dashed blue line represented the kinetics of 5-CT ground state bleach extracted directly from the double difference spectra of PbS//5-CT. The red dashed line is the 489 nm kinetics obtained from double difference TA spectrum in (c). ..... 125

Figure 8.22. Comparison of microsecond time range TA spectra of (a) PbS/CdS//OA and (b) PbS/CdS //5-CT. (c) Double difference TA spectrum of PbS/CdS //5-CT..... 126

Figure 8.23. Phosphorescence spectra of anthracene ligands measured in a glass of 2-methyltetrahydrofuran at 77K..... 129

Figure 8.24. Cyclic voltammogram (CV) of anthracene transmitter ligands with different functional groups in an anhydrous dichloromethane (DCM) solution containing tetra-n-

butylammonium hexafluorophosphate (0.1 M) as electrolyte. CV measurements were performed at room temperature at a scan speed of  $100 \text{ mV s}^{-1}$ . The phosphorescence from An-Py, An-NH<sub>2</sub> and An-SH could not be obtained. The energy of T<sub>1</sub> state for these three ligands are calculated as the average of the values for other ligands. .... 131

Figure 8.25. Cyclic voltammogram (CV) of (a) PbS/CdS core-shell QD measured at  $-50^\circ\text{C}$  and (b) 5-carboxylic acid tetracene measured RT. Both CVs were performed in dichloromethane at a scan speed of  $100 \text{ mV s}^{-1}$ . .... 132

## List of Tables

Table 4.1. The diameter, optical properties, and upconversion QYs of the CdSe NC sensitizers.....	46
Table 5.1. Key parameters for the hybrid photon upconversion system: absorption maxima, $\lambda_{\text{abs}}$ ; emission maxima, $\lambda_{\text{ems}}$ ; average number of bound 5-carboxylic acid tetracene (5-CT) per QD, N; photon upconversion quantum yield (UCQY); efficiency of triplet energy transfer (TET) from QD to 5-CT, $\Phi_{\text{TET}}$ ; and the rate of TET, $k_{\text{TET}}$ .....	53
Table 6.1. The shell thickness n in monolayer (ML), absorption and emission maxima, $\lambda_{\text{abs}}$ and $\lambda_{\text{ems}}$ ; average number of bound ligands per NC, N; mole ratio of Se: Cd: Zn from ICP-AES; the radiative rate constant, $k_{\text{r}}$ ; the nonradiative rate constant, $k_{\text{nr}}$ ; the photoluminescence quantum yield, $\Phi_{\text{PL}}$ ; and the photon upconversion quantum yield, $\Phi_{\text{UC}}$ for each nanocrystal. ....	67
Table 6.2. The rate constant of triplet energy transfer (TET), $k_{\text{TET}}$ ; TET efficiency $\Phi_{\text{TET}}$ ; and the relative decrease of initial exciton bleach of CdSe NCs monitored at 520 nm due to An-X, $\Delta_{\text{XB}}$ . ....	71
Table 7.1. The absorption and emission maxima, $\lambda_{\text{abs}}$ and $\lambda_{\text{ems}}$ ; the energy corresponding to the $T_1$ , $E_{T1}$ ; the HOMO and LUMO energy levels, $E_{\text{HOMO}}$ and $E_{\text{LUMO}}$ ; the optical gap, $E_{\text{gap}}$ ; the fluorescence QY, $\Phi_{\text{F}}$ ; average number of bound ligands per NC, N; and the photon upconversion QY, $\Phi_{\text{UC}}$ for each anthracene transmitter ligand with functional group X. 81	
Table 7.2. The rate of triplet energy transfer (TET), $k_{\text{TET}}$ ; the normalized $k_{\text{TET}}$ , $k_{\text{TET}}/N$ ; TET efficiency $\Phi_{\text{TET}}$ ; and the relative decrease of initial exciton bleach of CdSe NCs monitored at 463 nm due to An-X, $\Delta_{\text{XB}}$ . ....	84

Table 7.3. Constrained Density Functional Theory with Configuration Interaction (CDFT-  
 CI) calculations for electronic couplings between a triplet on the NC and a triplet on the  
 ligand..... 87

Table 8.1. Parameters from the triexponential fits of the photoluminescence decay for CdSe  
 core and CdSe/ZnS, CdSe/CdS core-shell nanocrystals.  $n$  is the shell thickness in  
 monolayers (ML);  $A_1, A_2, A_3$  and  $\tau_1, \tau_2, \tau_3$  are the amplitudes and time constants,  $A_0$  is the  
 y-offset of the decay..... 110

Table 8.2: Parameters from the global fits of the decay of the ESA at 437 nm (green) and  
 rise of the GSB at 463 nm (red) for CdSe NCs capped with different anthracene ligands in  
 Figure 8.14, based on Eq. 8.8 and Eq. 8.9.  $t_0$  is the correction for time zero.  $A_0, A_1, \tau_0, \tau_1$   
 are the amplitudes and time constants of the intrinsic decays of CdSe NCs at 463 nm (from  
 the GSB),  $A_2, \tau_2$  are the amplitude and time constant for the decay due to TET at 463 nm  
 (from the GSB).  $A$  is the amplitude of the rise of  $T_1-T_n$  transition of anthracene ligands at  
 437 nm (ESA).  $m$  is the proportionality constant between ESA and GSB.  $k_{TET}$  is the TET  
 rate constant.  $\Phi_{TET}$  is the TET efficiency. All the amplitudes are normalized by the  
 concentration of CdSe NCs for different samples. .... 116

Table 8.3: Parameters from the global fits of the kinetics at 433 nm (green) and 523 nm  
 (red) for CdSe//9-ACA and 0.5 ML CdSe/ZnS//9-ACA.  $t_0$  is the correction for time zero.  
 $A_0, A_1, \tau_0, \tau_1$  are the amplitudes and time constants of the intrinsic decays of NCs at 523  
 nm (from the GSB),  $A_2, \tau_2$  are the amplitude and time constant for the decay due to TET at  
 523 nm (from the GSB).  $A$  is the amplitude of the rise of  $T_1-T_n$  transition of 9-ACA at 433  
 nm.  $m$  is the proportionality constant between GSB of NCs at 433 nm and 523 nm.  $k_{TET}$  is

the TET rate constant.  $\Phi_{\text{TET}}$  is the TET efficiency. All the amplitudes are normalized by the concentration of CdSe NCs for different samples. .... 123

Table 8.4. Parameters obtained from fitting kinetics traces displayed in Fig. 5.4..... 127

Table 8.5. Component corresponded TET efficiency..... 128

Table 8.6. TDDFT calculations of  $S_0/S_1$  and  $S_0/T_1$  energy gaps, activation energies for  $T_1$ - $S_0$  transitions, and spin-orbit couplings (SOC) of  $S_0$  and  $S_1$  to triplet states for different anthracene ligands..... 133



## **Chapter 1 Introduction**

### **1.1 Introduction to photon upconversion**

In hybrid material systems, the goal is to retain the desirable properties associated with the original components while creating synergies between various elements for added value. For the purpose of this Perspective, a hybrid material is comprised of semiconductor nanocrystals and organic semiconductors, i.e. conjugated small molecules or polymers. The key idea is to retain the mechanical strength and electronic properties of the inorganic portion, the processability and ease of functionalization of the organic constituents, while directing energy at nanoscale dimensions by control of multi-excitonic processes. Hybrid materials can overcome the traditional limits associated with the individual building blocks, as seen in applications in optics,<sup>1</sup> electronics,<sup>2</sup> biosensors<sup>3</sup>, and photovoltaics.<sup>4</sup> For example, dye sensitized solar cells (DSSCs)<sup>5</sup> combine a stable titania photoanode that has excellent transport properties with synthetically tunable organometallic complexes. This combination addresses the relatively low electron mobility in molecular systems and the transparency of titania to visible light. Compared to titania, the high extinction coefficients in the visible and near-infrared (NIR) of the organometallic dyes allow much more of the solar spectrum to be collected for a power conversion efficiency of up to 15%.<sup>6</sup>

In this chapter, we discuss a hybrid platform consisting of semiconductor nanocrystals (NCs) and organic molecules for photon upconversion that can potentially improve the efficiencies of photovoltaics and photocatalysts under one sun conditions. Photon upconversion occurs when low energy photons are converted to high energy photons. Like the DSSCs, this hybrid platform makes use of the unique properties of each

component. It exploits 1) the large absorption coefficients of the NCs,<sup>7</sup> 2) their ability to extend into the NIR<sup>8-10</sup> and 3) triplet-triplet annihilation (TTA) in organics for photon upconversion.<sup>11</sup> These characteristics are unavailable simultaneously in existing lanthanide<sup>12</sup> and molecule<sup>11</sup> based photon upconversion systems. Lanthanide doped matrices, or rare-earth glasses have been studied for decades, but are generally excited with pulsed or high power lasers because of their low photon upconversion efficiency. The best reported quantum yields (QYs) are 3-12% in the bulk<sup>13,14</sup> and 5% and 7.6%<sup>15</sup> at the nanoscale. Typical QYs are between 10<sup>-2</sup> to 10<sup>-4</sup> % for nanosized lanthanide doped NCs.<sup>16</sup> This low efficiency stems from the extremely small absorption cross-section ( $\sim 10^{-20}$  cm<sup>2</sup>)<sup>17</sup> of the single absorbing ions (typically Yb<sup>3+</sup>) dispersed in the glassy matrix and the parity forbidden nature of these 4*f*-4*f* transitions.<sup>18</sup> Despite efforts in the field of organic photovoltaics to design conjugated polymers that harvest infrared photons,<sup>19</sup> it remains difficult to find organic structures that absorb strongly at wavelengths to the red of 900 nm. In addition to lower photostability, organic chromophores that absorb strongly in the NIR undergo rapid internal conversion to the ground state.<sup>20</sup>

The hybrid TTA-based upconversion system discussed here is able to utilize both visible and NIR photons. As shown in Fig. 1.1a and 1.1d, it is composed of inorganic semiconductor nanocrystals (NCs) as sensitizers (CdSe NCs in Fig. 1.1a, and PbS/PbSe NCs in Fig. 1.1d), bound organic ligands on NCs as transmitters (9-anthracene carboxylic acid, or **9-ACA** in Fig. 1a, 4-(tetracen-5-yl)benzoic acid or **CPT** in Fig. 1.1d), and organic annihilators (9, 10-diphenylanthracene, or **DPA** in Fig. 1.1a, and rubrene in Fig. 1.1d) in solution. As the light absorbers, these photostable semiconductor NCs have size and shape

dependent optical properties that are easily controlled via colloidal synthesis. Here, the NCs absorb the low energy photons that are then transferred as triplets to the transmitter ligand covalently bound to the NC surface. Triplet energy transfer (TET) then occurs again down an energy cascade, this time from the transmitter to the annihilator. Two annihilator molecules in their triplet-excited state collide in a spin-allowed, energy conserved manner known as TTA to emit a higher energy photon. Fig. 1.1b and 1.1c show the upconverted photons that are emitted when excited by visible and NIR light respectively.

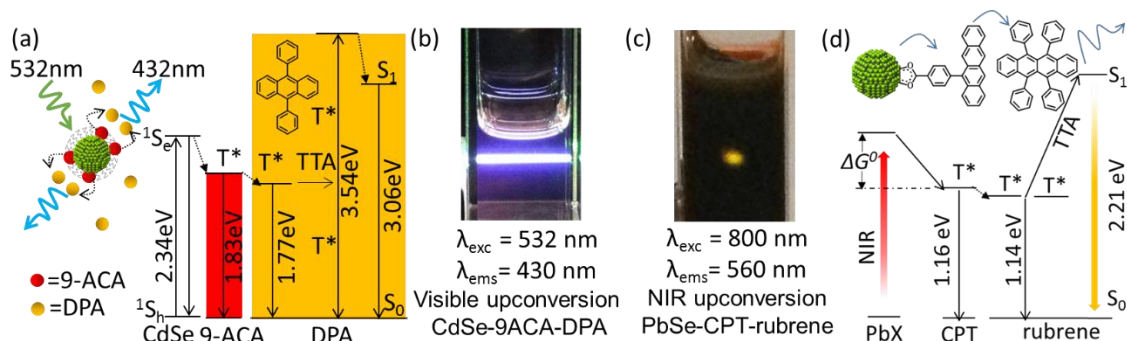


**Figure 1.1.** (a) Schematic illustration of the energy transfer for CdSe/9-ACA/DPA based photon upconversion of green to violet light. The green arrow indicates the photoexcitation of sensitizer CdSe nanocrystals (NCs, green ball). Energy is transferred to the transmitter, i.e. the bound 9-ACA ligands (red ball), and then to the annihilator DPA (yellow ball), followed by the annihilation between two triplet DPA molecules and subsequent emission from the singlet state of DPA (blue arrow). The same process for the upconversion of near-infrared (NIR) light is shown in (d), with PbX (X=S or Se), CPT and rubrene as the sensitizer, transmitter and annihilator respectively. (b) Photograph of visible upconversion in a cuvette containing CdSe/9-ACA/DPA, with the excitation by a cw 532 nm green laser and 430 nm violet emission. (c) Photograph of NIR upconversion in a cuvette containing PbSe/rubrene. The sample is excited with a cw 800 nm laser, and the yellow emission at 560 nm can be seen.

In this chapter, we summarize the current results in the sub-field of triplet energy transfer specifically across this hybrid nanocrystal-molecule interface. We then examine the factors limiting the upconversion QYs, followed by the strategies to improve the QY by improving TET. In particular, we focus on the molecular design of the transmitter

ligands, including molecular energetics, photophysics, energy offsets compared to the NC donor, binding groups to the NC donors, finally concluding with suggestions for alternatives to the acene family.

## 1.2 Current status and challenges

The first observation of triplet energy transfer between nanocrystals and molecules were two joint publications in 2014. It was demonstrated that conjugated molecules in the form of linear fused acenes donated triplet excitons to lead chalcogenide NCs. These triplet excitons were created when a singlet excited state in the acene, created by the absorption of light, splits or fissions into two bound electron-hole pairs with unpaired spins. Singlet fission can be thought of the downconversion of photons because the original high energy singlet state is split into two triplet excitons.<sup>21,22</sup> Baldo and Bawendi reported enhanced photoluminescence (PL) of PbS NCs due to the downconversion of singlets formed in tetracene, and subsequent TET to the PbS acceptors.<sup>23</sup> Using transient absorption spectroscopy, Rao et al showed that triplets derived from singlet fission migrated from pentacene to PbSe NCs, followed by backwards hole then electron transfer from the NCs to the acene.<sup>24</sup> These studies hinted at the possibility of the reverse processes, which is triplet energy transfer from NCs to molecules. After our first report of triplet excitons transferred from inorganic semiconductor NCs to organic molecules<sup>25</sup>, Wu *et al.*<sup>26</sup> reported the same physical phenomenon. We employed CdSe and PbS/PbSe NCs as sensitizers of conjugated molecules, or triplet donors to acenes for photon upconversion<sup>25</sup>. Wu et al described the emission of yellow light by rubrene, created when triplets donated from PbS NCs annihilated each other to create a singlet exciton. They showed the photon

upconversion of NIR light absorbed by PbS NCs in thin film. In terms of mechanistic studies, Mongin *et al.*<sup>27</sup> observed the formation of triplet excitons on anthracene ligands bound to CdSe NCs that occurred after the NCs were photoexcited. These transient absorption experiments directly showed triplet energy transfer from inorganic NCs to bound organic ligands.

Analysis of the kinetics of the energy transfer from the CdSe NCs to **9-ACA** suggests that the overall efficiency is limited by the fast non-radiative decay channels in NCs, and the low coverage of **9-ACA** ligands.<sup>28</sup> In line with this, CdSe-ZnS core-shell NCs as sensitizers have been reported to enhance the upconversion QYs to 1.4% by 50 times compared to core-only CdSe NCs,<sup>29</sup> as the trap states for non-radiative recombination on the CdSe core are passivated by the ZnS shell. Similarly, CdS-ZnS and PbS-CdS core-shell NCs were essential in achieving 5.2 % and 8.4% photon upconversion QYs for the production of ultra-violet light and visible light respectively.<sup>30</sup> With NC light absorbers, visible to UV upconversion is 5 times more efficient compared to organic sensitizers<sup>30-32</sup>, while the relatively high 8.4% NIR to visible upconversion QY was realized with an excitation intensity of 3.2 mW/cm<sup>2</sup>, approximately three times lower than the available solar flux.<sup>33</sup> We have also found that CdSe NCs with higher PL QYs result in higher upconversion QYs because of reduced midgap and surface trap states.<sup>34</sup> For example, for CdSe NCs of the same size, NC donors with PL QYs of 8.9% and 3.5% have photon upconversion QYs of 4.4% and 1.4% respectively.<sup>34</sup>

In contrast to triplet energy transfer from pentacene to PbSe NCs, triplet exciton migration in the opposite direction, i.e. from NCs to acenes does not show the same

dependence on the energy offsets between the donors and acceptors. The Cambridge group reports that resonant energy transfer occurs from acene to NC, where the highest rate of TET occurs when the bandgaps of the PbSe NCs are resonant with the T<sub>1</sub> state of pentacene (0.86 eV).<sup>24</sup> However, in our hands, smaller NCs gave higher upconversion QYs due to the larger driving force for TET ( $\Delta G^0$  in Fig. 1.1d). The same trend was observed in two different combinations of NC and acene, i.e. PbX (X = S, Se) sensitized NIR upconversion<sup>35</sup> and CdSe sensitized conversion of green to violet light.<sup>34</sup> This discrepancy may be due to the higher density of states in the NCs that can accept triplets from acenes, compared to the reverse process where the T<sub>1</sub> acceptor state on the acene is a discrete state that can only accept one exciton. More work has to be done to increase understanding on the fundamental aspects of TET across this hybrid interface.

A transmitter ligand can greatly enhance photon upconversion QYs in this hybrid platform by creating an energy cascade between the sensitizer and annihilator, and facilitating the orbital overlap required for efficient Dexter transfer. For example, we have shown that the **9-ACA** transmitter enhances CdSe sensitized photon upconversion by 3 orders of magnitude,<sup>25</sup> and a tetracene derivative, 4-(tetracene-5-yl)benzoic acid, **CPT**, enhances photon upconversion QY by 81 and 11 times for PbS and PbSe NCs respectively.<sup>36</sup> The upconversion QYs were found to be exponentially dependent on the distance between NCs and transmitter when this distance was varied as a function of the number of *p*-phenylene units bridging CdSe donors and anthracene acceptors. Thus the anthracene transmitter with the shortest bridge has the highest upconversion QY of 14.3% for the conversion of green to violet light for this hybrid platform so far.<sup>37</sup>

In order to improve the upconversion QYs,  $\Phi_{UC}$ , the efficiency of each elementary step in Fig. 1.2 should be considered: (1)  $\Phi_{ISC}$ , intersystem crossing (ISC) within the NC, (2)  $\Phi_{TET}$ , TET from NCs to transmitters, (3)  $\Phi_{TTA}$ , TTA between two annihilators, and finally (4)  $\Phi_A$ , the fluorescence quantum yield of the annihilators. The efficiency of TET from transmitters to annihilators is not a factor in solution because Schmidt and Castellano have shown it is close to unity when the concentration of the annihilator is high.<sup>38</sup> For example, for transmitters with triplet lifetimes exceeding 10  $\mu$ s, the annihilator concentration of 10 mM leads to a near-unity efficiency in the TET from transmitters to annihilators.<sup>39</sup> As discussed above, firstly, trap states on the NC need to be passivated in order to maximize  $\Phi_{ISC}$ . Secondly,  $\Phi_{TTA}$  can be increased if the higher order excited states of the annihilators are energetically inaccessible at RT. Standard spin statistics predict an efficiency of 1/9 for TTA, but usually the efficiency of TTA is higher because the high energy quintet states are not accessible.  $\Phi_{TTA}$  is 0.52 for **DPA**,<sup>40,41</sup> and 0.33<sup>42</sup> for rubrene. Thirdly, molecules with high PL QYs meet the requirements for sensitizers, such as the PL QY of 0.90<sup>43,44</sup> for **DPA**, and 0.98 for rubrene.<sup>45</sup> Therefore,  $\Phi_{TET}$  is the bottleneck currently limiting the upconversion QY, since the other factors in Fig. 1.2 more or less stem from the intrinsic properties of the NCs or annihilators. To maximize  $\Phi_{TET}$ , we can synthetically tune the properties of transmitters to control the rate of TET from NCs to transmitters in terms of the binding group, the bridge, and the transmitter core, as shown in Fig. 1.2. This is discussed in the Section 1.3.

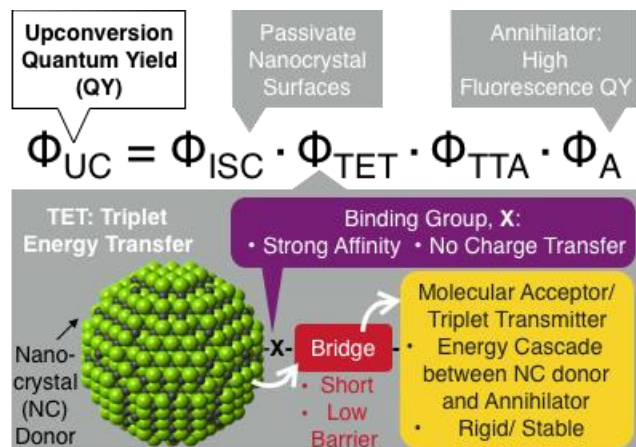


**Figure 1.2.** The upconversion QY,  $\Phi_{UC}$ , is a convolution of four factors, the efficiencies of: (1) intersystem crossing (ISC) within the NC,  $\Phi_{ISC}$ , (2) triplet energy transfer (TET) from NCs to transmitters,  $\Phi_{TET}$ , (3) triplet-triplet annihilation (TTA) between two annihilators,  $\Phi_{TTA}$ , and (4) the fluorescence quantum yield of the annihilators,  $\Phi_A$ . Strategies to enhance  $\Phi_{TET}$  from NC donors to molecular acceptors by synthetic control of the binding group, **X**, the bridge between the donor and acceptor, and the functionalized conjugated core of the transmitter are discussed in this Perspective.

### 1.3 Molecular design of transmitters

#### 1.3.1 Molecular energetics: Balancing the trade-off between upconversion QY and energy conservation

To date, triplet energy transfer from semiconductor NCs to a transmitter has been adequately modeled by the Dexter mechanism. It can be explained by Marcus theory.<sup>46</sup> In equation 1.1, the rate of TET,  $W_{ij}$ , relates to the energy offset between the triplet states of the NC donors and molecular transmitters,  $\Delta G^0$  (Fig. 1.1d), the reorganization energy  $\lambda$ , and the electronic coupling between the NCs and transmitters  $J_{ij}$ .

$$W_{ij} = \frac{|J_{ij}|^2}{h} \sqrt{\frac{\pi}{\lambda k_B T}} \exp \left[ -\frac{\lambda}{4k_B T} \left( 1 + \frac{\Delta G^0}{\lambda} \right)^2 \right] \quad (1.1)$$



By increasing  $\Delta G^0$ ,  $W_{ij}$  increases in the Marcus normal region to a maximum, then decreases in the Marcus inverted region. For TET from NCs to bound transmitters,  $\Delta G^0$  can be tuned by varying the size of NCs, and experimentally, higher upconversion QYs are obtained from smaller NCs.<sup>34,35</sup> This suggests that TET is in Marcus normal region. Along these lines, within the Marcus normal region, the triplet energy levels of transmitters should be lower than the dark excitonic state of the NCs, thus providing a driving force for higher  $\Phi_{TET}$ . The energy levels of the molecular transmitter used in photon upconversion can be tuned by varying the degree of conjugation<sup>47,48</sup>, or by varying the position and number of electron donating and withdrawing functional groups.<sup>47,49,50</sup>

There is a trade-off between the conservation of energy and the upconversion QY. A low lying  $T_1$  state in the transmitter leads to a high  $\Phi_{TET}$ , but this energy offset means not all the energy in the photons absorbed by the NC is utilized. Similarly, in DSSCs,<sup>51</sup> the energy levels of the dye molecules relative to the  $TiO_2$  conduction band are crucial for high performance. An efficient dye molecule should have molecular excited states with potentials sufficiently low for dye regeneration<sup>39</sup> and sufficiently high for electron injection into the conduction band of titania.<sup>47</sup> However the increased bandgap leads to a lower spectral coverage. The trade-off between open-circuit voltage and short-circuit current in DSSCs parallels the trade-off between photon upconversion QY and efficiency in this hybrid upconversion platform.

To minimize energy loss during upconversion, the triplet energy of the annihilators should be close to that of transmitters, and the energy level of the  $S_1$  state of the annihilators should be lower than, but close to twice their  $T_1$  energy for energy conservation. For

example, pentacene cannot be used as an upconversion annihilator because the 2.3 eV<sup>52</sup> energy of S<sub>1</sub> state is more than twice the energy of the T<sub>1</sub> state which is 0.86 eV,<sup>53</sup> thus three pentacene triplets would be required for TTA to be observed.

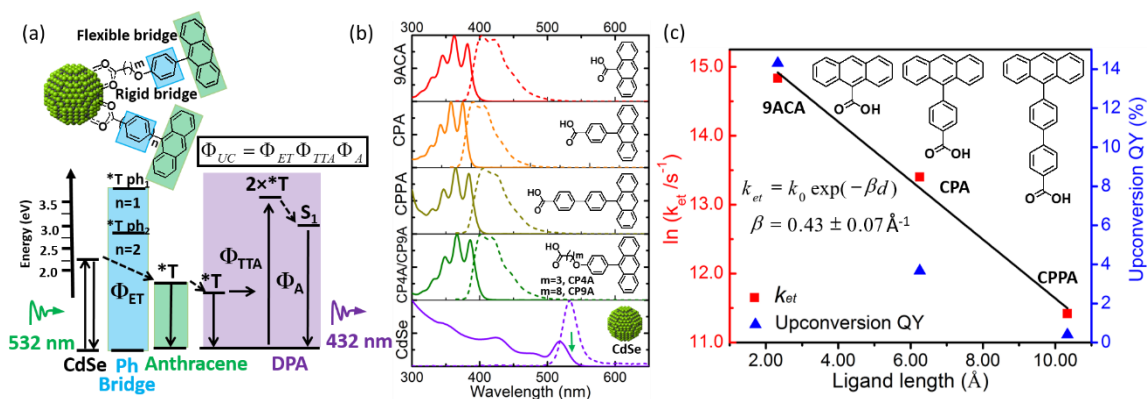


**Figure 1.3.** (a) Schematic of the energy transfer in the hybrid CdSe-anthracene photon upconversion platform. The energy diagram depicts the triplet excitonic states of the CdSe NC donor, the *p*-phenylene bridges when *n*= 1 and 2, and the anthracene acceptor, which also serves as the transmitter ligand. (b) Absorption (solid line) and fluorescence spectra (dotted line) for different transmitters and CdSe NCs. (c) The rate of triplet energy transfer ( $k_{et}$ , red squares) and the maximum upconversion QY (blue triangles) are shown versus the length of the phenylene bridge in the covalently bound anthracene transmitter ligands on CdSe nanocrystals. Reproduced from reference 33 with permission from the American Chemical Society.

### 1.3.2 Bulky or rigid transmitters with high fluorescence QYs.

The addition of phenyl or other rigid side groups to the conjugated core of the transmitter is proposed to enhance triplet energy transfer by decreasing vibrational relaxation. A good transmitter should have minimal pathways for excited electronic states to decay by vibrational relaxation. This is usually reflected in a high fluorescence QY. The idea is to minimize access to non-radiative decay pathways in TET from NC to transmitter and then to annihilators, thus increasing the upconversion QY. Bulky groups should also prevent excimer formation or triplet exciton quenching/ TTA between the two neighboring

transmitters bound to the surface of NC. We have seen that the upconversion QY increases then decreases with the surface density of transmitter ligands.<sup>36,37</sup> The initial increase is associated with an increasing number of transmitter ligands that facilitates energy transfer, while the drop is linked to excimer formation or inter-molecular TTA, both of which can be avoided by installing rigid, bulky transmitter ligands. Finally, by group theory arguments, molecular symmetry is directly related to the number of allowed vibrational modes that can couple to electronic states<sup>54</sup>, thus transmitters with higher symmetry may minimize coupling to vibrational states and increase overall TET efficiency.

### 1.3.3 Decreasing the tunneling barrier during TET

The upconversion QY is exponentially dependent on the distance between the NC donors and the transmitter. Li et al.<sup>37</sup> used oligo-*p*-phenylene bridges to covalently link anthracene acceptors to CdSe NCs. As shown in Fig. 1.3a, TET from CdSe NCs to the anthracene ligand is based on a tunneling mechanism through the phenylene bridges. By varying the length of this rigid phenylene spacer (Fig. 1.3b), the rate of TET from CdSe NCs to the anthracene core was found to be exponentially dependent on the length of the bridge, as described by the Dexter equation in Fig. 1.3c. Though the rates of triplet energy transfer showed this exponential dependence, the photon upconversion QYs didn't show the same trend. This is due to the different numbers of bound transmitters. Upconversion QYs were lower than expected for the transmitters with the phenyl bridges, **CPA** and **CPPA**. This is because these transmitters were less soluble than **9-ACA**, and fewer transmitters were bound to the CdSe donor surface, resulting in a lower overall rate of triplet energy transfer to the **DPA** annihilator. Therefore, due to the fact that Dexter transfer

should be optimized, a good transmitter should be designed to have a short distance between transmitter core and NCs. Dexter-type transfer is a short range interaction based on the wavefunction overlap between the donor and acceptor, usually occurring within 1 nm,<sup>37,55</sup> parameterized by  $\beta$ , the damping coefficient that describes the extent of coupling of the donor and acceptor through the barrier material. A higher  $\beta$  value means weaker coupling, which leads to a slower rate of energy transfer. The  $\beta$  value is dependent on the energy offsets between energy donor and acceptor, as well as the tunneling barrier and the length of the bridging units.<sup>56</sup> The  $\beta$  value of the rigid, aromatic phenyl groups is  $0.43 \text{ \AA}^{-1}$  for Dexter energy transfer for the thermodynamically downhill (0.5 eV) TET between the CdSe donor and anthracene acceptor in Fig. 1.3.<sup>37</sup> Interestingly, this attenuation factor is very close to the  $\beta$  value obtained from dinuclear heterometallic complexes with *para*-polyphenylene spacers. De Cola et al<sup>57</sup> report  $\beta = 0.50 \text{ \AA}^{-1}$  for triplet transfer from Ru(bipyridine)<sub>3</sub><sup>2+</sup> to Os(bipyridine)<sub>3</sub><sup>2+</sup> for  $\Delta G = -0.37 \text{ eV}$  and Barigelletti<sup>58</sup> report  $\beta = 0.33 \text{ \AA}^{-1}$  for a structurally related Ru(II)/ Os(II) complex. Acetylene, alkene, thiophene, *p*-phenylene ethynylene and *p*-phenylene vinylene bridges present lower tunneling barriers than the *p*-phenylene bridges explored in Fig. 1.3 and may result in lower  $\beta$  values.

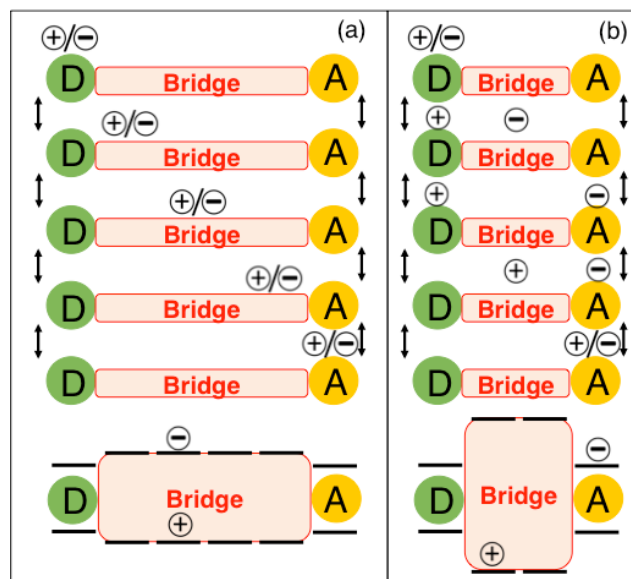


**Figure 1.4.** Dexter energy transfer across the bridge between the donor (D) and acceptor (A) can occur via two different pathways. (a) For long bridges or bridges with energy levels that may be resonant with the donor or acceptor, the triplet exciton moves across the bridge as an unseparated hole and electron.<sup>52</sup> (b) The Closs model where the triplet energy transfer consists of individual charge transfer events, typically through short bridges with high tunneling barriers.<sup>53</sup>

The length of the bridge and its tunneling barrier are anticipated to dictate the pathway for Dexter energy transfer. Skourtis and Beratan<sup>59</sup> predict that in the presence of long bridges that have energy levels resonant with a donor and acceptor, triplet energy transfer can occur via a bridge excitonic state that accommodates both the hole and electron simultaneously (Fig. 1.4a). Mechanistically, this is a departure from the Closs/ McConnell model,<sup>60</sup> where TET consists of two individual charge transfer events, with either the hole or the electron sequentially traversing virtual excitonic states in the bridge (Fig. 1.4b). Note that evidence for the Closs model mainly arises from aliphatic bridges with high tunneling barriers. It will be exciting to find experimental evidence of holes and electrons arising from triplets concurrently within the bridging aromatic ligands.

#### 1.3.4 Increasing the binding affinity of transmitters to NCs

The binding affinity of transmitter ligands for the NC surfaces is an important consideration, because at low ligand loadings,  $\Phi_{TET}$  is proportional to the number of bound transmitters per NC. Upconversion QYs decrease if the NC-transmitter complexes were cleaned more than once, or if good solvents for transmitter ligands are used to dissolve the isolated hybrid complex.<sup>34</sup> This is because the transmitter ligands can detach from the surface of NCs when exposed to good solvents. The higher the binding affinity of the transmitter ligand, or the semiconductor NC-transmitter bond strength, the more stable the NC-transmitter complex, the more easily the native ligands can be displaced. Generally, commonly used organic ligands on NCs can be classified as neutral L-type ligands that can datively bind to NCs (i.e. amines, pyridines and phosphine oxides) and anionic X-type ligands that covalently bind to NCs (e.g. carboxylates, thiolates, phosphonates). While carboxylic acids, thiols and phosphonic acids can be introduced as neutral molecules dissolved in organic solvent during ligand exchange, it is thought these ligands bind as X-type ligands in their deprotonated form.<sup>61</sup> Each functional group presents different binding affinities to the surface of NCs. Several studies<sup>62,63,64</sup> have measured the binding constants of ligands to CdSe NCs with NMR or via NC PL quenching methods. However, these equilibrium constants are not comparable because these values are dependent on solvent, concentration, native ligands, etc. Various computational methods<sup>65,66</sup> have been used to calculate the binding energies of a series of ligands to NCs. Generally, for CdSe NCs, the anionic X-type ligands bind stronger than neutral ligands, while L-type ligands bind weakly

and reversibly due to the weaker dative bond to the NC surface. The relative binding affinity can also be indicated by the ease of displacement of one ligand compared to another. In ligand exchange reactions, carboxylic acid ligands can be displaced by thiols or phosphonic acids, but the reverse process is not efficient.<sup>67,68</sup> Thiols can easily displace amine, trioctylphosphine oxide (TOPO), or trioctylphosphine (TOP) from NCs.<sup>69</sup> Pyridine is a weak binding group and can be easily displaced by aliphatic amines.

Instead of using weakly bound monodentate ligands, multidentate ligands can be used to strengthen the bonding to NCs. For example, in biological applications of thiol-capped CdSe-ZnS core-shell NCs, monodentate thiols bound on the ZnS shell are stable for a week.<sup>70</sup> The use of bidentate thiol-based ligands enhances the shelf lives of functionalized NCs from a few days to one year.<sup>71,72</sup> In a series of bidentate anthracene transmitters with pyridine binding groups, only one out of the three isomers gave a high photon upconversion QY exceeding 12% when paired with a CdSe NC sensitizer. The lower upconversion QY by the other two isomers (8% and 2.5%) shows that transmitter ligands can be designed to bind in a complementary ‘lock and key’ manner to NC surfaces. The bidentate binding geometry here increases orbital overlap and the efficiency of energy transfer.<sup>73</sup>

It is well known that the electrooptic properties of II-VI and III-V semiconductors are very sensitive to chemical perturbations of their surfaces.<sup>74</sup> In other words, energy transfer from NCs to transmitters may compete with charge transfer. Both result in the enhancement or quenching of NC PL and time-resolved TA or PL experiments are indispensable in identifying the loss mechanisms. For example, ligands that are initially

added may bind preferentially to dangling bonds,<sup>75</sup> thus enhancing the PL of NCs at low loadings. Kalyuzhny and Murray<sup>75</sup> found that thiols quenched CdSe NCs, while hexadecylamine, pyridine, TOP and TOPO enhanced the PL of CdSe NCs. Similarly, previous work indicated that thiol<sup>63,76</sup> and dithiocarbamate<sup>77</sup> ligands serve as a hole trapping agents for CdSe NCs, as they quench the PL of NCs dramatically. However, thiol ligands enhance the PL of CdTe NCs due to the higher level of the CdTe valence band.<sup>76</sup> Aliphatic amines are observed to enhance the PL of NCs, e.g. primary amines are found to enhance the PL more than secondary and tertiary amines<sup>63</sup> while aromatic amines quench NC PL by photoinduced hole transfer.<sup>78</sup> In a study of resonance energy transfer from CdS NCs to bound boron dipyrromethene (BODIPY) dye molecules,<sup>79</sup> both charge transfer and energy transfer were observed for the amino functionalized BODIPY. The specific location of the binding group on the conjugated core of the transmitter ligand affects the photon upconversion QY. 1-, 2- and 9- carboxylic acid or dithiocarbamate functionalized anthracene isomers lead to different rates of TET from CdSe NCs to bound anthracene ligands. This is because the isomeric substitutions either altered the relative levels of the higher order excitonic states in anthracene, or varied the orbital overlap between CdSe and anthracene, thus critically affecting the Dexter-based transfer.<sup>80</sup>

In the same way, in DSSCs, the anchoring group has a pronounced effect on the optical properties and energy levels of the dye molecules, e.g. electron withdrawing cyanoacrylic acid and carboxylic acid anchoring groups stabilize the complexes.<sup>81</sup> In addition, polar functional groups may affect the band structure of the inorganic photoanode. For example, some acidic anchoring groups can protonate the TiO<sub>2</sub> surface



which leads to an accumulation of positive charge and a lowering of the TiO<sub>2</sub> conduction bands.<sup>81</sup> Though the phosphonic acid group can bind on oxides more strongly, the rate of charge transfer is low compared to the carboxylic anchor because of the tetrahedral geometry of the phosphorus center.<sup>82</sup>

To sum up, anchoring groups that can strongly bind to NCs while preserving their photoinduced excitonic states are preferred, such as the carboxylic acid or phosphonic acid groups. Binding groups that result in intramolecular charge transfer or interfacial charge transfer between NCs should be avoided, e.g. thiols are undesirable even though they bind strongly to chalcogenide NCs. Multidentate transmitters are an unexplored class of ligands which should display a higher binding affinity and a more well-defined donor-acceptor geometry that will shed light on the factors affecting TET at this organic-inorganic interface.

### 1.3.5 Stability of the transmitter

The stability of the transmitter is important in TET. Currently, acene transmitters functionalized with anchoring groups are used.<sup>25,29,34,36,37</sup> As triplet transmitters, acenes have low-lying triplet states<sup>83</sup> and long triplet lifetimes<sup>28</sup> to allow energy to be efficiently transferred to the annihilator. It is well known that linear acenes with more than five fused rings, e.g. pentacene or hexacene are unstable because of Diels Alder reactions with ambient oxygen.<sup>84</sup> However slightly electron withdrawing alkynyl substitutions<sup>85</sup> stabilize the electron density in these linear fused acenes, making substituted hexacenes and higher order analogs isolable. Therefore, as transmitter ligands, substituted linear acenes are superior to their parent molecules in terms of stability and solubility.

Other stable, nonlinear polycyclic aromatic hydrocarbons such as pyrene<sup>86</sup> and perylene<sup>87</sup> may also be used as transmitters, while nitrogen containing chromophores like the perylene diimides or BODIPY class of molecules are possible alternatives. Some of these molecules have been used in molecular TTA upconversion as sensitizers or annihilators.<sup>88</sup>

## **Chapter 2    Hybrid molecule-nanocrystal photon upconversion across the visible and near-infrared.**

### **2.1    Introduction**

The sequential absorption of two low energy photons, followed by emission of one higher energy photon, is known as photon upconversion. This incoherent two-photon process has potential applications in biological imaging<sup>89</sup> and shown promise for high density data storage<sup>90</sup>. In solar energy conversion, photon upconversion has the potential to generate substantial gains in overall solar conversion efficiency, e.g. from 32% under the Shockley-Queisser limit to 43% under one sun for photovoltaic cells with a bandgap of 1.76 eV<sup>91,92</sup>. Two key challenges in the field are to find new upconversion materials that can operate 1) with high conversion efficiencies; and 2) in the near infrared (NIR) spectral region.

A successful approach to achieve efficient upconversion at low light intensities has been to use mixed conjugated organic systems in which triplet-triplet annihilation (TTA) can occur<sup>93-95</sup>. A sensitizer molecule absorbs a long wavelength photon, creating a singlet state that undergoes intersystem crossing to its triplet state, which then transfers its energy to the triplet state of a second molecule that acts as an emitter. When two sensitizers transfer their triplet states to the emitter, the two triplets can fuse into a higher energy singlet state on the emitter. Organic upconversion systems based on TTA can operate under low light conditions (equivalent to sunlight), have demonstrated upconversion efficiencies of up to 28%<sup>96</sup>, and have been used to upconvert photons at wavelengths as long as 790 nm<sup>97</sup>.

Unfortunately, it has proved challenging to find photostable, long-lived organic chromophores that allow organic upconversion systems to operate beyond 800 nm. This NIR spectral region is of interest because commonly used photovoltaic materials like silicon (bandgap,  $E_g = 1.1$  eV) and cadmium telluride ( $E_g = 1.5$  eV), are unable to collect photons that have wavelengths exceeding 1100 and 800 nm respectively. Furthermore, NIR photons are only weakly absorbed in aqueous environments, making them useful for probing biological systems. Rare earth glasses have been used for NIR upconversion, but they have limited spectral coverage and low efficiencies due to the forbidden nature of the optical transitions in lanthanides employed for upconversion<sup>96,98</sup>.

Inorganic nanocrystals (NCs) are relatively photostable chromophores whose bandgap absorption spectra can be tuned from the near ultraviolet to the infrared. Previous reports of triplet energy transfer from organics to semiconductors suggest that it is possible for NC excitons to exchange energy with molecular triplet states.<sup>99</sup> A good example is the recent demonstration that triplet excitons produced by singlet fission in pentacene and tetracene layers can efficiently transfer their energy to adjacent semiconductor NC layers<sup>100,101</sup>. Evidence for the reverse process, i.e. energy transfer from the NC to the triplet state of an organic molecule, can be found in earlier experiments showing that CdSe NCs could sensitize singlet oxygen formation<sup>102</sup> and that the triplet state of a naphthyl ligand could act as an energy acceptor for NC excitons<sup>103</sup>. Although NCs were recently used as luminescence recyclers for a TTA upconversion scheme<sup>104</sup>, the use of semiconductor NCs as sensitizers for photon upconversion has not been explored. In this Letter, we show that NC-organic triplet sensitization is a robust phenomenon that can be optimized through

ligand chemistry. It has the potential to extend upconversion into the infrared spectral region, where it could be used to enhance the efficiency of commercially viable photovoltaic materials like CdTe and Si.

## 2.2 Results and discussion

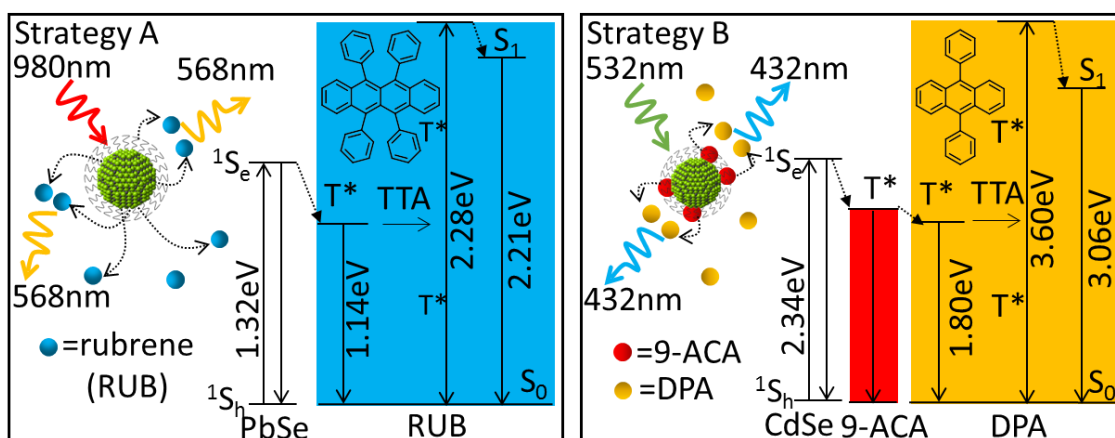


**Figure 2.1.** Schematic illustration of NC-organic upconversion strategies. In Strategy A, the organic ligands of the PbSe NC are electronically inert and energy must be transferred directly to the triplet state of the organic emitter RUB. In Strategy B, the energy is first transferred to the triplet state of an anthracene-based ligand, 9-ACA, which then transfers it to the DPA emitter.

The general idea of upconversion using NC sensitizers is outlined in Fig. 2.1. We illustrate two potential strategies. In Strategy A, the as-synthesized NC is surrounded by the native alkyl-terminated carboxylic acid or phosphonic acid ligands. Since these ligands do not have low-lying triplet states, energy transfer must occur directly from the NC to the emitter in solution. Given that triplet-triplet energy transfer is generally believed to require wavefunction overlap between acceptor and donor and operates on short ( $\sim 1$  Å) length scales, it is not clear that Strategy A could be successful with ligands that typically have alkyl chain lengths on the order of 10 Å or more. In Strategy B, the ligand itself has a

triplet state that can accept the energy from the NC exciton. The triplet state on the ligand acts as a transmitter that mediates triplet energy transfer from the NC sensitizer to an emitter in solution.<sup>105</sup> This strategy relies on an energy transfer cascade to move energy from the NC to the emitter. In this paper, we show both strategies work, but Strategy B with the energy cascade shows superior upconversion efficiencies.

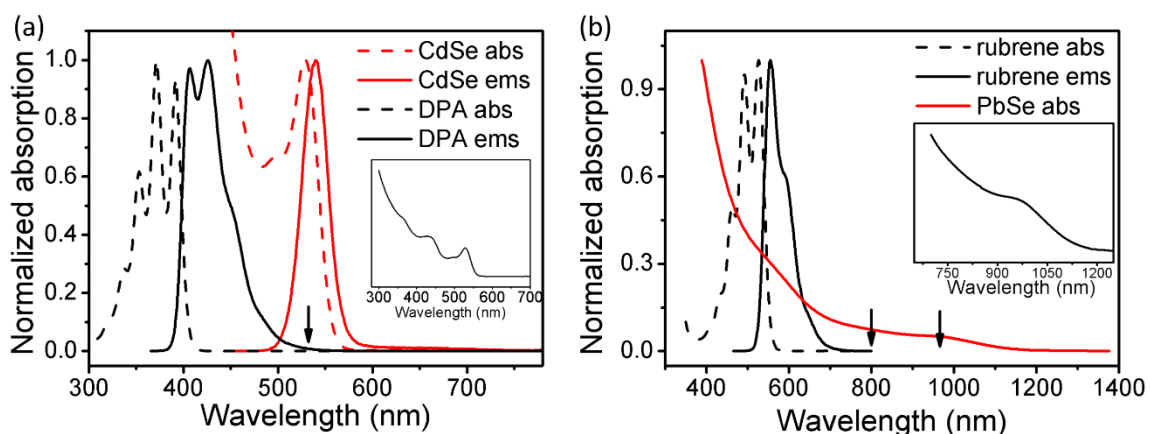


**Figure 2.2.** a) Absorption and emission spectra of 2.7 nm CdSe/DPA sensitizer/emitter pair in hexane at room temperature. Inset is the full absorption spectrum of CdSe b) Absorption and emission spectra of 2.1 nm PbSe/RUB sensitizer/emitter pair taken in toluene at room temperature. Inset is the absorption of PbSe's first exciton. Arrows indicate excitation wavelengths for photon upconversion.

As emitter molecules, we use diphenylanthracene (DPA) and rubrene (RUB). Both are commonly used in organic-organic upconversion schemes due to their long-lived, low-lying triplet states and high (>97%) singlet state fluorescence quantum yields<sup>106</sup>. As sensitizers, we use CdSe in combination with DPA to upconvert visible (532 nm) light to the blue region (DPA's emission peaks at ~450 nm) and PbSe in combination with RUB to upconvert the NIR (800-980 nm) to the visible (RUB's emission peaks at ~550 nm). The absorption and fluorescence spectra of both the NC sensitizers and the organic emitters are shown in Fig 2.2, along with the laser wavelengths used in the upconversion experiments

described below. Details regarding NC synthesis<sup>8,107,108</sup>, ligand exchange and characterization by NMR, quantum efficiency measurements, etc. can be found in the Chapter 8.

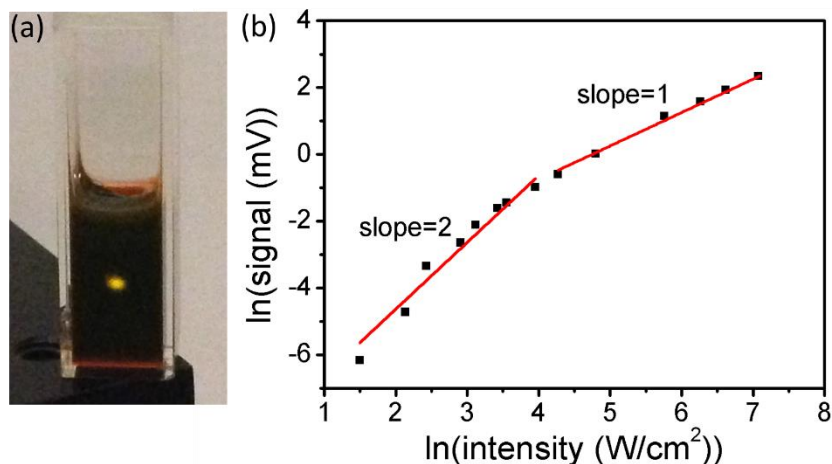


**Figure 2.3.** **a)** Photograph of upconversion in a cuvette containing the 2.1 nm PbSe/RUB mixture. The yellow spot is emission from the RUB originating from an unfocused cw 800 nm laser with an intensity of 1 W/cm<sup>2</sup>. **b)** Log-log plot of upconversion signal versus laser intensity (W/cm<sup>2</sup>) for the PbSe/RUB mixture, showing the transition from quadratic (slope = 2) to linear (slope = 1) regimes. (a) and (b) were conducted in dry and degassed toluene with 3.84 mM rubrene and 58.1  $\mu$ M PbSe NCs at room temperature.

Since one of our goals is to extend the spectral response of upconversion systems into the NIR, we first used 2.1 nm PbSe NCs capped with oleic acid ligands with RUB as the emitter. These samples gave visible upconversion, as shown in Fig. 2.3a. A bright yellow fluorescence originates from the spot where a 3 mm diameter, 100 mW 800 nm cw laser beam hits the sample. The black color of the cuvette is due to the PbSe NCs, whose absorption extends across the entire visible spectrum. The intensity dependence of the upconverted signal, shown in Fig. 2.3b, exhibits the signature linear-to-quadratic behavior seen in organic upconversion systems.<sup>109</sup> The absolute yield of the upconversion was

determined by comparing the RUB output from the upconversion to that from direct excitation of the RUB by 400 nm light. The upconversion quantum yield was  $1.0 \pm 0.5 \times 10^{-4}$  (or 0.01 %) in the linear intensity regime where the efficiency is maximized (Chapter 8). When a 980 nm laser diode was used to excite the sample, yellow upconverted light was also observed. The 980 nm source was not sufficiently intense to reach the linear regime, but the efficiency at this wavelength was estimated to be within a factor of 3 of that at 800 nm (Chapter 8). To our knowledge, 980 nm is the longest wavelength that has been upconverted using the triplet-triplet annihilation strategy. While the efficiency is lower than the 0.1% measured for nanosized  $\text{NaYF}_4:20\% \text{Yb}, 2\% \text{Er}$ , irradiated at 980 nm<sup>110</sup> with an intensity of 150 W/cm<sup>2</sup>, we emphasize that there are still many parameters that can be optimized in this system, including the implementation of Strategy B.

The TTA mechanism of upconversion was confirmed by time-resolved fluorescence measurements on the upconversion sample. Pulsed excitation at 800 nm leads to two RUB emission components, widely separated in time. Direct two-photon excitation of the RUB by itself leads to a prompt fluorescence decay on the nanosecond timescale. This fluorescence decay in the PbSe/RUB mixture is 14.3 ns, as compared to 16.2 ns measured for RUB by itself in toluene (Fig. 2.4a). Despite the high concentration of PbSe NCs, there is only a slight decrease in fluorescence lifetime that corresponds to a decrease in fluorescence yield from 98% (RUB by itself) to 86% in the mixed solution. On longer timescales, there is a delayed fluorescence component that



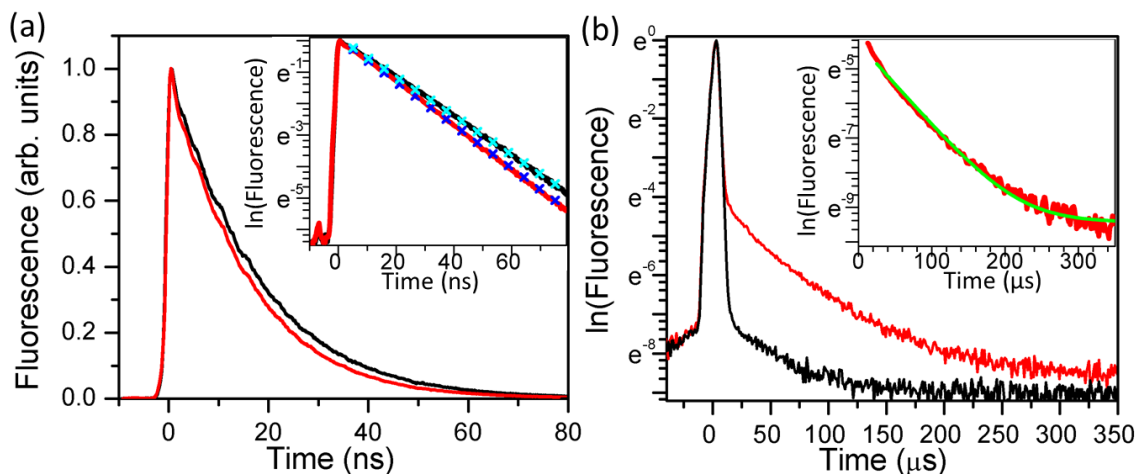


**Figure 2.4.** **a)** Prompt fluorescence decay of PbSe/RUB (red line) and RUB (black line) samples in a 100 ns time window. *Inset:* logarithmic plot of decay along with exponential fits (crosses). The singlet decay time decreases from 16.2 ns for RUB alone to 14.3 ns in the PbSe mixture. **b)** Logarithmic plot of the delayed fluorescence decay of PbSe/RUB (red) and RUB (black) samples on the  $\mu\text{s}$  timescale. The spike at time=0 is due to prompt fluorescence due to direct two-photon excitation of the RUB. *Inset:* logarithmic plot of delayed fluorescence component overlaid with fit with 41  $\mu\text{s}$  decay time and a 5% offset.

decays with a 41  $\mu\text{s}$  time constant (Fig. 2.4b) that is entirely absent in the RUB-only sample. The delayed fluorescence arises from the fusion of pairs of RUB triplets formed by energy transfer from the excited PbSe NCs. If we assume that most of the PbSe  $\rightarrow$  RUB energy transfer occurs within the  $\sim 1$   $\mu\text{s}$  lifetime of the luminescent exciton in PbSe<sup>111</sup>, then the delayed fluorescence reflects the RUB triplet lifetime. In the limit of bimolecular triplet encounters, the delayed fluorescence lifetime is half the triplet lifetime, allowing us to estimate a RUB triplet lifetime of 82  $\mu\text{s}$  in the mixed solution. This lifetime is close to the 120  $\mu\text{s}$  lifetime reported for RUB in nonpolar liquids<sup>112</sup>, indicating that quenching of the RUB triplet state is not pronounced in the mixed solution. Note that there is a small (5%) component of the delayed fluorescence that persists for much longer times, as can be seen

from the fact that some upconversion signal is detectable even at 300  $\mu$ s. Energy transfer from the PbSe NCs to the RUB is the dominant process in these mixed solutions, despite the fact that the PbSe sample has lower energy states that can accept energy from both RUB's singlet and triplet states.

We can make some general observations about the physical mechanism of the NC sensitization of the molecular triplet states. Both experiment and theory have shown that quantum confinement in semiconductor NCs leads to a dark state with triplet character just below the optically allowed state<sup>113-115</sup>. Energy transfer from this state to the molecular triplet state would be spin-allowed. The participation of long-lived dark NC exciton states is supported by the presence of a minor (5%) long-lived component in the RUB delayed fluorescence (Fig. 2.4b), which suggests that some state is supplying energy to RUB long after the optically bright exciton state has decayed.

Triplet-triplet energy transfer typically occurs via a Dexter mechanism that relies on wavefunction overlap. One way to enhance wavefunction overlap is to increase the extent of the excitonic wavefunction beyond the NC surface. Previous work on charge transport in NC arrays has shown that wavefunctions of particles with smaller effective masses can extend well beyond the NC surface<sup>116-118</sup>. Small carrier effective masses lead to larger exciton Bohr radii. By this logic, a larger Bohr radius should lead to a larger evanescent component of the exciton wavefunction and more efficient Dexter energy transfer. As a preliminary test of this idea, we compared PbSe (Bohr radius = 46 nm) to PbS (Bohr radius = 18-20 nm). We found that under identical conditions (absorption at 800 nm, laser power, RUB concentration), the PbS upconversion output was consistently

a factor of 3.5-3.8 times less than that of the PbSe sample. This observation lends qualitative support to the hypothesis that the Böhr radius is important, but more work needs to be done to assess factors like ligand binding and exciton relaxation in the different semiconductors.

The low upconversion efficiency of the PbSe/RUB system provided motivation to identify strategies that can increase its efficiency. Strategy B provides a promising way forward, but the design and synthesis of organic ligands with triplet energy levels appropriate for PbSe is a challenging problem. This synthesis is currently underway. In the meantime, we have used the CdSe/DPA combination as a model system to demonstrate that Strategy B is a viable way to enhance upconversion yields by the required amount.

When octadecyl phosphonic acid (ODPA) is used as the ligand for 3.3 nm diameter CdSe NCs, there was no detectable emission from DPA under 532 nm laser excitation (Chapter 8). This experiment corresponds to Strategy A in Fig. 2.1, and it appears that energy transfer across the ligand shell is even less efficient than in PbSe/RUB, placing an upper bound on the quantum yield of  $1 \times 10^{-4}$ . The arguments used above to explain the difference between PbSe and PbS also predict that CdSe (Böhr radius = 4-5 nm) would show very little upconversion, as observed.

To facilitate energy transfer, we replaced the ODPA ligands with anthracene derivatives functionalized with carboxylic acid groups. The use of the anthracene ligands enhances the DPA emission by roughly a factor of  $\sim 10^3$ , resulting in a blue fluorescence

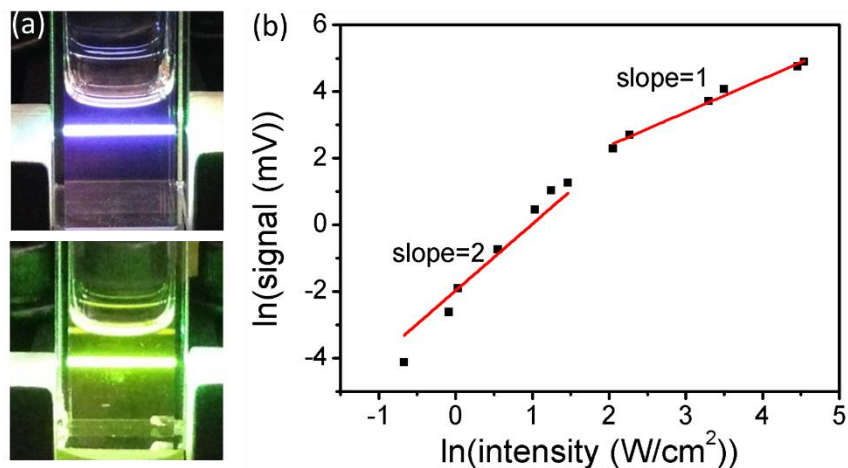


**Figure 2.5.** a) Photographs of upconversion in a cuvette containing an optimized CdSe/9-ACA sample (top) and a CdSe/ODPA sample (bottom). The spectra of these samples are shown in the Chapter 8. The violet DPA output in the 9-ACA sample (top) swamps the green CdSe emission and laser scatter that is clearly seen in the ODPA sample (bottom). (b) Log-log plot of upconversion versus laser intensity for the 3.3 nm CdSe/9-ACA/DPA sensitizer/ligand/emitter system, showing the transition from quadratic (slope = 2) to linear (slope = 1) regimes. All experiments were conducted in dry and degassed hexanes respectively with 1 mM DPA and 5  $\mu$ M CdSe NCs at room temperature.

output that is easily visible by eye using a 532 nm laser (Fig. 2.5a). The dependence of the DPA emission on laser intensity (Fig. 2.5b) again shows the quadratic-to-linear transition seen in organic upconversion systems. The best performance was obtained for 9-anthracene carboxylic acid (9-ACA). Shown in Fig. 2.6a is a comparison of the relative output levels for the five ligands tested at high laser power. Using Rhodamine 6G as fluorescence standard, we calculated an overall conversion efficiency of  $9 \pm 2\%$  for the 2.7 nm CdSe/9-ACA/DPA system (Chapter 8). Time-resolved fluorescence measurements on the CdSe/DPA mixtures confirmed that the DPA singlet lifetime is unaffected by the presence of the NCs. We note that this system still has room for further efficiency gains by modifying the NC size or geometry, ligand structure, and emitter molecule.

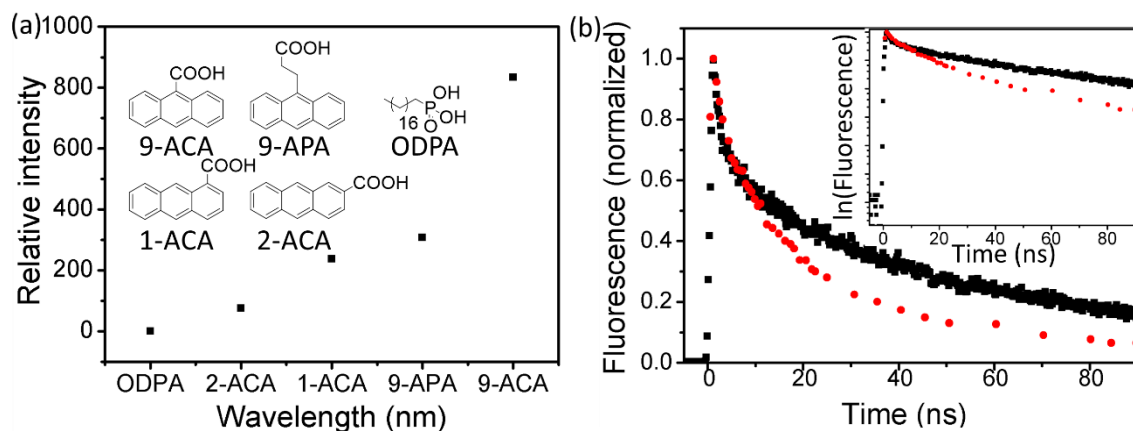


**Figure 2.6. a)** The relative upconversion efficiency with different transmitter anthracene ligands and the ODPA ligand attached to the CdSe NCs in toluene. **b)** Decay of CdSe/ODPA sample (black) and extracted CdSe component from CdSe/9-ACA sample (red). Details of the data analysis can be found in the Chapter 8. *Inset:* Logarithmic comparison of the decays.

To explain the enhanced upconversion, our hypothesis is that the anthracene-COOH ligands form an energy cascade outlined in Strategy B in Fig. 2.1. Given the CdSe bandgap of  $18870 \text{ cm}^{-1}$  (or 2.34 eV), as estimated from the PL peak, the triplet energy of 9-ACA ( $14760 \text{ cm}^{-1}$  or 1.83 eV) and the triplet energy of DPA ( $14290 \text{ cm}^{-1}$  or 1.77 eV)<sup>83</sup>, there is a downhill path for the energy from the CdSe to the 9-ACA to the DPA. To confirm that the anthracene ligands act as intermediate energy acceptors, we measured the PL lifetimes of CdSe NCs with and without the 9-ACA ligand. The results (Fig. 2.6b) show that this ligand generates substantial quenching of the NC photoluminescence on timescales  $>10 \text{ ns}$ . The observed shortening of the CdSe lifetime, combined with the large enhancement in upconversion efficiency, prove that Strategy B is an effective strategy to enhance energy transfer from the semiconductor NC to the emitter triplet state.

Finally, we consider why the emissive singlet states of RUB and DPA are not quenched by the NC sensitizers. The Förster radii for RUB $\rightarrow$ PbSe and DPA $\rightarrow$ CdSe

energy transfer lie in the 5-6 nm range (Chapter 8). If the RUB singlet state is excited while in close proximity to the NC, we would expect substantial fluorescence quenching. But given a diffusion coefficient of  $10^{-5} \text{ cm}^2/\text{s}$ <sup>119</sup> and a triplet lifetime of 80  $\mu\text{s}$ , the RUB can diffuse more than 100 nm after its triplet state is populated by the PbSe exciton. The long triplet lifetime allows it to escape the critical Förster radius around the PbSe NC. Similar considerations apply to the CdSe/DPA system. The weak nonradiative quenching of the emitters means that there is no fundamental limit on the ability of the emitter molecules to emit upconverted photons. However, we note that radiative transport of these photons through an absorbing sample may make it challenging to extract the upconversion output.

### **2.3 Conclusion**

The results of this Letter show that the use of inorganic NC sensitizers is a viable strategy for extending upconversion into the NIR spectral region. The ability of the PbSe/RUB system to upconvert 980 nm light to 550 nm opens up the possibility of using upconversion to enhance the efficiency of photovoltaic materials like GaAs and CdTe. Furthermore, we have demonstrated that using conjugated organic ligands, rather than standard alkyl ligands, can lead to an energy cascade process that enhances the overall upconversion efficiency by up to three orders of magnitude in the CdSe/DPA system. Extending this strategy to the PbSe/RUB system provides a clear path for making hybrid organic-inorganic nanomaterials that can upconvert infrared photons with high efficiency.

## Chapter 3 Ligand enhanced NIR photon upconversion

### 3.1 Introduction

Multi-excitonic processes can be harnessed to reorganize the energy contained in light in order to improve the performance of photovoltaic devices or photocatalysts.<sup>1</sup> Reshaping the solar spectrum to match the optical properties of common semiconductors will allow the efficient use of all incident light. While many efforts e.g. hot carrier devices,<sup>2</sup> intermediate band<sup>3</sup> or multi-exciton generation solar cells,<sup>4</sup> offer a route to manipulating incoming photons, the conversion of low energy near-infrared (NIR) photons to higher energy photons is particularly appealing, especially when considering NIR radiation comprises 53% of the solar spectrum.

The upconversion of NIR photons at the solar flux has not been demonstrated. If this formidable challenge is met, sub-bandgap photons that are currently not absorbed by common semiconductors can be utilized. Photon upconversion is predicted to increase the power conversion efficiency of a single *p-n* junction silicon solar cell from 28% to 43%,<sup>5</sup> beyond the Shockley-Queisser limit<sup>6</sup>. Currently, the upconversion of incident photons at power densities commensurate with the solar flux has only been demonstrated for the conversion of green to violet light, via a triplet-triplet annihilation (TTA) based mechanism.<sup>7</sup> This is because other upconverting platforms, like the lanthanides<sup>8</sup> or the chromophores for multi-photon absorption<sup>9</sup> (used in bioimaging) require high excitation densities for appreciable efficiency. TTA-based photon upconversion can be efficient when molecular<sup>120-122</sup>

or nanocrystal<sup>11</sup> (NC) light absorbers are used to sensitize triplet states on molecules. For molecular sensitized upconversion, triplets are created via intersystem crossing. In NC sensitized upconversion, triplet energy transfer was observed from NC to molecular triplet states<sup>11</sup> and later confirmed with transient absorption spectroscopy.<sup>27</sup> Two triplets can encounter each other and undergo TTA to emit a high-energy photon. Internal upconversion quantum yields (QYs) as high as 35-36%<sup>13</sup> and 10%<sup>11</sup> have been reported for the upconversion of green to violet light with palladium porphyrins and CdSe NCs as sensitizers respectively. However, in terms of harvesting NIR photons, molecular sensitizers that absorb strongly in the NIR generally have low fluorescence QYs due to strong internal conversion,<sup>14</sup> as predicted by the energy gap law. In contrast, the size, shape and material dependent optical properties of NCs make them ideal as light absorbers for photon upconversion, and It has been recently demonstrated that PbS or PbSe NCs are able to serve as NIR sensitizers in solution<sup>11</sup> and thin film.<sup>123</sup>

Here, we report that specially designed tetracene-based transmitter ligands can vastly increase the upconversion QY of NIR photons in a hybrid nanocrystal-molecular platform. Using the tetracene derivative 4-(tetracen-5-yl)benzoic acid or **CPT** (Fig. 3.1a), the upconversion QY increases from 0.021% (as synthesized NCs) to 1.7% (for NCs functionalized with **CPT**) using PbS NCs as the light absorbers, or sensitizers, and rubrene, as the light emitter, or annihilator. The corresponding increase in upconversion QY for PbSe NCs is 0.20% to 2.13%. For the first time, we demonstrate the potential of transmitter ligands to enhance the upconversion of



NIR photons, with an 81-fold and 11-fold enhancement for PbS and PbSe respectively. This rationally designed transmitter ligand addresses the problem of poor energy transfer in the original NC-rubrene platform<sup>11</sup>, and shows a clear path towards obtaining high QYs for the upconversion of NIR light, unhindered by the limitations of molecular light absorbers. The upconversion QY obtained here is the highest reported in the literature for TTA-based photon upconversion achieved without using precious metals.

### 3.2 Results and discussion

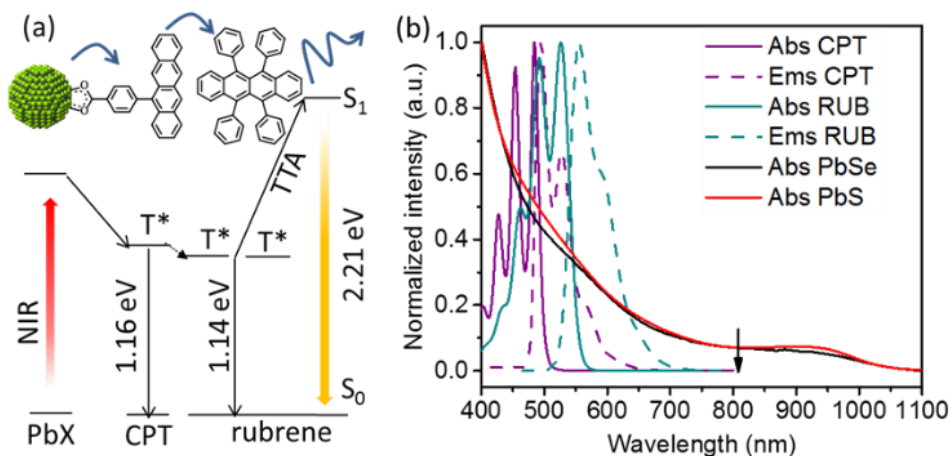
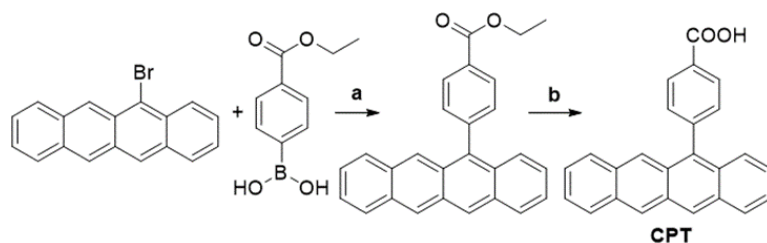


**Figure 3.1.** (a) Schematic of energy transfer during upconversion in this hybrid system with PbX (X=S, Se) as sensitizer, CPT as transmitter and rubrene as annihilator. (b) Absorption and emission spectra of CPT (purple), rubrene (dark cyan), 2.9 nm PbS (red) and 2.5 nm PbSe (black) in toluene at room temperature, with excitation wavelength (808 nm) indicated by the black arrow.

The components of this hybrid photon upconversion system and their optical properties are shown in Fig. 3.1. The first step in this upconversion scheme occurs when PbX NCs absorb a NIR photon (red arrow). Triplet energy transfer (TET) is enhanced in the presence of **CPT** directly anchored on the NC surface. TET

subsequently occurs between **CPT** and rubrene in solution. Two rubrene molecules then undergo TTA to emit a visible photon at 570 nm (yellow arrow). Here, a **CPT** scaffold is chosen as the transmitter because its  $T_1$  energy level is a little larger (1.16 eV, estimated from triplet energy of 5-phenyltetracene<sup>16</sup>) than that of rubrene,<sup>17</sup> thus forming a cascade for directional energy transfer. The absorption and emission spectra of the PbX NCs, **CPT**, and the rubrene annihilator are shown in Fig. 3.1b. **CPT** has a fluorescence QY of 0.53 and an extinction coefficient of  $9340 \text{ M}^{-1}\text{cm}^{-1}$  at its absorption maxima of 484 nm. The synthesis of **CPT** is shown in Scheme 1. 5-Bromotetracene<sup>18</sup> was used in a palladium catalyzed Suzuki cross-coupling reaction to give the esterified analog of **CPT**. Deprotection in KOH and repeated recrystallization in toluene/ THF afforded **CPT**. Ligand exchange was performed at room temperature in solution as outlined in the Chapter 8.



**Scheme 1.** Synthesis of transmitter tetracene derivative 4-(tetracen-5-yl)benzoic acid (**CPT**). Reagents and conditions: a) Cs<sub>2</sub>CO<sub>3</sub>, Pd(dppf)Cl<sub>2</sub>·CH<sub>2</sub>Cl<sub>2</sub>, toluene: H<sub>2</sub>O=3:1, 60 °C, overnight. b) 2 M KOH aqueous solution, THF:MeOH=1:1, reflux, 3h.

As shown in Fig. 3.2, for both PbS and PbSe, the number of **CPT** transmitter ligands bound per particle,  $n$ , correlates positively with the concentration of **CPT** in the ligand exchange solution (denoted as [CPT]<sub>LX</sub>). For 2.9 nm diameter PbS NCs,  $n$  varies from 14 to 45 as [CPT]<sub>LX</sub> is increased from 50 to 250 μM. The

corresponding transmitter ligand density increases from 0.53 to 1.7 nm<sup>-2</sup>. In comparison, there are 3 to 22 **CPT** ligands per 2.5 nm diameter PbSe NCs when [CPT]<sub>LX</sub> increases from 100 to 1000 μM, with ligand density ranging from 0.22 to 1.1 nm<sup>-2</sup>. The correlation between [CPT]<sub>LX</sub> and *n* was also confirmed by the photoluminescence (PL) quenching of 2.9 nm PbS. As shown in Chapter 8, with increasing [CPT]<sub>LX</sub> (ranging from 100 to 1500 μM), the PL of PbS was increasingly quenched, indicating very efficient energy transfer from PbS NCs to **CPT**. This estimate for *n* is obtained from the UV-Vis absorption spectrum of the PbX/ **CPT** complex that does not contain free ligand, taking into account the extinction coefficients of both the molecule and NC, assuming no charge transfer occurs (see Chapter 8 for details). The number of **CPT** transmitter ligands bound affects the solubility of the PbX/ **CPT** complex. Experimentally, it was impossible to redisperse the PbX-**CPT** pellet in toluene after centrifugation if [CPT]<sub>LX</sub> exceeded 1500 μM, and the PbX NCs would even spontaneously crash out of solution if [CPT]<sub>LX</sub> was over 2000 μM. Since **CPT** can effectively displace the native oleic acid ligands on the PbX NCs, the functionalized NCs no longer remain soluble if complete ligand exchange occurs. This is expected when the solubilizing long-chain hydrocarbons on the NC surface are completely replaced with the relatively insoluble **CPT**. The original oleic acid capped PbS and PbSe NCs have their surface saturated with carboxylic acid ligands with ligand densities of 3.0<sup>19</sup> and 4.2<sup>20</sup> nm<sup>-2</sup> respectively. The surface densities of **CPT** on PbS and PbSe NCs that lead to aggregating structures are 0.75<sup>19</sup> and 1.1<sup>20</sup> nm<sup>-2</sup> respectively, consistent with the fact that the

**CPT** molecule is around 4 times wider than oleic acid. Since the goal of this work is to establish ligand enhanced upconversion of NIR photons in solution, we used  $[\text{CPT}]_{\text{LX}}$  below 1500  $\mu\text{M}$ , where the PbS/ **CPT** complex remains soluble.

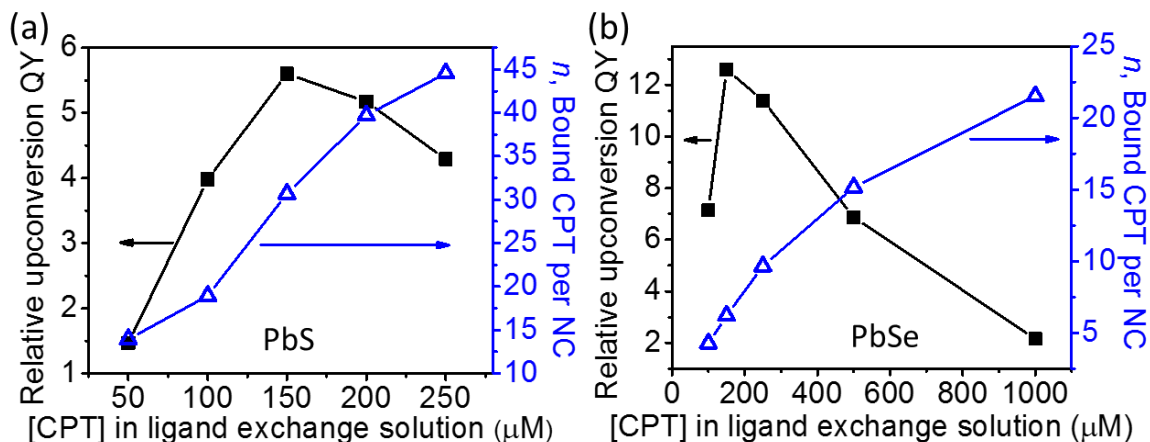


**Figure 3.2.** The relative upconversion QY is plotted with the upconversion fluorescence intensity normalized by the absorption at the excitation wavelength of 808 nm (black squares), and the number of bound **CPT** transmitter ligands per NC (hollow blue triangles) for (a) PbS, and (b) PbSe NC versus  $[\text{CPT}]$  in the ligand exchange solution. Both of the samples contain 1 mM rubrene and were measured in 200  $\mu\text{m}$  thick capillary tubes sealed in air-free cuvettes. Ligand exchange condition: PbS: stirring 10  $\mu\text{M}$  PbS with **CPT** in designated concentration for 40 min; PbSe: stirring 29  $\mu\text{M}$  PbSe with **CPT** in designated concentration for 20 min.

We found the upconversion QY reaches a maximum and then decreases as the number of bound transmitter ligands is increased (Fig. 3.2). Here, the relative upconversion QY is the upconversion fluorescence intensity of the rubrene emitter at 560 nm normalized by the absorption of the PbX NC at 808 nm. In Figure 2a and b, both PbS and PbSe sensitized upconversion show the highest relative QY at the optimal  $[\text{CPT}]_{\text{LX}}$  of 150  $\mu\text{M}$ . Since more **CPT** ligand is bound when  $[\text{CPT}]_{\text{LX}}$  is higher, the diminished upconversion at higher ligand loadings suggests that TET from **CPT** to free rubrene in solution is compromised. This suggests that the TTA

process may be occurring between two neighboring **CPT** molecules where newly introduced ligands may be aggregating together on the NC surface, as opposed to being randomly distributed. Comparing the TTA process between bound **CPT** and rubrene, TTA between bound **CPT** is undesirable because its fluorescence QY of 53% is significantly lower than the 98% of rubrene. In addition, emission from the singlet state of surface bound **CPT** may be quickly quenched due to rapid Förster energy transfer to the NC acceptor. For isolated **CPT**, energy transfer to free rubrene avoids quenching by the NCs.<sup>11</sup> For other reasons that are not clear, if too many transmitter ligands are installed, the upconversion QY decreases. Could it be that subsequent ligands bind to sites that result in a poor orbital overlap between the NC and the tetracene conjugated backbone? Or do these ligands bind to sites that behave as trap states for the triplet exciton? Unfortunately it is extremely challenging to interrogate the sites of bound ligands and their relative positions on the NCs to obtain a better understanding of the surface.<sup>21</sup>

To realize the maximum upconversion QY, other parameters such as the duration of ligand exchange, concentration of rubrene, and measurement setup was optimized. Other than  $[\text{CPT}]_{\text{LX}}$ ,  $n$  can also be controlled with the time allowed for ligand exchange. Chapter 8 includes the correlation between 2.5 nm PbSe sensitized upconversion QY and ligand exchange time. With 29  $\mu\text{M}$  PbSe and a fixed 150  $\mu\text{M}$  of  $[\text{5-CPT}]_{\text{LX}}$  in the ligand exchange solution, the highest upconversion efficiency was obtained after 5 min of stirring. A shorter or longer ligand exchange time leads to insufficient or too many **CPT** ligands per PbSe NC respectively. The

upconversion quantum efficiency plateaus when the ligand exchange time exceeds 15 min, indicating that equilibrium is achieved. The upconversion QY increases with the concentration of rubrene, as shown in Chapter 8, in accordance with reports in molecular visible upconversion systems.<sup>22</sup> Note that 20 mM is the solubility limit of rubrene in toluene. As shown in Fig. 3.1a, a high upconversion QY relates to efficient triplet energy transfer from **CPT** to rubrene, and the TTA between two rubrene molecules. The higher the concentration of rubrene, the more triplet rubrene formed, the higher the upconversion QY. Finally, to minimize the parasitic reabsorption of the upconversion signal by the NCs, the sample was put in a capillary tube with a thickness of 100  $\mu\text{m}$  and sealed in an air free 1 cm by 1 cm path length cuvette. The upconversion signal was measured in a front face geometry (see Chapter 8). Excitation power density dependence measurements were performed to confirm that all measurements occurred in the linear regime (Chapter 8).

$$\Phi_{UC} = 2 \times \Phi_{ref} \times \frac{(\textit{photons absorbed by reference})}{(\textit{photons absorbed by UC sample})} \times \frac{PL \textit{ signal}(UC \textit{ sample})}{PL \textit{ signal}(reference)} \quad (3.1)$$

With optimal conditions (see Chapter 8), the ligand enhanced upconversion was measured with an 808 nm laser on **CPT**-bound 2.9 nm PbS and 2.5 nm PbSe NCs in 20 mM rubrene. The upconversion QY,  $\Phi_{UC}$  is given by equation 3.1, where  $\Phi_{ref}$  is the single photon quantum yield of rubrene, excited by a cw 532 nm laser. Note that there is a factor of 2 in equation 3.1, so 100% QY is achieved when 50 upconverted photons are emitted with every 100 photons absorbed. For 2.9 nm PbS without the transmitter ligand, a QY of 0.021% was obtained. This upconversion

QY was enhanced by 81 times to 1.7% with the **CPT** transmitter covalently bound to the NC surface. For 2.5 nm PbSe, **CPT** enhances the upconversion QY 11 times from 0.20% to 2.1%. Note that the enhancement varies with rubrene concentration. While enhancements of 81 and 11 were obtained with 20 mM rubrene, over 200 times enhancement was observed when using 1 mM rubrene for 2.9 nm PbS NCs. As hypothesized, **CPT** binds on PbX NCs and forms the energy cascade described in Fig. 3.1a, so that energy is transferred to free rubrene molecules in solution more efficiently. The 2.1% QY is the highest reported value for TTA-based NIR upconversion. As demonstrated previously, in accordance with Kasha's rule,<sup>23</sup> this upconversion QY extends to all wavelengths of light absorbed by the NC, up to 1100 nm. This allows 43.8% more of the NIR region to be harvested compared to the maximum wavelength of 790 nm upconverted by molecular sensitizers.<sup>24</sup> Work is underway in this laboratory to improve this QY further by passivating the NC surface and investigating other molecular candidates for transmitters.

The use of transmitter ligands results in upconversion QYs enhanced by three orders of magnitude for CdSe NCs,<sup>11</sup> two orders of magnitude for PbS NCs, and an order of magnitude for PbSe NCs, a trend which is inversely related to their excitonic Bohr radius of 5 nm, 18 nm and 44 nm respectively. As triplet energy transfer from NCs to ligand molecules are based on the Dexter mechanism, the overlap of wave function is important. The inverse correlation between the Bohr radius of the NCs and ligand-based enhancement of the upconversion QYs supports the hypothesis that the Bohr radius relates to the delocalization of the excitonic wavefunction in

nanocrystals. Empirically, we observe that materials with a larger Bohr radius have higher upconversion QYs to begin with for the as-synthesized, unfunctionalized NCs, the subsequent transmitter-based enhancement of the upconversion QY is lower.

### 3.3 Conclusions

In conclusion, we have demonstrated that rationally designed transmitter ligands can enhance TET from PbX NCs to the triplet states of organic molecules, resulting in 1.7% and 2.1% upconversion QYs for PbS and PbSe NCs as the light absorbers. We show that the surface coverage of the **CPT** ligand on PbX NPs heavily influences the upconversion QY. This work lays the foundation for the molecular engineering required to improve this Dexter energy transfer process. For example, perhaps bulky structures that inhibit TTA between bound transmitter ligands may facilitate better TET between the NC light absorber and rubrene annihilator. In terms of practical applications, we expect the **CPT** functionalized PbS/PbSe NCs sensitizers to enhance the upconversion quantum yield in a thin film geometry as well.<sup>15</sup> Here the triplets are used for photon upconversion, but in principle, they could be directly extracted as electron-hole pairs in a solar cell. Antenna geometries, polymeric scaffolds and other supramolecular architectures could be harnessed to direct triplets efficiently from the NC to the annihilator, for high-performing, next-generation photovoltaic cells and photocatalysts.



## Chapter 4 CdSe Size and PLQYs in photon upconversion

### 4.1 Introduction

Photon upconversion refers to the absorption of low energy photons, and their subsequent emission as higher energy photons.<sup>124</sup> Compared to two-photon fluorescence or second harmonic generation, which depends strongly on peak intensity<sup>125,126</sup> and pulsed lasers for high efficiency,<sup>127</sup> photon upconversion can be accomplished using cw lasers or even incoherent light, like the sun. Photon upconversion is of particular interest for solar energy conversion, because it allows photovoltaics to harvest the unused sub-bandgap photons, and can contribute to the overall power conversion efficiency.<sup>128-135</sup> In terms of multiphoton imaging, exciting biological samples in the near infra-red (NIR) window with upconversion-based probes can minimize tissue autofluorescence and photodamage, as well as probe photobleaching.<sup>136-138</sup>

Until now, there were mainly two processes to achieve upconversion: lanthanide ion-based upconversion,<sup>139</sup> and molecular triplet-triplet annihilation (TTA)-based upconversion.<sup>88,140</sup> Lanthanide ion-based upconversion shows large anti-Stokes shifts and sharp emission lines, but low absorption cross sections,<sup>64</sup> limited tunability and therefore restricted spectral coverage. In TTA upconversion, while various molecules with high absorption cross-sections can have spectral ranges extending from the ultraviolet (UV) to the NIR,<sup>141</sup> it remains challenging to upconvert photons at wavelengths longer than 800 nm. In addition to lower photostability, organic dyes that absorb at these long wavelengths tend to undergo rapid internal conversion to the ground state, making them less effective as sensitizers.

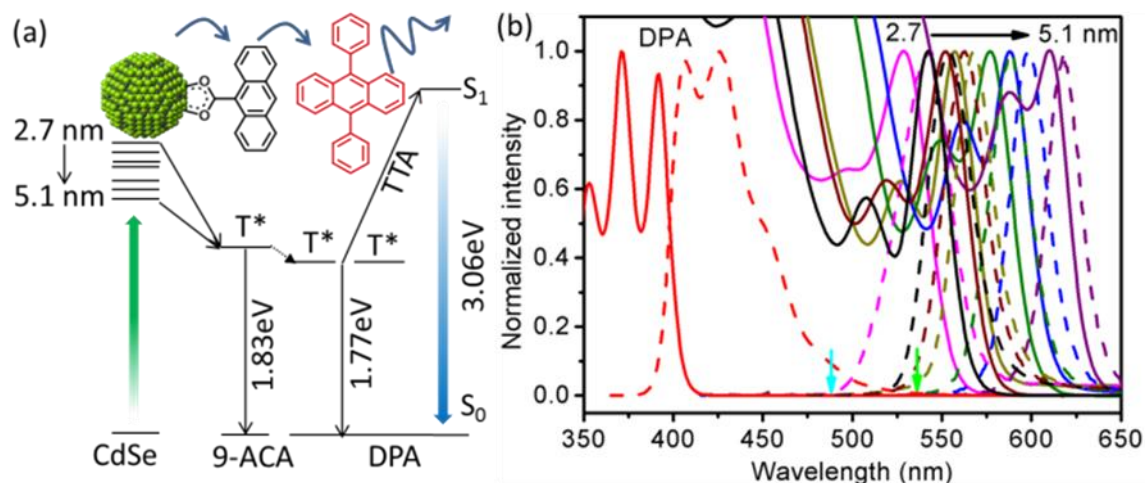


**Figure 4.1.** (a) In this hybrid system, the CdSe nanocrystals sensitizers are functionalized with a 9-ACA transmitter ligand. DPA serves as the annihilator. The green arrow indicates photo-excitation of CdSe NCs of different sizes, followed by energy transfer from CdSe to 9-ACA, then triplet-triplet energy transfer to DPA. Two DPA triplets annihilate to one singlet state and emit an upconverted photon (blue arrow). (b) Absorption (solid line) and emission (dashed line) spectra of DPA and CdSe NCs with 7 sizes measured in hexane at RT. Blue and green arrows indicate excitation wavelengths.

Recently, we discovered hybrid molecule-nanocrystal photon upconversion.<sup>25</sup> We found that semiconductor nanocrystals can effectively sensitize molecular triplet states which can undergo TTA and upconvert photons. Semiconductor nanocrystal sensitizers have the following advantages: 1) large absorption cross sections<sup>66</sup> compared to molecules, and especially when compared to lanthanide ions; 2) the ability to absorb light efficiently in the NIR;<sup>8-10</sup> 3) optical properties which are easily tuned based on the size and material properties of the nanoparticle.<sup>142</sup> Note that none of these properties are available simultaneously in the rare earth and molecular TTA systems. In fact, the tunable optical properties of nanoparticles, when combined with the vast selection of potential molecular annihilators, allow photon upconversion with this hybrid system to be engineered at

arbitrary wavelengths. However, much work needs to be done to investigate the fundamental processes underlying photon upconversion in this hybrid system.

Here, we examine the nanocrystal-based parameters affecting the upconversion of green to violet light using wurtzite CdSe NCs to sensitize the triplet states of anthracene derivatives, as depicted in Fig. 4.1a. We have hypothesized<sup>25</sup> that the relatively small Böhr radius of CdSe (4-5 nm) requires a transmitter ligand, such as 9-anthracenecarboxylic acid (9-ACA), directly anchored on the surface of these NCs to mediate the energy transfer to the annihilator, diphenylanthracene (DPA) in this case. We investigate the dependence of solvent, transmitter ligand density, NC photoluminescence quantum yield (PLQY), size and concentration on upconversion. This work sheds light on the mechanism of triplet energy transfer (TET) from CdSe NCs to organic molecules, and provides a guide to understanding and optimizing upconversion.

## 4.2 Results and discussion

In molecular upconversion systems, Monguzzi *et al.* has shown that there is a quadratic dependence on sensitizer absorption and excitation density when TTA is limited (equation 4.1), and a linear dependence when TTA is saturated (equation 4.2),<sup>143</sup>

$$S_A = 0.2 \frac{\gamma_{TT}}{k_A^S} \left[ \frac{k_{tr}}{k_D^T + k_{tr}} \right]^2 [\alpha(E)I_{exc}]^2 \quad (4.1)$$

$$S_A = 0.2 \frac{1}{k_A^S} \left[ \frac{k_{tr}}{k_D^T + k_{tr}} \right] \alpha(E)I_{exc} \quad (4.2)$$

where  $S_A$  is the concentration of annihilator molecules in the singlet excited state;  $\gamma_{TT}$  the second-order rate constant for TTA;  $k_A^S$  the singlet decay rate constant of the annihilator;

$k_{ir}$  is the rate constant of TET;  $k_A^T$  the triplet decay rate constant of the annihilator;  $k_D^T$  the triplet decay rate constant of the sensitizer;  $\alpha(E)$  the absorption coefficient of the sensitizer; and  $I_{exc}$  the laser intensity. In order to investigate the effect of sensitizer concentration/absorption, we varied the amount of 2.7 nm CdSe/9-ACA with a fixed concentration of 2.15 mM DPA in hexane. Fig. 4.2 plots the upconverted DPA emission versus nanoparticle absorption when excited by 488 and 532 nm cw lasers at constant intensity. It indicates that the upconversion photoluminescence is dependent on the light absorbed, which is proportional to NC concentration, as predicted.

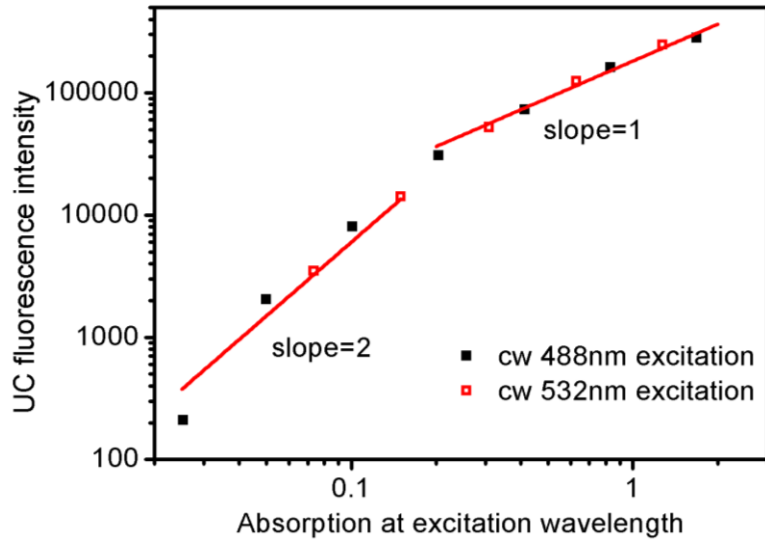


**Figure 4.2.** Log-log plot of the upconversion signal versus absorption at excitation wavelengths, showing the transition from quadratic (slope=2) to linear (slope=1) regimes. Measurements were conducted with 2.7 nm CdSe in dry and degassed hexanes at room temperature, with excitation wavelengths of 19.8 W/cm<sup>2</sup> 488 nm (black solid square) and 12.7 W/cm<sup>2</sup> 532 nm (red hollow square). The concentration of DPA is 2.15 mM.

A higher density of 9-ACA transmitter ligands on CdSe NCs leads to higher upconversion QY. Fig. 4.3a shows that upconversion is proportional to the concentration of 9-ACA in the ligand exchange solution. Here, five samples were prepared with 9-ACA

concentrations ranging from 1.6 to 15.4 mM in the ligand exchange solution. The more 9-ACA in solution, the more 9-ACA molecules bound to the CdSe NCs, and the more efficient the TET. Fig. 4.3b shows that upconversion is maximized in solvents that minimize solvation of the 9-ACA transmitter ligand. The upconverted PL with 2.7 nm CdSe/9-ACA and 1 mM DPA in 8 different solvents is shown. Since the CdSe NC/ 9-ACA samples were all prepared in the same flask, the only variable was the solvent used for upconversion. Fig. 4.3c shows the upconversion signal in Fig. 4.3b plotted against the solubility of 9-ACA in these 8 solvents. Good solvents for 9-ACA like THF (solubility limit: 813 mM) will dissociate the transmitter from the surface of CdSe NC. Hexane or toluene, with saturation concentrations of 0.016 and 1.909 mM respectively, are bad solvents for 9-ACA, so the 9-ACA transmitter molecules remain bound to the surface of CdSe NC, and upconversion is enhanced. The relatively low viscosity of hexane<sup>144</sup> may facilitate the diffusion of DPA and increase TTA. However, this solubility trend is not observed in halogenated solvents. It has been shown that aromatic fluorophores like anthracene can be quenched by CCl<sub>4</sub> due to the formation of a ground-state complex.<sup>[16]</sup> It is possible that in the halogenated solvents, there are two competing effects, solubility and singlet/triplet state quenching that preclude the observation of a clear trend. Finally, upconversion QYs decrease after excessive NC cleaning. If the CdSe-9ACA complex was resuspended in hexane and re-precipitated out with acetone, the upconversion QY does not increase but instead drops from 7.5% to 0.65% for 2.7 nm CdSe excited with 488nm light. This is because acetone used in the cleaning dissociates bound 9-ACA molecules from the nanoparticle surface, thus decreasing the TET rate. Note that the sensitivity to 9-ACA

surface density is due to the fact that we start with ODPa coated NCs which are resistant to displacement by carboxylic acids.<sup>68</sup>

**Table 4.1.** The diameter, optical properties, and upconversion QYs of the CdSe NC sensitizers.

Size (nm)	$\lambda_{\max}$ (nm) <sup>a</sup>		$E_g$ (eV) <sup>b</sup>	PLQY (%) <sup>c</sup>	Upconversion QY (%)	
	Abs.	Ems.			488 nm <sup>d</sup>	532 nm <sup>d</sup>
2.7	529	544	2.34	11	7.5	7.7
2.9	544	554	2.28	4.0	3.0	3.1
3.1	552	563	2.25	3.5	1.4	1.4
3.2	557	568	2.23	8.9	4.4	4.6
3.7	577	588	2.15	4.3	2.1	1.8
4.1	588	598	2.11	3.4	1.2	1.1
5.1	611	618	2.03	2.0	0.26	0.27

<sup>a</sup>In hexanes at RT; <sup>b</sup>optical gap as given by the absorption maxima; <sup>c</sup>NC photoluminescence quantum yield (PLQY), in hexanes at RT in air against R6G in ethanol (QY= 95%); <sup>d</sup>[DPA]=1.7mM, excitation with 19.8 W/cm<sup>2</sup> 488 nm and 12.7 W/cm<sup>2</sup> 532 nm cw lasers.

In addition to ligand coverage, the TET may also depend on the properties of the NCs, specifically NC size and PLQY. The absorption and emission spectra of CdSe NCs investigated are shown in Fig. 4.1b. Details on ligand exchange and sample preparation can be found in the Chapter 8. Proton NMR reveals that the 9-ACA transmitter ligand has a density around 0.1/nm<sup>2</sup> on the CdSe NC surface, in contrast to 1.3/nm<sup>2</sup> for the native ODPa ligands<sup>68</sup>. NMR shows no trend with respect to particle size, probably because NMR cannot distinguish between the free and bound 9-ACA ligands.<sup>145,146</sup> Fig. 4.4a shows the

upconversion photoluminescence spectra with 532 nm excitation (see Chapter 8 for 488 nm excitation).

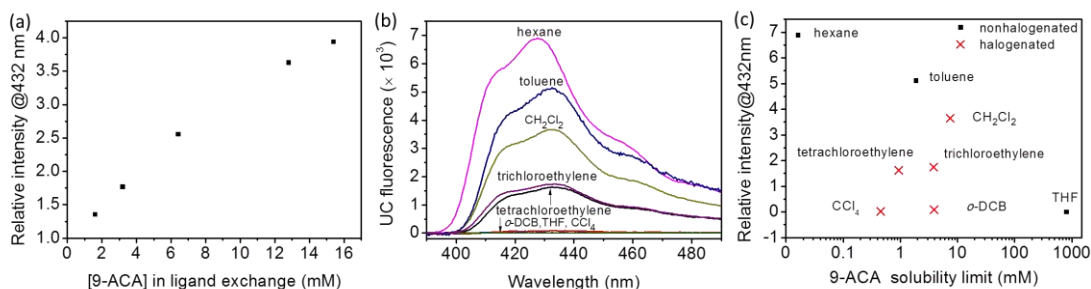


**Figure 4.3.** All measurements were conducted at RT with 1 mM DPA and a 532 nm laser at 12.7 W/cm<sup>2</sup>. (a) Upconverted DPA emission in toluene decreases as the concentration of 9-ACA transmitter in the ligand exchange solution with 3.2 nm CdSe NCs decreases. (b) Upconversion photoluminescence spectra of 1.5  $\mu\text{M}$  2.7 nm CdSe/9-ACA in different solvents. (c) The upconversion signal versus the solubility limit of 9-ACA in the solvents in (b).

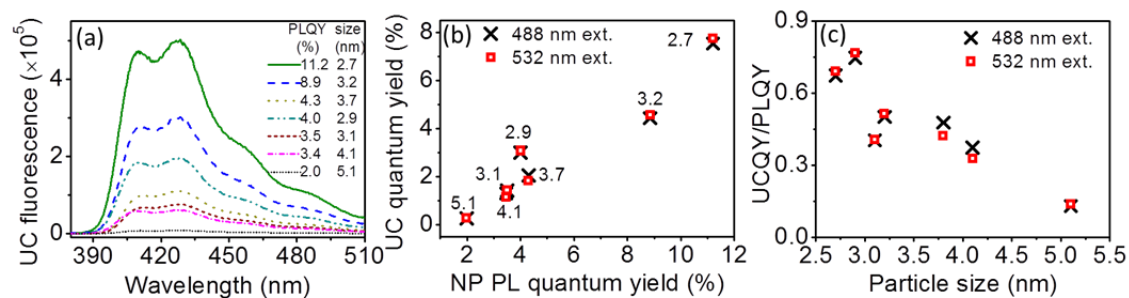


**Figure 4.4.** (a) Upconverted DPA photoluminescence spectra using CdSe NC sensitizers excited with a 12.7 W/cm<sup>2</sup> 532 nm cw laser. (b) Plot of upconversion QY versus CdSe NC PLQY, with the diameter (nm) of each NC labelled. (c) Plot of the UCQY normalized by PLQY versus size of CdSe NCs. All measurements were done with 488 nm (black cross) and 532 nm (red hollow square) excitation at RT with 2  $\mu\text{M}$  CdSe and 1.7 mM DPA in dry, degassed hexane.

Upconversion QYs at 488nm and 532 nm excitation are the same for each sample, in accordance with the Kasha-Vavilov rule.<sup>147</sup> Fig. 4.4b shows the upconversion QY of each sample plotted against CdSe NC PLQY, with particle size listed. Taken by itself, this

data suggests that upconversion efficiency increases with the increase in NC PLQY. When the upconversion yields are divided by the PLQY values in Table 4.1, we find that there is a systematic dependence on NC diameter, as shown in Fig. 4.4c, implying that the energy of the CdSe NC exciton does affect TET to the anthracene derivatives.

The dependence of upconversion yield on PLQY was investigated in more detail using NCs with the same size but different PLQY values. For example, 3.2 nm and 3.1 nm diameter CdSe NCs, with PLQY = 8.9% and 3.5 % respectively, give a corresponding upconversion QY of 4.4% and 1.4%. The particle diameters are quite similar, but the NC with lower PLQY showed lower upconversion QY. Indeed, 2.9 nm CdSe NCs size with low PLQY gave a lower upconversion QY than 3.2 nm and 2.7 nm CdSe samples with high PLQY (see Table 4.1). The PLQY depends inversely on the non-radiative decay rate. Non-radiative decay processes includes relaxation to dark excitonic states through intersystem crossing,<sup>148</sup> as well as trapping by the mid-gap states and surface states. While relaxation to the dark excitonic states with triplet character<sup>114,148,149</sup> may aid TET, nonradiative trapping to other states would compete with TET and decrease the efficiency of triplet energy transfer.<sup>150</sup> The nonradiative decay rate likely stems from the presence of surface defects, dangling bonds, unpassivated sites, nanoparticle stoichiometry, etc<sup>151-161</sup> whose exact role in determining the PLQY is not well understood. An increased NC PLQY may indicate fewer trap states to impede energy transfer, or a NC surface that better binds 9-ACA.<sup>79</sup>

Upconversion QY correlates inversely with size of the NCs. Particle size affects the bandgap energy of CdSe NCs, which in turn relates to the driving force for energy



transfer from particle to 9-ACA ligand. Here, 5.1 nm diameter CdSe have a bandgap of 2.03 eV, and the triplet state energy of 9-ACA is 1.83 eV.<sup>83</sup> If we assume that 9-ACA's highest occupied molecular orbital (HOMO) and the valence band of CdSe NC equilibrate, TET from the 5.1 nm CdSe still has a driving force of 0.20 eV. Thus our results indicate that driving energies greater than 0.2 eV result in energy transfer, which is in good accordance with molecular upconversion systems.<sup>38</sup>

### **4.3 Conclusion**

To conclude, the nanocrystal-based parameters affecting the upconversion QY of wurtzite CdSe/9-ACA/DPA sensitizer/ transmitter/annihilator were investigated using 7 CdSe NCs of different sizes and PLQYs ranging from 2.0% to 11%. In TTA-based upconversion, one of the steps that limits efficiency is the TET from sensitizer to transmitter or annihilator.<sup>44</sup> Our results indicate that more 9-ACA ligand on the CdSe surface leads to higher TET efficiency and higher upconversion QYs. In addition, upconversion QYs correlate with NC PLQYs and inversely with NC size. Therefore, NCs with high PLQYs and small sizes should be utilized. This work provides a guide to understanding, designing and synthesizing functional hybrid nanoparticle-molecular photon upconversion systems.

## **Chapter 5    PbS/CdS core/shell QDs suppress charge transfer and enhance triplet energy transfer yield**

### **5.1 Introduction**

It remains challenging to control light-matter interactions at the nanoscale. Compared to bulk materials, quantum confined semiconductor nanocrystals, or quantum dots (QDs), have tunable band gaps, strong and stable emission, and low thresholds for multiple exciton generation.<sup>117,151,162-164</sup> These properties make QDs potentially useful for solid-state lighting,<sup>165</sup> bioimaging<sup>166</sup> and next-generation photovoltaic applications.<sup>167</sup> More recently, QDs have been shown to be excellent triplet sensitizers for photon upconversion applications<sup>25,26,33</sup> because of the small energy difference between their singlet and triplet exciton states.<sup>148,168</sup> Efficient triplet energy transfer (TET) from CdSe QDs to molecular acceptors has been demonstrated.<sup>27,73</sup> However, efforts to achieve efficient sensitization in the infrared have been hampered in part by the competition of TET with other exciton decay pathways (such as electron or hole transfer and nonradiative recombination within the QD). Previous studies have shown that core/shell structures with type I or type II band alignment between the core and shell materials can be used to control the spatial distribution of the electron and hole.<sup>169,55</sup> This offers additional control of the rate of electron and hole transfer. In principle, such core/shell heterostructures can also be used to selectively suppress charge transfer and enhance TET processes.

Here, by introducing a sub-monolayer thick layer of cadmium sulfide on lead sulfide NCs, we demonstrate that the steady state photon upconversion quantum yield (QY) is enhanced by a factor of 1.4, from 3.5% to 5.0%. As presented in Fig. 5.1a, this photon

upconversion system consists of QD sensitizers (PbS or PbS/CdS), surface-bound transmitter ligands (5-carboxylic acid tetracene, or **5-CT**), and triplet annihilators (rubrene). To understand the mechanism for the efficiency enhancement, we carried out transient absorption (TA) spectroscopic studies on the exciton decay pathway in QD/**5-CT** complexes. We show that in the PbS/CdS core/shell heterostructure, the sub-monolayer CdS shell can suppress hot hole transfer processes, enhancing the efficiency of TET,  $\Phi_{TET}$ , from the QD donor to the transmitter ligand. Furthermore, the CdS shell also prolongs the lifetime of **5-CT** triplet excited state, which enhances the energy transfer efficiency from the transmitter to the triplet annihilator.

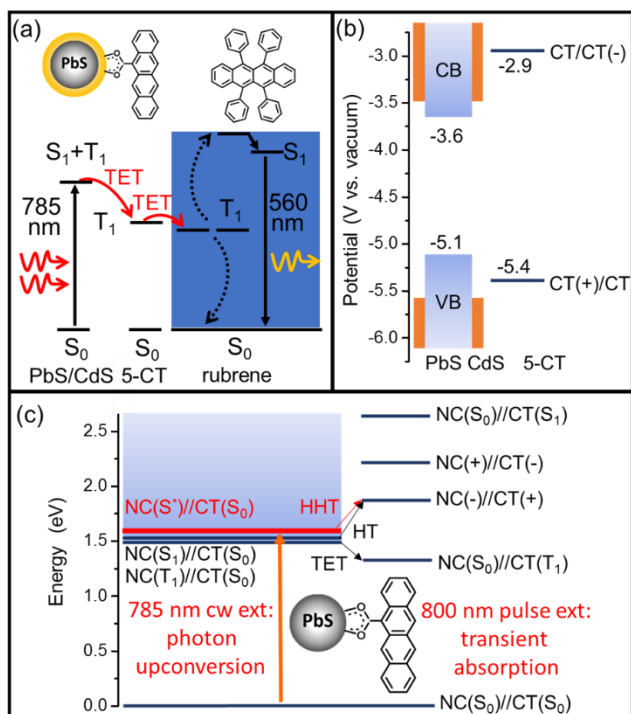


**Figure 5.1.** (a) Schematic of the energy transfer processes during photon upconversion using a hybrid PbS quantum dot (QD)-tetracene-rubrene platform. (b) Redox potential of PbS/CdS QD and **5-CT** (vs vacuum) measured by cyclic voltammetry in dichloromethane

at -50°C for the QD and RT for free **5-CT**. (c) Energy level of various energy and charge transfer states involved in the decay of QD excitons. Also shown is the initial excitation (orange arrow), hole transfer (HT), hot hole transfer (HHT) and triplet energy transfer (TET).

## 5.2 Results and discussion

The hybrid inorganic/organic platform for photon upconversion is shown in Fig. 5.1a. Photoexcitation of the QD with a 785 nm CW laser results in energy transfer to the triplet state of the bound **5-CT**, then to rubrene. Two rubrene triplets then annihilate to form a singlet-excited state that radiatively decays by emitting an upconverted photon at 560 nm. Two different QD sensitizers or light absorbers, 2.7 nm diameter PbS QD and 3.2 nm diameter PbS/CdS core-shell QD with native oleic acid ligands, are synthesized according to a literature procedure.<sup>33,35,170,171</sup> The similar absorption and emission maxima,  $\lambda_{\text{abs}}$  and  $\lambda_{\text{ems}}$  respectively, of the QDs (Table 5.1 and Chapter 8), indicate that they have approximately the same PbS core size. In our previous work, we have shown that photon upconversion is enhanced with smaller QDs because of the larger driving force for TET from QD donor to molecular acceptor.<sup>34,35</sup> In this work, PbS QD donors with the same absorption maxima allow the role of the CdS shell to be isolated. As a transmitter, the low-lying, long-lived triplet state of **5-CT** mediates TET from the QD to rubrene by forming an energy cascade (Fig. 5.1a). We have chosen rubrene as the annihilator because of its high singlet state photoluminescence QY (98%).<sup>45</sup> The absorption and emission spectra of the QD, **5-CT** and rubrene are shown in Chapter 8. When mixed with 20 mM rubrene emitter in toluene, the two **5-CT** functionalized light absorbers, i.e. PbS core only QDs and PbS/CdS core/shell QDs, give photon upconversion QYs of 3.5% and 5.0% respectively. Photon upconversion is optimized by varying the concentration of **5-CT** during ligand

exchange (See Chapter 8 for details). The upconversion QYs and other parameters relating to TET are summarized in Table 5.1. The photon upconversion QY of the three component system is 80 times higher than two component system of QDs and rubrene (without transmitter).<sup>36</sup>

**Table 5.1.** Key parameters for the hybrid photon upconversion system: absorption maxima,  $\lambda_{\text{abs}}$ ; emission maxima,  $\lambda_{\text{ems}}$ ; average number of bound 5-carboxylic acid tetracene (5-CT) per QD, N; photon upconversion quantum yield (UCQY); efficiency of triplet energy transfer (TET) from QD to 5-CT,  $\Phi_{\text{TET}}$ ; and the rate of TET,  $k_{\text{ET}}$

QD	$\lambda_{\text{abs}}$ (nm)	$\lambda_{\text{ems}}$ (nm)	N <sub>a</sub>	UCQ Y (%) <sub>b</sub>	$\Phi_{\text{TET}}$ (%) <sup>c</sup>	$k_{\text{ET}} (\times 10^9 \text{ s}^{-1})$ <sub>d</sub>
PbS core	837	978	2 2	3.5	58.1	3.35
PbS/C dS	826	967	3 4	5.0	73.1	0.934

<sup>a</sup> Determined by UV-Vis spectroscopy in toluene; <sup>b</sup> 10  $\mu\text{M}$  QD in 20 mM rubrene in toluene at RT, excited with a CW 785 nm laser at 26.4 W/cm<sup>2</sup>. <sup>c</sup>  $\Phi_{\text{TET}}$  and <sup>d</sup>  $k_{\text{ET}}$  determined from transient absorption measurements.

The sensitivity of the overall photon upconversion efficiency on the composition of the QD suggests that the TET between QD and **5-CT** is one of the key efficiency-limiting steps. In addition to this desired process, excitons in the QD can also decay by radiative recombination within the QD and charge (electron or hole) transfer to **5-CT**. We first examine the energetics of all possible exciton decay pathways in the QD//**5-CT** complex.

Shown in Fig. 5.1b is the reduction potential of PbS/CdS (-3.6 V vs vacuum) and oxidation potential of **5-CT** (-5.4 V vs vacuum) measured by cyclic voltammetry (in dichloromethane at -50 °C and RT, respectively, Chapter 8). From these values and the optical gaps (2.58 eV for **5-CT** and 1.48 eV for PbS/CdS, see Chapter 8), the reduction potential of **5-CT** (-2.9 V) and oxidation potential of PbS/CdS core-shell QDs (-5.1V) was estimated (Fig. 5.1b). Fig. 5.1c shows the energy levels of various states generated by either energy, electron or hole transfer from QDs. It is clear that starting from the band edge excitonic state in the QD, i.e. QD(T<sub>1</sub>)/**5-CT**(S<sub>0</sub>), electron (hole transfer) from the conduction band (valence band) edge of the QD to **5-CT** is uphill with the change of free energy of +0.7 (+0.3) eV. Only TET from QD(T<sub>1</sub>) to **5-CT**(S<sub>0</sub>), forming QD(S<sub>0</sub>)/CT(T<sub>1</sub>), is energetically downhill by 0.23 eV.

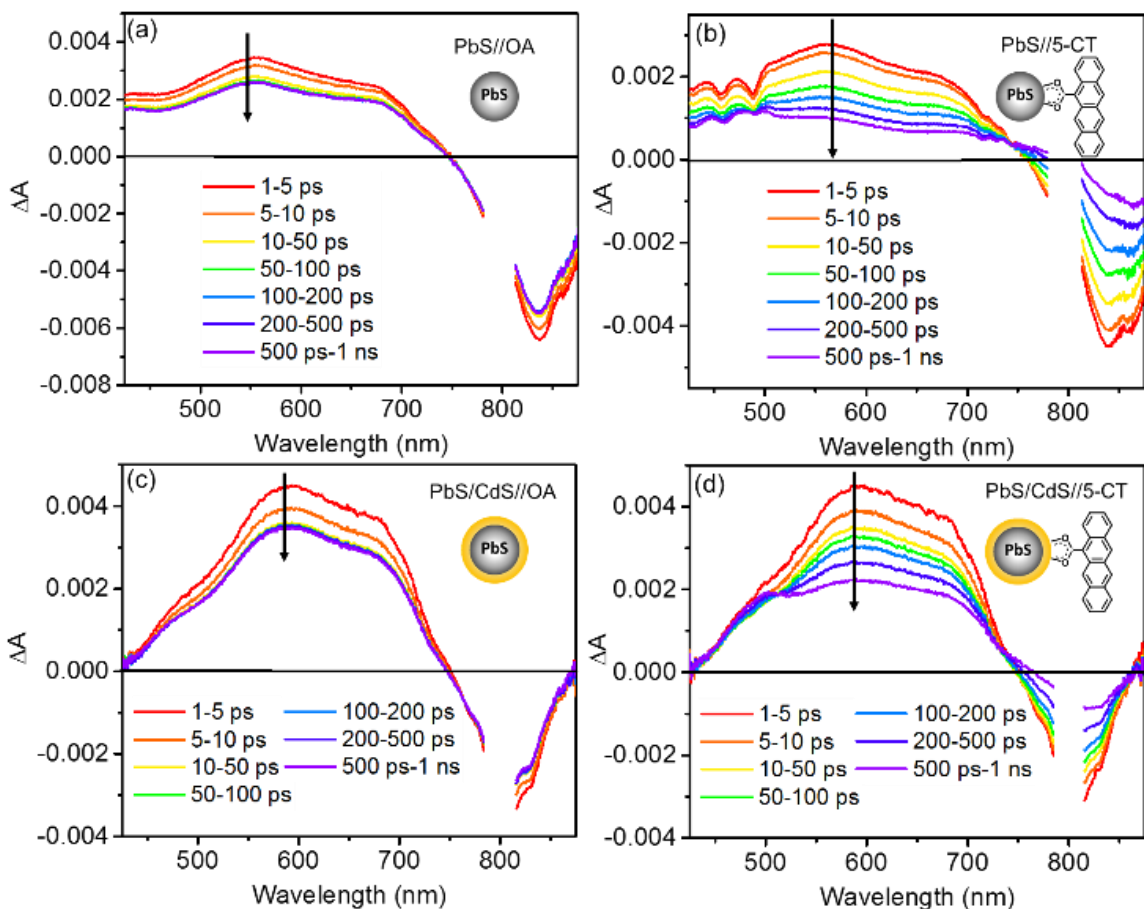


**Figure 5.2.** Comparison of TA spectra of QD//OA and QD//5-CT. TA spectra of (a) PbS QD capped with oleic acid, PbS//OA; (b) PbS QD capped with 5-carboxylic acid tetracene (5-CT), PbS//5-CT; (c) PbS/CdS core-shell QD capped with oleic acid, PbS/CdS//OA, and (d) PbS/CdS core-shell QD capped with 5-CT, PbS/CdS//5-CT. Samples are dissolved in toluene and excited at 800nm. Each curve in the figure is the average of the spectra within the indicated delay time window. Spectra from 785 to 815 nm are truncated due to the saturation of probe on the spectrometer.

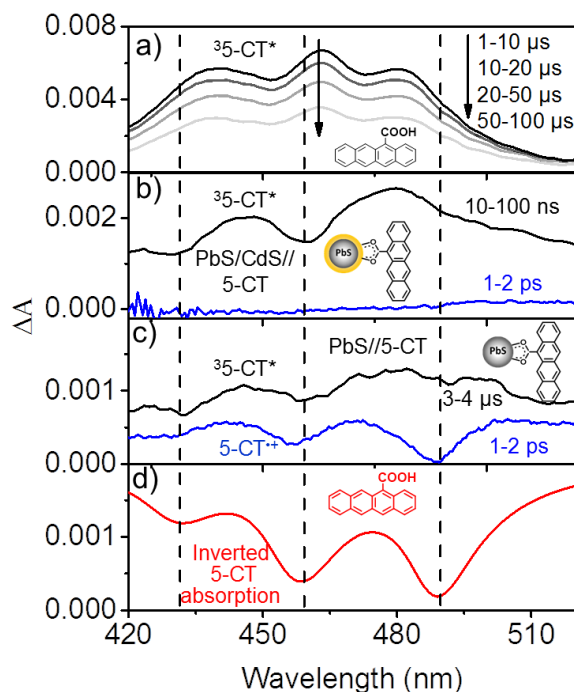


**Figure 5.3.** TA spectra and kinetics of triplet energy transfer. (a) TA spectra of **5-CT** in tetrahydrofuran at the indicated delay times; Double difference TA spectra of (b) bound **5-CT** on PbS/CdS QD at 1-2ps (blue) and 10-100 ns (black), (c) bound **5-CT** on PbS QD at 1-2 ps (blue) and 3-4  $\mu$ s (black); (d) The inverted steady state electronic absorption spectrum of bound **5-CT**. The QD//**5-CT** samples were excited at 800 nm while the free **5-CT** at 400 nm. The double difference TA spectra of bound **5-CT** are obtained by subtracting the contribution of the QD from the TA spectra shown in Fig. 5.2b and d (see Chapter 8 for details).

In order to explain the  $\sim 40\%$  enhancement in the photon upconversion QY in the presence of the CdS shell, TA measurements were performed to study the exciton decay pathways and kinetics of TET from QDs to **5-CT**. Here, four samples consisting of as-synthesized PbS core and PbS/CdS core/shell QD and the **5-CT** functionalized QDs that gave the highest photon upconversion QYs in toluene were studied. Fig. 5.2 shows the TA spectra of these four samples measured by selective excitation of the QD at 800 nm. In Fig. 5.2a and 5.2c, spectra of the oleic acid capped QDs (PbS//OA and PbS/CdS//OA) are shown. The broad positive feature from 400 to 750 nm is the excited state absorption (ESA)



of the QD, and the negative peak from 750 to 900 nm is the ground state bleach of the QD. Both features decay with the same kinetics (see below), reflecting the electron and hole dynamics within the QD.<sup>172</sup> Comparison of the spectra of PbS//**OA** (Fig. 5.2a) with PbS//**5-CT** (Fig. 5.2b) and PbS/CdS//**OA** (Fig. 5.2c) with PbS/CdS//**5-CT** (Fig. 5.2d) clearly shows that the presence of **5-CT** leads to faster decay of QD signals (both ESA and exciton bleach) indicative of quenching of excitons in QD by **5-CT**.

In the 420-500 nm spectral region, the TA spectra (i.e. difference spectra between sample with and without excitation) consist of overlapping features of **5-CT** (its singlet ground state bleach and triplet absorption) and the QD's ESA. To better observe the spectral evolution of the relatively weaker **5-CT** features, we constructed double difference TA spectra, in which the contributions of the QD have been subtracted. To remove the QD signals, we scaled the QD//**OA** spectra (containing only QD signals) to match those of the QD//**5-CT** at the same time delays at 750-900nm, where the **5-CT** contribution is negligible, and subtracted the TA signal of QD//**5-CT** by that of the scaled QD//**OA**. The double difference spectra PbS//**5-CT** (Fig. 5.3c and Chapter 8) and PbS/CdS//**5-CT** (Fig. 5.3b and Chapter 8) show clearly the evolution the **5-CT** signal. For both PbS//**5-CT** and PbS/CdS//**5-CT**, as shown in Fig. 5.3c and b, respectively, the TA spectra at long delay times (>10ns) resemble that of the triplet state of free **5-CT** in tetrahydrofuran solution (Fig. 5.3a). This clearly confirms the triplet sensitization process on these QDs. The spectra in Fig. 5.3a were independently obtained by intersystem crossing from the singlet excited state of free **5-CT** in solution, as shown in Chapter 8. The triplet spectra consist of positive triplet ( $T_1$  to  $T_n$ ) absorption band and negative bleach of ground state absorption ( $S_0$  to  $S_1$ ).

Both the ground state and triplet state absorption spectra of **5-CT** adsorbed on QDs are red-shifted from those in solution, likely caused by their different solvation environments.

The TA spectra of PbS//**5-CT** at early delay times (1-2ps) also show a bleach of the **5-CT** ground state (Fig. 5.2b, Fig. 5.3c) without the formation of the molecular triplet state. A comparison of the exciton bleach recovery kinetics for PbS//**OA** and PbS//**5-CT** (Fig. 5.4a) shows that the initial exciton bleach amplitude is smaller in the latter despite the excitation of the same number of QDs in both samples. Taken together, these spectral features suggest an ultrafast transfer of electrons or holes from QD to **5-CT** occurring prior to their relaxation to the band-edge ( $< 0.3\text{ps}$ ). We speculate that this process is likely due to hot hole transfer from PbS to **5-CT** on basis of the following evidence. The TA spectra of this intermediate species are dominated by the bleach of the **5-CT** ground state absorption with no obvious absorption features in the visible region (Fig. 5.2b, Fig. 5.3c). From the reported spectra of **5-CT** anion (-) and cation (+), only **5-CT** (+) is consistent with the observed TA spectra at early times.<sup>173-175</sup> Formation of reduced **5-CT** should exhibit an absorption peak at 360 and 400 nm, in addition to the ground state bleach.<sup>173</sup> Furthermore, as shown in Fig. 5.1c, although hole transfer from band edge exciton is energetically uphill by +0.3 V, hot hole transfer from the QD to **5-CT** to form the QD(-)//CT(+) charge separated (CS) state is more energetically favorable than electron transfer. As described in the Chapter 8, detailed analysis of the double difference TA spectra (Chapter 8) shows that bound **5-CT** spectral evolution can be well fit to a model that considers two independent pathways (Fig. 5.1c). Pathway one is the instantaneous hot hole transfer induced formation of the CS state, QD(-)//CT(+), which decays by charge

recombination to reform the ground state of the complex. Pathway two is TET from band edge excitons to form **5-CT** triplet state, which is discussed further below. As shown in Fig. 5.3b and Fig. 5.4b, for PbS/CdS//**5-CT**, both the ultrafast **5-CT** ground state bleach and QD exciton bleach recovery are not observed, suggesting that the CdS shell suppresses the hot hole transfer process.

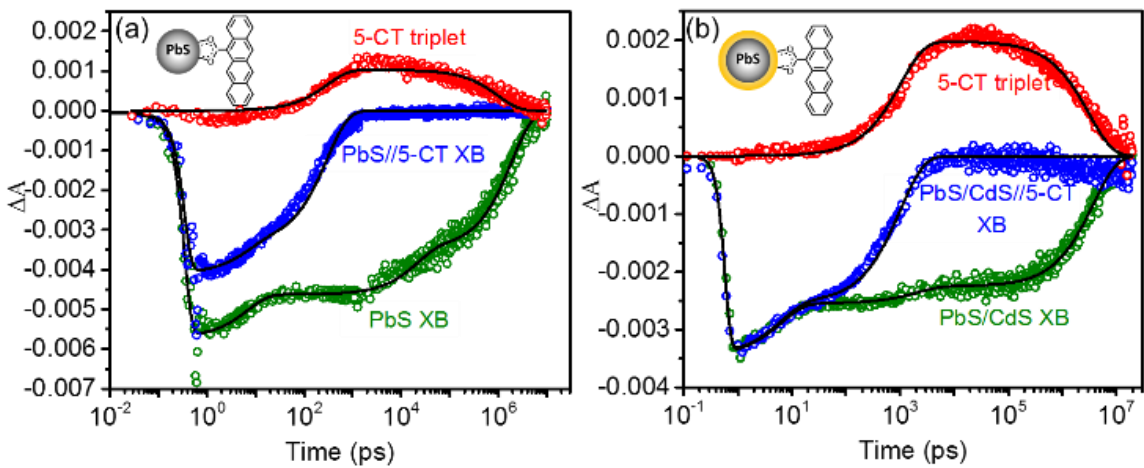


**Figure 5.4.** Kinetics of QD exciton bleach (XB, blue circles) at 820 nm and **5-CT** triplet (red circles) at 489 nm for (a) PbS//**5-CT** and (b) PbS/CdS//**5-CT**. Also shown for comparison are the XB kinetics of QDs without **5-CT** (green circles). Solid lines are a global fit to the kinetics according to the model in the main text.

The kinetics of the **5-CT** triplet state and QD exciton bleach are compared for PbS//**5-CT** (Fig. 5.4a) and PbS/CdS//**5-CT** (Fig.4b). The **5-CT** triplet formation kinetics can be well represented by the double difference TA signal at 489nm (see Chapter 8 for detailed discussion). These kinetics can be fit to a model that accounts for intrinsic decays in QDs, TET between QDs and **5-CT**, as well as ultrafast hole transfer between PbS QDs and **5-CT**. The fitting parameters are shown in Chapter 8. The presence of the CdS shell slows down the TET process from  $3.35 \pm 0.06 \text{ ns}^{-1}$  in PbS//**5-CT** to  $0.934 \pm 0.020 \text{ ns}^{-1}$  in PbS/CdS//**5-CT**, consistent with the shell being an insulating layer for TET.<sup>30,33</sup>

Interestingly, the decay of the **5-CT** triplet state also slows down from  $1.01 \pm 0.07 \mu\text{s}^{-1}$  in PbS//**5-CT** to  $0.318 \pm 0.017 \mu\text{s}^{-1}$  in PbS/CdS//**5-CT**. Both decay rates are faster than triplet decay of free **5-CT** in solution ( $0.009 \pm 0.0003 \mu\text{s}^{-1}$  in tetrahydrofuran), which suggests that the presence of QDs speeds up intersystem crossing (from  $T_1$  to  $S_0$ ) processes in **5-CT**. Interestingly, this triplet decay rate is larger for PbS than PbS/CdS, suggesting that CdS shell also reduces the yet-to-be identified coupling mechanism between QDs and **5-CT** that is responsible for the enhanced triplet decay.

From the fitting parameters one can calculate that the TET efficiency is 58.1% for PbS//**5-CT** and 73.1% for PbS-CdS//**5-CT**. A detailed comparison of exciton decay dynamics in PbS/CdS//**5-CT** and PbS//**5-CT** shows that the presence of the CdS shell suppresses the initial hot hole transfer pathway, enhancing the efficiency of TET. However, in PbS/CdS//**5-CT**, the TET efficiency is only 73.1%, suggesting additional loss pathways. As shown in Fig. 5.4 the kinetics of free QD exciton bleach can be well described with three exponential decays and the TET efficiency for these components can be calculated (Chapter 8). For the fastest decay component ( $\sim 24\%$  of total amplitude), the intrinsic decay within the PbS/CdS QD (with a rate constant of  $0.16 \text{ ps}^{-1}$ ) outcompetes the TET process in PbS/CdS//**5-CT**. For the intermediate component (9% of total amplitude), the intrinsic decay rate ( $0.44 \pm 0.07 \text{ ns}^{-1}$ ) within the QD is similar to the rate of TET, leading to 68% TET efficiency. The rate of TET is much faster than the slowest decay component (67% of the amplitude). These results suggest that defect-induced fast nonradiative e-h recombination within the QD is the major competing loss pathway for PbS/CdS//**5-CT**. Further

improvements that can eliminate these fast exciton pathways of PbS/CdS QDs would further enhance the TET efficiency.

These TA studies show the presence of the CdS shell leads to an enhancement factor of 1.26 (73.1%/58.1%) in TET efficiencies from the sensitizer to transmitter. This enhancement factor is smaller than that for the steady state upconversion QY of the full upconversion system (5%/3.5%=1.43). An additional improvement may come from prolonged **5-CT** triplet excited state lifetime in PbS/CdS/**5-CT** (compared to PbS/**5-CT**), which may enhance the TET from **5-CT** to the emitter rubrene.

### 5.3 Conclusion

In conclusion, this work demonstrates that compared to PbS core-only QDs, PbS/CdS core/shell QDs enhances the photon unconversion QY in a three-component triplet upconversion system consisting of QD, surface bound **5-CT** transmitter and rubrene annihilator/emitter. Detailed TA studies of QD/**5-CT** complexes clearly show the formation of the **5-CT** triplet state, confirming TET from QDs to **5-CT** for both QDs. In PbS//**5-CT**, there also exists a competitive ultrafast hot hole transfer processes that reduces the TET efficiency. In core/shell PbS/CdS//**5-CT** hybrid systems, although the CdS shell slows down the rate of TET from  $3.35 \pm 0.06 \text{ ns}^{-1}$  in PbS//**5-CT** to  $0.934 \pm 0.020 \text{ ns}^{-1}$  in PbS/CdS//**5-CT**, these TET rates are still faster than the intrinsic exciton lifetime of the QD. More importantly, the CdS shell suppresses the hot hole transfer pathway, leading to enhanced TET efficiency in PbS/CdS//**5-CT**. Furthermore, the decay of **5-CT** triplet excited state is slower on PbS/CdS compared to PbS, which likely further enhances the energy transfer efficiency from QD to rubrene in the photon upconversion system. This

work shows that core/shell structures can be used to tune the rates of competing energy and charge transfer processes, and to prolong the lifetime of triplets. It provides insight into the rational design of semiconductor QDs for triplet sensitization and photon upconversion applications.

## **Chapter 6     ZnS shells enhance triplet energy transfer from CdSe nanocrystals for photon upconversion**

### **6.1 Introduction**

Efforts to harness the interesting optical and electronic properties in nanocrystals (NCs) are usually hampered by uncontrolled charge transfer, electron-phonon or exciton-phonon coupling. These loss mechanisms are typically mitigated with thick or ‘giant’ shells that decrease non-radiative rates and minimize photoluminescence (PL) intermittency. This allows the tunable bandgaps and photostability of semiconductor NCs to be used in biological labeling, solid-state lightening and displays. Although ‘giant’ shells result in stable NC emitters, they serve as barriers impeding charge or energy transfer. For example, NCs used as the active material in photovoltaic devices eschew thick shells for thinner ones that allow simultaneous charge percolation and trap passivation to improve power conversion efficiency.

The role of the shell has not been clearly articulated for triplet exciton transfer, a process critical for singlet fission and photon upconversion. Since these multiexcitonic processes have the potential of exceeding the Shockley-Queisser limit with diffuse sunlight, it is important that the fundamental parameters controlling triplet transfer between molecules and nanocrystals be elucidated for the rational design of these hybrid platforms for energy conversion.

In this work, the effect of core-shell architecture on the efficacy of triplet energy transfer from CdSe NC light absorbers is investigated for photon upconversion. In cadmium selenide NCs, thermally accessible processes at room temperature involve hole

excitations and lattice vibrations, and when a shell is present, electron excitations. The presence of a shell may be a bane or a boon. At the core-shell interface, charge localization affects the rate of Auger recombination; electron and hole wavefunction overlap influences the efficiency of multiple exciton generation. Shell thickness and band offset affect the tunneling of charges or excitons from the core. Heterogeneity in material composition affects the nuclear fluctuations, which in turn modulate radiative rates and non-radiative processes like triplet energy transfer.

Building on previous work, we sought to investigate if epitaxial shell growth could ameliorate strain-based surface traps, and if photoluminescence quantum yield (PLQY) correlated with triplet energy transfer. Many workers have shown that ZnS or CdS shells on CdSe nanocrystals dramatically improve NC brightness, because these higher bandgap materials spatially confine the excitons to the core, thus minimizing the probability of encountering surface trap states. Thus, a whole range of CdS and ZnS shell thicknesses are examined here, with a focus on thin shells like those used for QD solar cells. Unlike the long-range energy transfer of singlet excitons through space, triplet excitons are transferred through bonds, so a thin shell is expected to enable better electronic coupling.

## **6.2 Results and discussion**

With the 2.9 nm diameter CdSe NCs used here, we find that only sub-monolayer ZnS shells enhance triplet energy transfer and photon upconversion, while CdS shells do the opposite. We study triplet energy transfer from CdSe/ZnS and CdSe/CdS core/shell NCs to anthracene molecules with linear photon upconversion, ultrafast transient absorption (TA) spectroscopy and time resolved lifetime measurements. The upconversion



quantum yield (QY) is enhanced 1.6 times by the growth of a ZnS shell from 5.7 to 9.3 %, consistent with TA spectra that show an increase in the efficiency of triplet energy transfer from 6.3% to 10.3%. All the core-shell NCs here have an order of magnitude larger radiative rate than the core, indicating successful surface passivation. TA spectra shows that the electron localized at the CdS shell is rapidly quenched within nanoseconds in the presence of the anthracene acceptor with negligible triplet transfer. We postulate that the major difference in the efficiencies of triplet transfer arise from stronger exciton-phonon coupling with the CdS shell that dissipates the photogenerated exciton in the CdSe core, similar to the linewidth broadening observed in the photoluminescence of single CdSe/CdS core/shell NCs, and the large linewidth in CdS nanoplatelets.

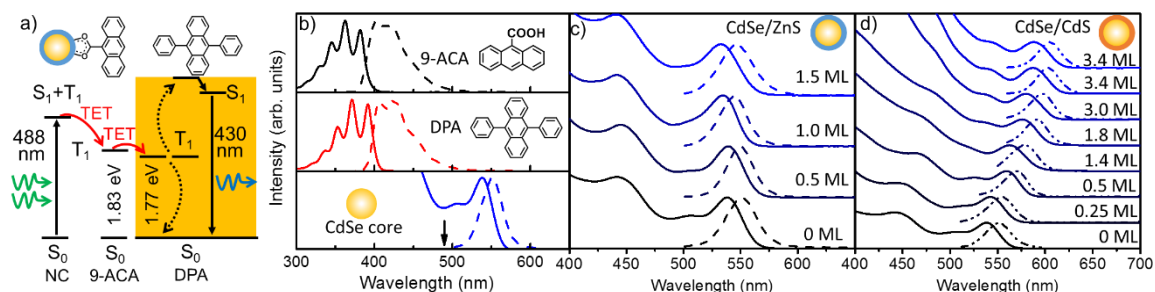


**Figure 6.1.** (a) Illustration of the triplet energy transfer (TET) in this hybrid photon upconversion system. Green and blue arrows denote photoexcitation of the nanocrystals (NCs) and emission from diphenylanthracene (DPA) respectively. Dotted black and red curved arrows denote the triplet-triplet annihilation and TET. The absorption (solid line) and emission (dashed line) spectra of (b) 9-ACA (top), DPA (middle), 2.9 nm diameter CdSe NCs (bottom); (c) CdSe/ZnS and (d) CdSe/CdS core-shell NCs with different shell thickness (ML = monolayer). The black arrow in the bottom panel of Fig. 6.1b indicates the excitation wavelength used (488 nm). Measurements are performed in hexane at room temperature.

The hybrid upconversion system investigated here is depicted in Fig. 6.1a. It is composed of CdSe NCs as sensitizer, 9-anthracenecarboxylic acid (9-ACA) as transmitter, and diphenylanthracene (DPA) as annihilator. During linear photon upconversion

experiments, the NCs are photoexcited by a 488 nm CW laser. Triplet energy transfer occurs firstly from the NCs to the triplet state of 9-ACA, which is directly bound on the NC surface, then secondly to free DPA in solution. Two DPA molecules in their triplet-excited state annihilate to form a singlet that emits the upconverted 430 nm photon. Fig. 6.1b shows the absorption and emission spectra of 9-ACA, DPA and the CdSe core NCs.

In order to epitaxially grow sub-monolayer thick CdS shells on CdSe cores, slow deposition at high temperatures was performed with the injection of octanethiol and cadmium oleate at 240 °C over 2 hours, following the methodology recently reported by Bawendi and Chen. Shell growth was only reproducible with CdSe cores larger than 2.9 nm in diameter, presumably because strain at the core-shell interface is not prohibitive beyond this size. This core size is still small enough to maintain a driving force of 0.47 eV for triplet energy transfer to the anthracene acceptor. However, since the lattice mismatch between ZnS and CdSe is 12% (compared to 4.5 % between CdS and CdSe), no epitaxial growth can occur. Therefore, the ZnS shell is grown on the CdSe core using the more reactive precursors of diethylzinc and hexamethyldisilathiane, injected at 160 °C over 10 min. In order to make high quality core-shell NCs, these CdSe/ ZnS core/shell NCs were annealed for 3 hours at 90 °C. ZnS and CdS shells blue and red shift the absorption maxima of the CdSe NCs respectively, as seen in Fig. 6.1c and 1d. The 2-7 nm blue shift as the ZnS shell increases from 0.5 ML to 1.5 ML indicates contraction of the CdSe core and is interpreted as formation of a Zn-Cd alloy structure at the surface and a Type I electronic structure. On the other hand, growth of a CdS shell leads to exciton delocalization with a red shift as large as 49 nm to 589 nm (3.4 monolayers), suggesting a pseudo Type II

electronic structure. Delocalization of the electron into the shell arises from the small band offsets between both materials (300 meV in the bulk).

**Table 6.1.** The shell thickness  $n$  in monolayer (ML), absorption and emission maxima,  $\lambda_{abs}$  and  $\lambda_{ems}$ ; average number of bound ligands per NC,  $N$ ; mole ratio of Se: Cd: Zn from ICP-AES; the radiative rate constant,  $k_r$ ; the nonradiative rate constant,  $k_{nr}$ ; the photoluminescence quantum yield,  $\Phi_{PL}$ ; and the photon upconversion quantum yield,  $\Phi_{UC}$  for each nanocrystal.

NC	$n$ / ML	$\lambda_{abs}^a$ / nm	$\lambda_{ems}^a$ / nm	$N^b$	mole ratio Se: Cd: Zn	$k_r$ / $\mu\text{s}^{-1}$	$k_{nr}$ / $\mu\text{s}^{-1}$	$\Phi_{PL}^a$ / %	$\Phi_{UC}^c$ / %
CdSe	0	540	552	2.63	1:1.32:0	0.43	16.0	2.72	5.7
CdSe/ZnS	0.5	538	549	1.84	1:1.34:0.492	6.21	6.01	50.8	9.3
	1	535	544	5.14	1:1.36:0.0447	4.84	5.22	48.1	8.1
	1.5	533	545	9.31	1:1.36:0.597	8.15	6.40	56.0	5.6
CdSe/CdS	0.25	543	555	4.56	1:1.42:0	2.54	12.6	16.8	0.59
	0.5	559	570	2.61	1:1.26:0	1.53	16.2	8.63	0.31
	1.4	563	578	3.05	1:3.33:0	2.06	24.0	7.91	2.3
	1.8	576	591	8.59	1:4.10:0	8.11	21.5	27.4	2.5
	3.0	580	597	9.78	1:6.93:0	7.27	20.9	25.8	1.9
	3.4	588	603	13.4	1:8.56:0	15.3	11.5	57.1	1.0
	3.4	589	604	12.3	1:8.54:0	9.03	13.3	40.4	0.91

<sup>a</sup>Hexanes, RT;  $\Phi_{PL}$  with a R6G standard; <sup>b</sup>Given by UV-vis spectroscopy; <sup>c</sup>5  $\mu\text{M}$  NC in 2.15 mM DPA in hexane at RT, excited with a CW 488 nm laser at 19.8 W/cm<sup>2</sup>.

The shell thickness was determined by the ratios of Se, Cd, and Zn obtained from inductively coupled plasma atomic emission spectroscopy (Table 6.1), the size of CdSe core (determined by the first exciton absorption peak), and the bulk density of CdSe, CdS and ZnS. The shell thickness is represented in monolayers (MLs) of shell materials, where

1 ML is 3.4 Å and 3.1 Å for wurtzite CdS and ZnS respectively. For the CdSe core, all CdSe/ZnS core/shell NCs and the 0.25 and 0.5 ML CdSe/CdS core-shell NCs, the molar ratios of Cd/Se = 1.3-1.4, indicating that the composition of the NC doesn't change significantly when shell is very thin. The estimated shell thickness and the first exciton absorption peaks of CdSe/CdS core-shell NCs in this work match the calibration curve reported by Mulvaney and coworkers well. (JACS, 2009, 131,14299)

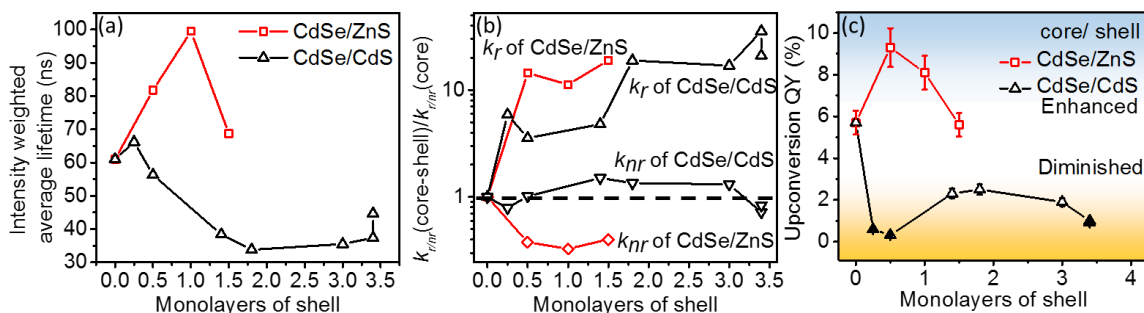


**Figure 6.2.** The (a) Intensity weighted average lifetimes; (b) Radiative ( $k_r$ ) and nonradiative ( $k_{nr}$ ) rate constants normalized relative to the CdSe core; (c) Photon upconversion QYs of the NC sensitizers with surface bound 9-ACA and 2.15 mM DPA with respect to shell thickness. CdSe/ZnS and CdSe/CdS core/shell nanocrystals (NCs) are denoted by the red square and black triangle respectively. Data in (a) and (b) are obtained from lifetime measurements (see Chapter 8) with a 406 nm pulsed laser and (c) with a 488 nm CW laser at 19.8 W/cm<sup>2</sup>. All samples are dissolved in hexane and measured at room temperature.

The core/shell NCs here have higher photoluminescence QYs,  $\Phi_{PL}$ , and radiative rate constants,  $k_r$ , compared to the core, implying surface traps detrimental to emission are removed with shell growth. For example,  $\Phi_{PL}$  is 2.72%, 56.0% and 57.1% and  $k_r$  is 0.43  $\mu\text{s}^{-1}$ , 8.15  $\mu\text{s}^{-1}$  and 15.3  $\mu\text{s}^{-1}$  for the CdSe core, the CdSe/(1.5ML)ZnS and CdSe/(3.4ML)CdS core/shell NCs respectively (see Table 6.1). Radiative and non-radiative time constants were obtained by fitting PL decays with a triexponential and calculating the intensity weighted average lifetimes (Fig. 6.2a and Chapter 8). The higher

radiative rates are consistent with near unity PLQY CdSe nanocrystals that show decreasing radiative lifetimes with increasing shell thickness, a trend expected for single-component CdSe nanocrystals, but unexpected from a pure Type II structure (JPCC 2015, 119, 2231). We note that CdS nanorods with CdSe seeds transition from pseudo-Type II to Type I when the CdSe core diameter exceeds 2.75 nm.

The photon upconversion quantum yield,  $\Phi_{UC}$ , of the NC photosensitizers is enhanced by the ZnS shell, reduced by the CdS shell, and is inversely proportional to the non-radiative rate constants,  $k_{nr}$ . As seen in Table 6.1, the CdSe/ZnS core/shell NCs have an order of magnitude lower  $k_{nr}$  compared to the other NCs. The ZnS shell enhances  $\Phi_{UC}$  from 5.7% (CdSe core) to 8.1% and 9.3% for the CdSe/(1ML)ZnS and CdSe/(0.5ML)ZnS core/shell NCs respectively. However, NCs with CdS shells ranging from 0.25 to 3.4 ML have lower  $\Phi_{UC}$ , with the highest  $\Phi_{UC}$  less than half that compared to the CdSe core.  $\Phi_{UC}$  for each NC is optimized by varying  $N$ , the average number of surface bound 9-ACA ligands per NC (see Chapter 8). The highest  $\Phi_{UC}$  with the corresponding  $N$  are presented in Table 6.1 and Fig. 6.2c.  $\Phi_{UC}$  reaches a maximum at 0.5 ML of ZnS and 1.8 ML of CdS and then decreases as the shell thickness increases because the tunneling barrier slows down the triplet energy transfer from the CdSe core to 9-ACA. A similar trend is observed for triplet transfer from PbS/CdS core-shell NCs to rubrene. In our hands, it was challenging to grow ZnS shells less than 0.5 ML on these 2.9 nm diameter cores, thus the highest reported  $\Phi_{UC}$  is for the CdSe/(0.5 ML)ZnS NCs at 9.3%. Note that in this work  $\Phi_{UC}$  is defined as:

$$\Phi_{UC} = 2 \times \Phi_{ref} \times \frac{(\text{photons absorbed by reference})}{(\text{photons absorbed by UC sample})} \times \frac{PL \text{ signal}(UC \text{ sample})}{PL \text{ signal}(reference)} \quad (6.1)$$

where  $\Phi_{ref}$  is the fluorescence QY of the reference rhodamine 6G. The factor of 2 in the equation means  $\Phi_{UC} = 100\%$  when 50 upconverted photons are produced for every 100 photons absorbed.

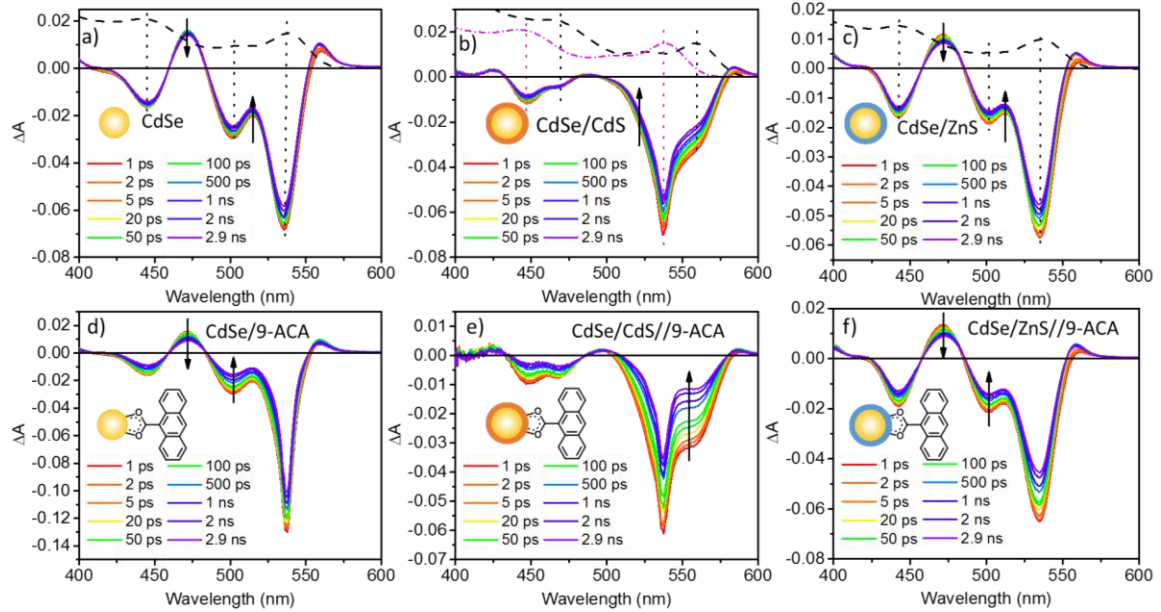


**Figure 6.3.** Femtosecond transient absorption (TA) spectra of (a) CdSe; (b) CdSe/(0.5ML)CdS; and (c) CdSe/(0.5ML)ZnS nanocrystals (NCs); (d)-(f) TA spectra of the same NCs with surface bound 9-anthracenecarboxylic acid. Samples are dissolved in hexane and excited with a 540 nm pulsed laser. The black dashed curves in (a) and (c) are the linear absorption spectra of CdSe core and 0.5 ML CdSe/ZnS core-shell NCs, and the magenta and black dashed curves in (b) are that of CdSe core and 0.5 ML CdSe/CdS core-shell NCs respectively.

Transient absorption (TA) measurements were performed to probe the difference in the electronic transitions between the CdS and ZnS shells. Triplet energy transfer was studied for the CdSe core ( $\Phi_{UC} = 5.7\%$ ), CdSe/(0.5ML)ZnS ( $\Phi_{UC} = 9.3\%$ ), and CdSe/(0.5ML)CdS ( $\Phi_{UC} = 0.31\%$ ) NCs capped with 9-ACA dissolved in hexanes. We chose CdSe/(0.5ML)ZnS core-shell NCs because it has the highest upconversion QY and its Cd counterpart with the same shell thickness for comparison. Samples were excited with a 540 nm femtosecond laser at low power (220 nJ) to avoid the creation of more than one

exciton per NC (Chapter 8). Fig. 6.3 shows the TA difference spectra of the CdSe core, CdSe/(0.5ML)ZnS, and CdSe/(0.5ML)CdS core-shell NCs with and without surface bound 9-ACA. The positive features are assigned to the excited state absorption (ESA), and the negative features to the ground state bleach (GSB) of the NCs. The latter corresponds to maxima in the linear absorption spectra (dashed lines in Fig. 6.3a, b c).

**Table 6.2.** The rate constant of triplet energy transfer (TET),  $k_{TET}$ ; TET efficiency  $\Phi_{TET}$ ; and the relative decrease of initial exciton bleach of CdSe NCs monitored at 520 nm due to An-X,  $\Delta_{XB}$ .

NC	$k_{TET}$ (s <sup>-1</sup> )	$\Phi_{TET}$	$\Delta_{XB}$
CdSe	3.08E+09	6.28	4.85
0.5 ML	1.89E+10	10.3	7.71
0.5 ML	-	-	24.5

Ultrafast TA spectra shows that the CdSe/CdS core/shell NCs have virtually no excited state absorption, indicating sub-picosecond depletion of the exciton (Fig. 6.3b and e). This is clearly seen in the 3ps window in Fig. 6.4a, where the kinetics of the GSB at 523 nm for the three sets of NCs with and without the surface bound 9-ACA are shown. In principle, the population of photoexcited CdSe NCs should be proportional to the concentration of NCs. Therefore, the initial amplitude at time zero for the GSB at 523 nm should be the same after normalizing by the linear absorption at 540 nm (the excitation wavelength). However, it is considerably smaller with the CdS shell. If we define the decrease of the initial amplitude,  $\Delta_{XB}$  as:

$$\Delta_{XB} = \frac{\Delta A_0(NC) - \Delta A_0(NC/9-ACA)}{\Delta A_0(NC)} \quad (6.2)$$

where  $\Delta A_0$  is the absorption at 523 nm at time zero for different samples, then  $\Delta_{XB} \sim 5-8\%$  for CdSe and CdSe/ZnS core/shell NCs, but is significantly higher at  $\Delta_{XB} = 25\%$  for the CdSe/CdS core/shell NCs. As can be seen in Table 6.2,  $\Delta_{XB}$  negatively correlates with  $\Phi_{UC}$ . Compared to CdSe and CdSe/ZnS NCs, CdSe/CdS NCs have a dramatically different TA spectrum with the absence of ESAs at 471 nm and GSBs at 501 nm, and the presence of a new GSB bathochromically shifted from the core at 560 nm. Electronic transitions corresponding to excitons confined to the CdSe core and delocalized to the CdS shell are observed (Fig. 6.3b). The CdSe core has GSB at 446 nm and 540 nm (linear absorption in magenta) while the CdS shell has GSB at 470 nm and 560 nm (linear absorption in black). In the presence of the 9-ACA transmitter ligand, the GSB at 560 nm corresponding to excitons delocalized in the shell is 68% quenched within the 3 ns window, without sensitization of the molecular triplet state. No rise channel is observed at 433 nm, the isosbestic point for these NCs that coincides with the  $T_1-T_n$  transition of bound 9-ACA. This is consistent with the low  $\Phi_{UC}$  of 0.31%. The presence of 9-ACA quenches the exciton on the CdS shell more efficiently than that on the core, probably by coupling to molecular vibrations.



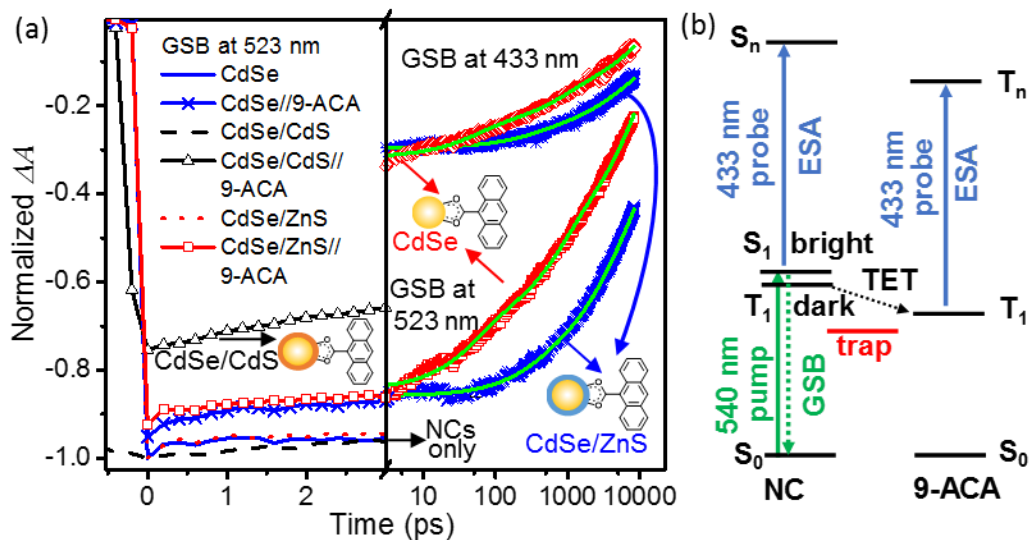


**Figure 6.4.** (a) The initial ground state bleach at 523 nm for CdSe, CdSe/(0.5ML)ZnS, and CdSe/(0.5ML)CdS with and without surface bound 9-ACA. The curves for NCs only are normalized with the initial minimum O.D. to be -1, and curves for NCs capped with 9-ACA are normalized based on the NC concentration, i.e. the O.D. at 540 nm in the linear absorption spectra. Green curves are the global fits to the recovery of the GSB at 433 nm (averaged over 430-435 nm) and 523 nm (averaged over 520-525 nm) for CdSe//9-ACA and 0.5 ML CdSe/ZnS//9-ACA. Measurements were performed in hexane at room temperature, with the excitation of 540 nm pulsed laser. (b) The energy diagram describing the physical processes during TA measurements.

TA measurements confirm that the ZnS shell removes the surface-based trap states. The TA difference spectrum of CdSe/ZnS core/shell NCs (Fig. 6.3c and 3f) has similar ESA and GSB features as the core CdSe NCs (Fig. 6.3a and 3d), with the exception of the most red-shifted positive absorption peak. This feature is typically associated with trap states, and is decreased with the ZnS shell (Fig. 6.4b). For both the CdSe core and the CdSe/ZnS core/shell NCs, the presence of the 9-ACA transmitter ligand results in a faster recovery of the GSB and decay of the ESA that can be correlated with triplet energy transfer. For both,  $\Phi_{UC}$  from linear upconversion measurements correlates to the rate constant ( $k_{TET}$ ) and efficiency ( $\Phi_{TET}$ ) of triplet energy transfer obtained from TA

spectroscopy. Since the  $T_1$ - $T_n$  transition of bound 9-ACA is centered at 433 nm, we monitor the kinetics at 433 nm to extract the  $k_{TET}$  and  $\Phi_{TET}$  (see Chapter 8 for details). Global fitting of the kinetics at 433 nm and GSB at 523 nm for CdSe//9-ACA and CdSe/ZnS//9-ACA (Fig. 6.4b) provides  $k_{TET}$ ,  $k_{TET}$  per 9-ACA ligand, and  $\Phi_{TET}$  (Table 6.2). The ZnS shell enhances  $k_{TET}$  from  $3.08 \times 10^9 \text{ s}^{-1}$  to  $1.89 \times 10^{10} \text{ s}^{-1}$  and  $\Phi_{TET}$  1.6 times from 6.28% to 10.3%, which is consistent with the 1.6 times increase of  $\Phi_{UC}$  from 5.7% to 9.3%. This makes sense because  $\Phi_{UC} = \Phi_{TET} \times \Phi_{TTA(DPA)} \times \Phi_{F(DPA)}$  where  $\Phi_{TTA(DPA)}$  and  $\Phi_{F(DPA)}$  are the efficiency of triplet-triplet annihilation and fluorescence quantum yield of DPA respectively. As  $\Phi_{TTA(DPA)}$  and  $\Phi_{F(DPA)}$  are constants,  $\Phi_{UC}$  is proportional to  $\Phi_{TET}$ .

This data shows that the CdS shell is detrimental for photon upconversion because its exciton is rapidly depleted at sub-picosecond timescales, most likely through rapid charge transfer, and then again at nanosecond timescales when bound with the 9-ACA anthracene transmitter, without triplet energy transfer. The latter may be explained by exciton-vibrational coupling to the molecule or exciton-phonon coupling to nuclear fluctuations. Cui and Bawendi *et al.* have reported that there is stronger exciton-longitudinal optical phonon coupling in CdSe/CdS compared with CdSe/ZnS core-shell NCs. This is because the exciton in CdSe/CdS core-shell NCs delocalizes to the shell, as observed in the linear absorption and TA difference spectrum here. This decreases electron-hole wavefunction overlap compared to the CdSe core and CdSe/ZnS core-shell NCs, polarizes the NC and couples the optical phonon with the exciton. In addition, delocalization of excitons in CdSe/CdS NCs to the shell increases the chance of sampling the surface-based defects, inducing more polarization and stronger exciton-phonon

coupling at the expense of triplet energy transfer. At the nanoscale, coupling between electronic excited states and lattice fluctuations can change the emission maxima by as much as 90%, as shown by temperature dependent measurements on CdSe/CdS core/shell NCs.

Though all the core/shell NCs have increased radiative rates, only sub-monolayer ZnS shells improve photon upconversion QYs. We propose that CdSe/ZnS core/shell NCs with thicker shells that have more surface ligands (i.e.  $N > 9$ , the maximum number here) may show increased photon upconversion QYs in the presence of more triplet acceptors. This hypothesis is based on the observation that the net rate of hole transfer from CdSe/CdS core-shell NCs to surface bound ferrocene for 7ML CdS shells is higher than for the 3 and 5 MLs because of the higher surface loading of ferrocene acceptors. For photon upconversion, bulky transmitters may be necessary to avoid triplet-triplet annihilation between neighboring ligands.

### 6.3 Conclusion

Triplet energy transfer from the CdSe exciton competes with both radiative and non-radiative loss mechanisms. Shell growth improves triplet energy transfer from CdSe donor to anthracene acceptors for three reasons. Firstly, the ZnS shell minimizes the contribution of the fastest decay component comprising the NC lifetime, allowing triplet transfer to compete. Secondly, it decreases the non-radiative rate,  $k_{nr}$ , by chemically passivating the surface. Lastly, it minimizes exciton-phonon coupling by promoting wavefunction overlap between electron and hole. The best performing CdSe/ZnS core-shell NCs with 0.5 ML shell thickness enhance the photon upconversion QY 1.6 times

from 5.7 % to 9.3%. In contrast, the poor photon upconversion QYs in the presence of the CdS shell can be explained by relatively strong exciton-phonon coupling, and decreased exciton lifetimes that deplete the density of excited states responsible for triplet sensitization. This work provides a guide for designing core-shell NCs that have enhanced triplet energy transfer for purposes of imaging and solar energy conversion.

## **Chapter 7     The Goldilocks effect for triplet transfer from CdSe nanocrystals for photon upconversion: anchoring groups.**

### **7.1 Introduction**

The prospect of combining energy contained in photons from the sun directly to exceed the Shockley-Queisser limit<sup>11,25,26,33,128,176-181</sup> is most feasible using a combination of nanocrystal light absorbers and molecular emitters. This hybrid platform requires that triplet transfer be efficient for useful energy conversion. Since triplet energy transfer (TET) occurs through bonds, the atomic and molecular details at the interface are expected to substantially impact the yield and kinetics of exciton transport. Indeed, Dexter-type exchange has been used to explain the exponential dependence on transfer efficiency for both aliphatic and aromatic bridges.<sup>23,37,182</sup> This is in contrast to singlet exciton transfer between NCs and molecules<sup>183,184</sup>, where the distance or nature of the linkage between donor and acceptor is not as critical, as long as both are within the Förster radius.

Here, we present the first systematic study on the role of the functional group (X) tethering the molecular triplet transmitter to the NC (Fig. 7.1a and b). We have previously shown that the transmitter ligand can enhance the photon upconversion QYs in this hybrid system up to three orders of magnitude, by introducing an energy cascade and facilitating orbital overlap between the NC donor and molecular acceptor.<sup>25</sup> Using 9 different functional groups that bind more strongly than the current workhorse, the carboxylic acid functionalized anthracene (X= COOH, An-COOH, Fig. 7.1e) ( $K_a = 1.3 \times 10^6 \text{ M}^{-1}$ )<sup>185-187</sup>, we show that sterics, binding affinity and electronic structure of the bridge drastically affect TET. Here, triplet exciton transfer from CdSe NCs to bound anthracene ligands was

measured independently with photon upconversion using a CW laser and ultrafast transient absorption (TA) spectroscopy. The photon upconversion QYs,  $\Phi_{UC}$ , vary from 12-13.5% for X = COOH, PO<sub>3</sub>H<sub>2</sub> and imidazole, to near zero when X contains sulphur. TA measurements show TET efficiencies ( $\Phi_{TET}$ ) consistent with the upconversion QYs, with  $\Phi_{TET}$  as high as 12.3% for An-PO<sub>3</sub>H<sub>2</sub>. Rate constants for TET,  $k_{TET}$ , vary from 10<sup>9</sup>–10<sup>10</sup> s<sup>-1</sup>. TA spectroscopy also shows the anchoring group quenches the CdSe NC exciton on sub-ps timescales, depleting the photogenerated exciton. This quenching,  $\Delta_{XB}$ , is negatively correlated with the upconversion QY, and is as high as 24% for the dithioic acid and dithiocarbamate functionalized anthracene ligands, the worst performing anchoring groups.

## 7.2 Results

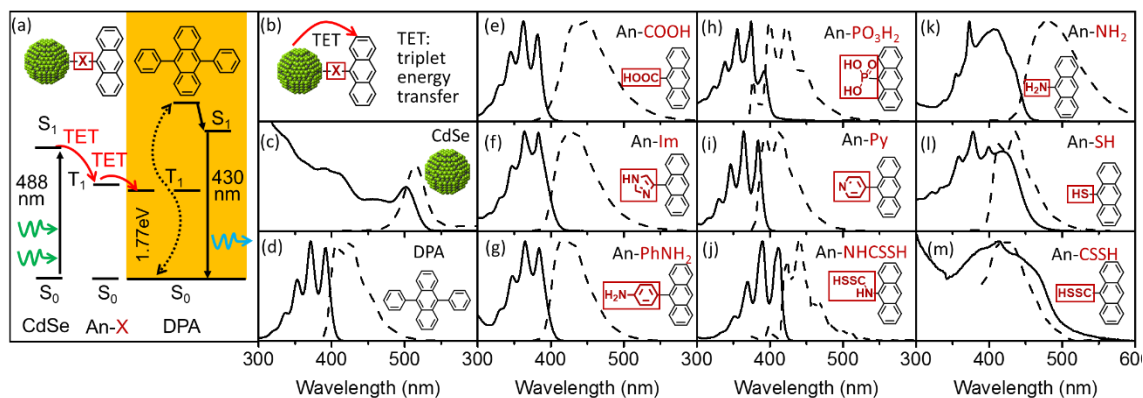


**Figure 7.1.** (a) Schematic of the energy transfer in this hybrid photon upconversion platform. Upon excitation with a 488 nm cw laser, triplet energy transfer (TET) occurs from CdSe nanocrystals (NCs) to the bound anthracene transmitter, and subsequently to 9,10-diphenylanthracene (DPA, yellow box). Two DPA triplets fuse to form a singlet, followed by emission at 430 nm. (b) Illustration of TET from CdSe NCs to bound anthracene ligands through anchoring groups, X. The absorption (solid line) and emission (dashed line) spectra of (c) 2.4 nm diameter CdSe NCs, (d) DPA, and (e)-(m) transmitter ligands with different anchoring groups measured in hexane at room temperature.

As shown in Fig. 7.1a, TET occurs in this hybrid upconversion system composed of CdSe NCs sensitizers, anthracene triplet transmitters (An-X) and 9,10-diphenylanthracene (DPA) annihilators.<sup>45</sup> Here, the anthracene transmitter is bound to the NC with functional group X in the 9- position of the ring. During photon upconversion experiments, only CdSe NCs are excited by the 488 nm CW laser, except for An-CSSH that shows a broad absorption band extending to 600 nm. Energy is transferred from the NC to the bound anthracene, An-X, and then to the DPA emitter in solution. Two DPA triplets then annihilate to form a singlet that radiatively decays, emitting the upconverted light at 430 nm.

The absorption and emission spectra of the CdSe NC donors, DPA, and transmitter ligands in hexanes are shown in Fig. 7.1c, 7.1d, and 7.1e-m respectively with the corresponding peak maxima in Table 7.1. As shown in 7.1b, anthracene functionalized with carboxylic acid (An-COOH),<sup>188,189</sup> phosphonic acid (An-PO<sub>3</sub>H<sub>2</sub>), imidazole (An-Im), pyridine (An-Py), *p*-aniline (An-PhNH<sub>2</sub>), amine (An-NH<sub>2</sub>), thiol (An-SH), dithiocarbamate (An-NHCSSH) and dithioic acid (An-CSSH) are investigated in this study. An-Im and An-CSSH are new molecules. All the transmitter ligands show vibrational fine structure in their absorption spectrum except when functionalized with the amino, thiol and dithioic acid groups (Fig. 7.1k-m). For An-NH<sub>2</sub>, this featureless absorption profile is assigned to intramolecular charge transfer states, as observed experimentally in its 2-aminoanthracene isomer.<sup>190</sup> Time-Dependent Density Functional Theory (TDDFT) calculations show that the bright state of An-NH<sub>2</sub> couples strongly with the amine, reducing the energy of the bright state and introducing charge-transfer character.<sup>190-194</sup> Although An-SH and An-

CSSH show similar broadening of their absorption spectra, TDDFT calculations do not show a similar coupling. Instead, TDDFT calculations find that the dithiolates An-CSSH and An-NHCSSH have very large  $S_1/T_3$  spin-orbit coupling constants (148  $\text{cm}^{-1}$  and 170  $\text{cm}^{-1}$  respectively) that promote intersystem crossing and contribute to their poor fluorescence quantum yields.<sup>195</sup> TDDFT has been used to locate conical intersections (CI) between the  $S_0$  and  $S_1$  surfaces, pathways for rapid internal conversion. These calculations show low-energy CIs for An-NH<sub>2</sub> and An-NHCSSH, partially explaining their anomalously low  $\Phi_F$ . Details about the synthesis of the NCs and transmitters, sample preparation, and TDDFT calculations are included in the Chapter 8.<sup>196-198</sup>

In terms of photon upconversion, the best transmitter ligands were the -COOH, -PO<sub>3</sub>H<sub>2</sub> and imidazole functionalized anthracene (Table 7.1), with  $\Phi_{UC} \sim 12.5\text{--}13.5\%$ . This was followed by the pyridine and then aniline functionalized anthracene, An-Py and An-PhNH<sub>2</sub>, with  $\Phi_{UC}$  of 6.7% and 3.6% respectively. When X contained S (thiol, dithioic acid and dithiocarbamate), or X = NH<sub>2</sub>,  $\Phi_{UC}$  is very low. The photon upconversion QYs are summarized in Table 7.1 and Fig. 7.3a, where  $N$  is the average number of bound anthracene transmitters per NC that corresponds to the conditions that gave the highest  $\Phi_{UC}$  (see Chapter 8).  $N$  is as high as 14 for X= Im and Py, but is low when X contains sulfur. It is well established that sulfur-containing ligands quench CdSe NC PL,<sup>63,76,77,199</sup> hence the highest upconversion QYs for these ligands were obtained at low  $N$  because TET is relatively slow compared to this fast quenching. As shown in Fig. 7.2a, there is no relationship between  $\Phi_{UC}$  and the energy levels of the highest occupied MO (HOMO) of



the anthracene transmitters given by cyclic voltammetry (Chapter 8) or their first excited triplet state,  $T_1$ , that ranges from 1.79-1.83 eV (Table 7.1 and Chapter 8).

**Table 7.1.** The absorption and emission maxima,  $\lambda_{\text{abs}}$  and  $\lambda_{\text{ems}}$ ; the energy corresponding to the  $T_1$ ,  $E_{T_1}$ ; the HOMO and LUMO energy levels,  $E_{\text{HOMO}}$  and  $E_{\text{LUMO}}$ ; the optical gap,  $E_{\text{gap}}$ ; the fluorescence QY,  $\Phi_{\text{F}}$ ; average number of bound ligands per NC,  $N$ ; and the photon upconversion QY,  $\Phi_{\text{UC}}$  for each anthracene transmitter ligand with functional group X.

Anth	$\lambda_{\text{abs}}^{\text{a}}$	$\lambda_{\text{ems}}^{\text{a}}$	$E_{T_1}^{\text{b}}$	$E_{\text{HOM}}$	$E_{\text{gap}}^{\text{a}}$	$E_{\text{LUM}}$	$\Phi_{\text{F}}^{\text{a}}$	$N^{\text{d}}$	$\Phi_{\text{UC}}^{\text{e}}$
CdSe	502	515	N/A	-5.60	2.48	-3.12	23.0	N/A	N/A
An-	362	446	1.83	-5.80	3.25	-2.55	34.3	2.80	13.5
An-	374	399	1.80	-5.71	3.16	-2.55	19.0	7.45	13.3
An-	364	430	1.79	-5.41	3.24	-2.17	12.2	13.8	12.5
An-	364	414	-	-5.15	3.24	-1.91	22.1	13.7	6.67
An-	365	416	1.79	-5.27	3.25	-2.02	16.3	3.34	3.56
An-	373	484	-	-4.80	3.02	-1.78	10.7	0.47	0.789
An-	378	435	-	-5.77	2.95	-2.82	2.01	-	0.146
An-	390	439	1.78	-5.66	3.02	-2.64	0.116	-	0.059
An-	413	428	1.81	-5.91	2.99	-2.92	0.260	-	0.00

<sup>a</sup>Hexanes, RT;  $\Phi_{\text{F}}$  with a DPA standard; <sup>b</sup>2-methyltetrahydrofuran, 77K. Dashed line indicates that phosphorescence was not detected; <sup>c</sup>Determined by cyclic voltammetry in 0.1 M tetra-*n*-butylammonium hexafluorophosphate in dichloromethane at RT with a ferrocene standard. The CdSe NC HOMO level is from Ref. 23<sup>55</sup>; <sup>d</sup>Given by UV-vis spectroscopy. Dashed line indicates less than one ligand bound per NC for sample optimized for photon upconversion; <sup>e</sup>35  $\mu\text{M}$  CdSe NC in 2.15 mM DPA in hexane at RT, excited with a CW 488 nm laser at 19.8 W/cm<sup>2</sup>.

Transient absorption measurements were performed to quantify the rates and efficiencies of TET,  $k_{\text{TET}}$  and  $\Phi_{\text{TET}}$ , on CdSe NCs functionalized with anthracene transmitters at ligand loadings that gave the highest  $\Phi_{\text{UC}}$  (as listed in Table 7.1). The original CdSe NCs capped with native octadecylphosphonic acid ligands (CdSe/ODPA) were also investigated. All samples were excited by a 505 nm pulsed laser at low power

(220 nJ) to avoid generating more than one exciton per particle (Chapter 8). Fig. 7.2b and 2d shows the TA difference spectra of CdSe/ODPA and CdSe/An-PO<sub>3</sub>H<sub>2</sub> where the broad positive and negative features are the excited state absorption (ESA) and ground state bleach (GSB) of the NCs respectively. The presence of the An-X transmitters results in a faster recovery of the NC's GSB and decay of the ESA (see Fig. 7.2d for CdSe/An-PO<sub>3</sub>H<sub>2</sub> and the other ligands in Chapter 8).

Ligands with high upconversion QYs show high TET efficiencies (Fig. 7.3a), and no clear correlation with the TET rate constants,  $k_{TET}$ , that occur between  $10^9$  to  $10^{10}$  s<sup>-1</sup>. We monitor the kinetics of the anthracene triplet state at 437 nm where its broad  $T_1$ - $T_n$  transition occurs. As this overlaps with the ESA of the NCs,  $k_{TET}$  is extracted at 437 nm by globally fitting the growth of the molecular  $T_1$ - $T_n$  peak in addition to the time constants obtained from the GSB of the NC at 463 nm.  $\Phi_{TET}$  is calculated based on the maximum in the  $T_1$ - $T_n$  absorption obtained from the prefactor of the single exponential corresponding to  $k_{TET}$  (see Chapter 8 for details).  $k_{TET}$  and  $\Phi_{TET}$  are summarized in Table 7.2. We see that  $\Phi_{TET}$  is directly correlated to upconversion QYs. For the ligands with a high  $\Phi_{UC}$  such as An-PO<sub>3</sub>H<sub>2</sub> and An-Im,  $\Phi_{TET}$  is 11-12 %. Conversely, the ligands with low  $\Phi_{UC}$ , e.g. An-SH,  $\Phi_{TET} = 2\%$ . An-NH<sub>2</sub> and An-PhNH<sub>2</sub> have similar  $\Phi_{TET}$  from NC to transmitter but the  $\Phi_{UC}$  of An-PhNH<sub>2</sub> (3.56%) is higher than An-NH<sub>2</sub> (0.789%), indicating more efficient TET from An-PhNH<sub>2</sub> to annihilator DPA. The sterically hindered phenyl ring in An-PhNH<sub>2</sub> might mitigate triplet excimer formation or triplet-triplet annihilation between two neighboring ligands.

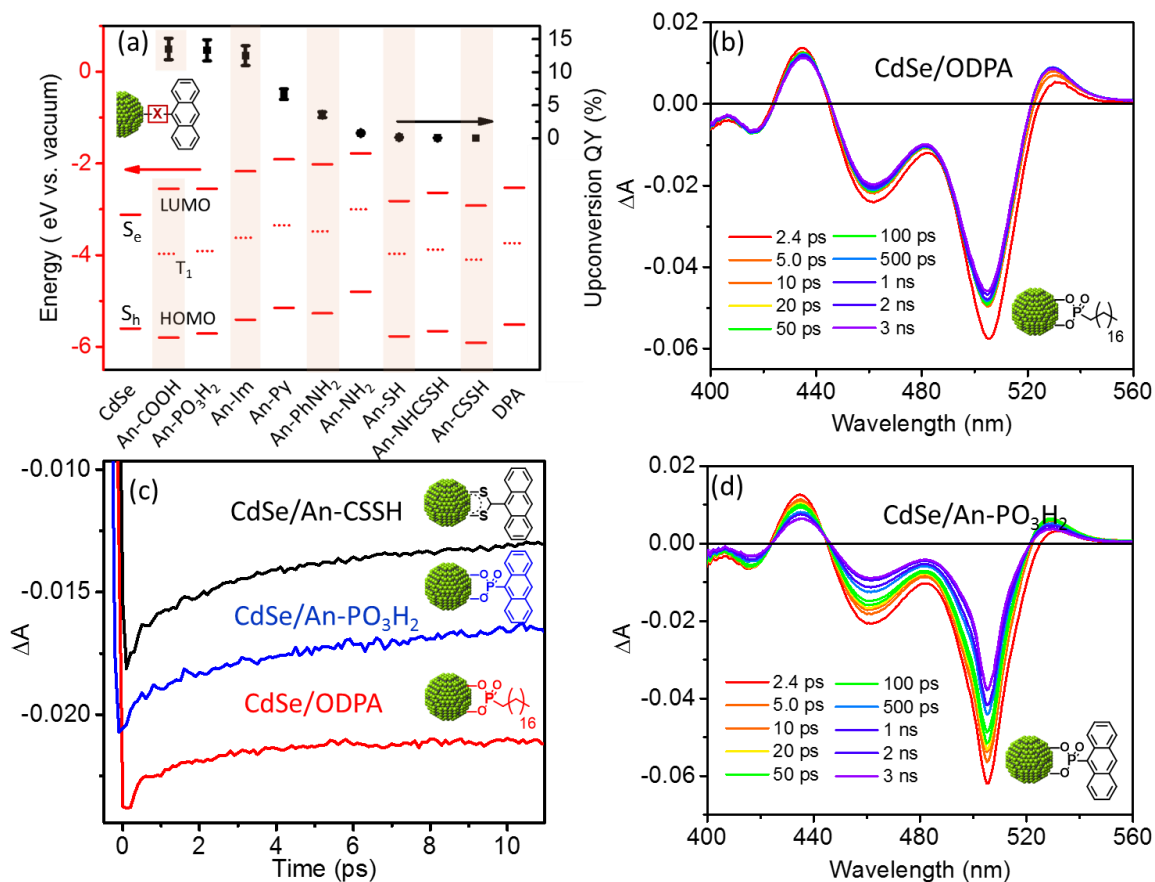


**Figure 7.2.** (a) The HOMO and LUMO energy levels (red solid line) and  $T_1$  state (relative to HOMO, red dashed line) versus vacuum for CdSe NCs (left), anthracene ligands with functional group X (An-X) and DPA (right) and the photon upconversion QYs (black square) from Table 7.1. See text for details. (b) Femtosecond transient absorption spectra of CdSe NCs capped with native ligand octadecylphosphonic acid (ODPA), and (d) An- $PO_3H_2$ . (c) The initial ground state bleach at 463 nm corresponding to CdSe/ODPA (red), CdSe/An- $PO_3H_2$  (blue) and CdSe/An-CSSH (black) in hexane at RT. Samples are dissolved in hexane and excited with a 505 nm pulsed laser.

For the sulfur containing ligands and An- $NH_2$ , photon upconversion is limited by ligand-induced depletion of the CdSe exciton that occurs fast, beyond the resolution of our TA setup. In principle, the population of photoexcited CdSe NCs should be proportional to the concentration of CdSe NCs. However, after normalizing the kinetics of the GSB of the NC at 468 nm by the steady state absorption at 505 nm for each sample, there is a marked

decrease in the initial amplitude of the exciton bleach of CdSe NCs capped with anthracene ligands compared to the original CdSe/ODPA. This is shown in Fig. 7.2c for CdSe/ODPA, CdSe/An-PO<sub>3</sub>H<sub>2</sub> and CdSe/An-CSSH, while data for the other ligands are available in the Chapter 8. This decrease,  $\Delta_{XB}$ , is defined as:

$$\Delta_{XB} = \frac{\Delta A_0(\text{CdSe / ODPA}) - \Delta A_0(\text{CdSe / An - X})}{\Delta A_0(\text{CdSe / ODPA})} \quad (7.1)$$

where  $\Delta A_0$  is the absorption at 468 nm at time zero for different samples.  $\Delta_{XB}$  for different ligands are listed in Table 7.2. As shown in Fig. 7.3a,  $\Delta_{XB}$  negatively correlates with the upconversion QYs.  $\Delta_{XB}$  indicates there are some fast, sub-picosecond decay channels that are not resolved in our experiments. Possible loss mechanisms could stem from ultrafast photoinduced charge transfer from CdSe NCs to bound ligands, or surface-based trap states introduced during ligand exchange. Note that no evidence for the radical cation or anion of anthracene was observed in any of the TA spectra.

**Table 7.2.** The rate of triplet energy transfer (TET),  $k_{TET}$ ; the normalized  $k_{TET}$ ,  $k_{TET}/N$ ; TET efficiency  $\Phi_{TET}$ ; and the relative decrease of initial exciton bleach of CdSe NCs monitored at 463 nm due to An-X,  $\Delta_{XB}$ .

Ligand	$k_{TET}$ (s <sup>-1</sup> )	$k_{TET}/N$ (s <sup>-1</sup> )	$\Phi_{TET}$ (%)	$\Delta_{XB}$ (%)
An-PO <sub>3</sub> H <sub>2</sub>	4.26E+09	5.72E+08	12.34	13.0
An-Im	4.16E+09	3.01E+08	11.20	10.1
An-Py	7.57E+09	5.53E+08	4.73	10.1
An-PhNH <sub>2</sub>	1.33E+10	3.98E+09	3.65	16.3
An-NH <sub>2</sub>	1.14E+10	2.43E+10	3.70	17.9
An-SH	6.64E+09	- <sup>a</sup>	2.23	17.7
An-NHCSSH	4.69E+09	- <sup>a</sup>	0.93	23.2
An-CSSH	0	- <sup>a</sup>	0	23.9

<sup>a</sup>not calculated due to the low value of  $N$ ;

### 7.3 Discussion

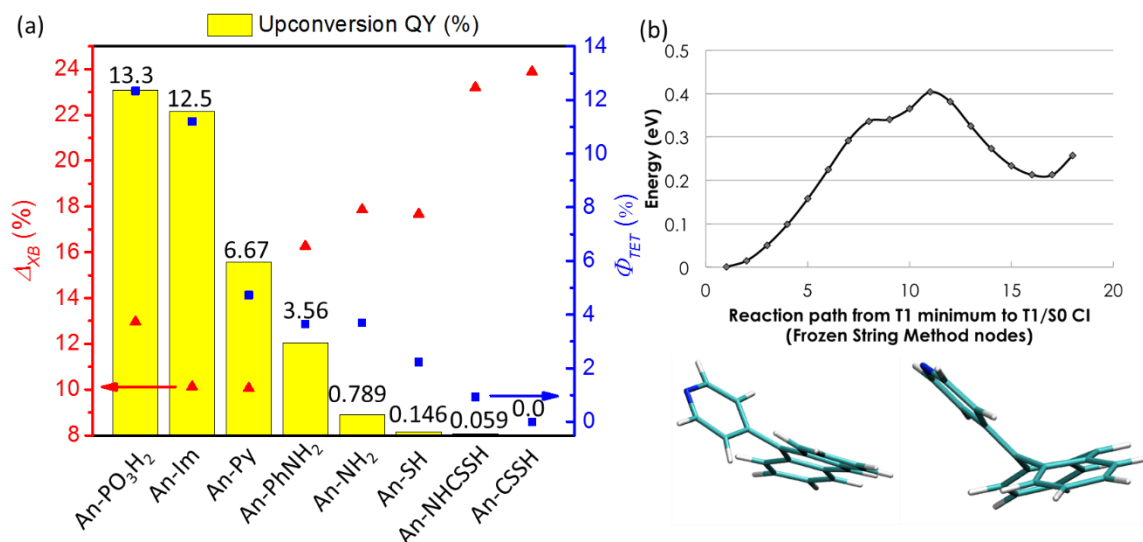


**Figure 7.3.** (a) Histogram of the photon upconversion QY for anthracene ligands (yellow bars), plotted with the relative decrease of initial exciton bleach of the CdSe NC donor ( $\Delta_{XB}$ , red triangles, left), and the TET efficiency  $\Phi_{TET}$  (blue squares, right) listed in Table 7.1 and 7.2. (b) The energetics of the reaction path on the T<sub>1</sub> surface of An-Py going from the T<sub>1</sub> minimum-energy geometry to the T<sub>1</sub>/S<sub>0</sub> minimum-energy crossing point geometry, as computed using nodes and the freezing string method.<sup>200</sup> The first node is at the global minimum and the final node is at the intersection between the T<sub>1</sub> and S<sub>0</sub> potential energy surfaces. The lower-left structure displays the geometry of An-Py near the global minimum (node 1 on the reaction path above); the lower-right structure is of the local minimum near the minimum-energy crossing point (node 16 on the reaction path above) with the S<sub>0</sub> surface, only 0.20 eV above the global minimum. This local minimum seems to be caused by steric clashing between the ortho hydrogens on the aryl groups and the hydrogens in the 1 and 8 positions on the anthracene. This local minimum on the T<sub>1</sub> surface can confine the anthracene near a T<sub>1</sub>/S<sub>0</sub> conical intersection, accelerating intersystem crossing between the two states and lowering the triplet lifetime.

Calculations show that the sulfur-containing ligands have relatively strong T<sub>1</sub>/S<sub>0</sub> coupling, leading to a short triplet lifetime that impedes TET from anthracene ligands to the DPA annihilator and thus low photon upconversion QYs. We looked at the energetic cost of accessing the T<sub>1</sub>/S<sub>0</sub> minimum-energy crossing point, as well as the T<sub>1</sub>/S<sub>0</sub> spin-orbit coupling constants (see Chapter 8). There was minimal variation in the ligands with the

exception of the dithiolate An-CSSH, for which the  $T_1/S_0$  minimum-energy crossing point is not much above the minimum (0.18 eV). Other than An-CSSH, An-NHCSSH also possesses spin-orbit coupling constants exceeding  $100 \text{ cm}^{-1}$ . An-SH has a spin-orbit coupling constant of  $6 \text{ cm}^{-1}$ , which may also be sufficient to affect the efficiency of transfer from the ligand to DPA.

The short lifetime of An-Py and An-PhNH<sub>2</sub> is due to strong coupling between their  $T_1$  and  $S_0$  states. We observe an interesting feature in An-Py and An-PhNH<sub>2</sub>: a local minimum on the  $T_1$  surface near the CI (see Fig. 7.3b), which is absent in the other species. This local minimum is caused by steric clashes between the ortho hydrogens of the aryl side groups and the hydrogens in the 1 and 8 positions on the anthracenes. This can trap the ligand into a conformation from which the CI is both more accessible and more “peaked”, a feature which is thought to speed up transfer through the CI.<sup>201</sup> This helps explain why An-Py and An-PhNH<sub>2</sub> has a shorter triplet lifetime and lower upconversion QY than An-Im, despite their similar chemistries.

In addition to the triplet lifetime, we found that electronic coupling between the triplet states on the NC and the anthracene transmitter must be “just right” to promote TET and upconversion. This electronic coupling is calculated by Constrained Density Functional Theory with Configuration Interaction (CDFT-CI) and summarized in Table 7.3.<sup>182,202-204</sup> While there is no overall trend, several explanations emerge to help differentiate between similar ligands. The top three performing ligands (An-COOH, An-PO<sub>3</sub>H<sub>2</sub>, and An-Im) share a similar coupling of 5-10  $\mu\text{Ha}$ , and ligands with too strong (48.3  $\mu\text{Ha}$  for An-NH<sub>2</sub>) or too weak (0.2  $\mu\text{Ha}$  for An-SH) coupling lead to a low upconversion

QY. This suggests a “Goldilocks” effect of the triplet state coupling on the upconversion QY. As expected, An-PhNH<sub>2</sub> has a lower coupling than An-NH<sub>2</sub>, since it is further away from the NC. However, An-PhNH<sub>2</sub> has a higher photon upconversion QY than An-NH<sub>2</sub> (3.6 % compared to 0.8 %) despite containing a phenyl spacer which serves as a tunneling barrier (T<sub>1</sub> benzene ~3.8 eV). This is because An-PhNH<sub>2</sub> has a coupling similar to the top performers, again suggesting that a “just right” coupling might be needed. Additionally, comparing the two *N*-heterocycles, An-Py has an order of magnitude smaller coupling to the CdSe NC than An-Im (Table 7.3), explaining its lower  $\Phi_{UC}$ .

**Table 7.3.** Constrained Density Functional Theory with Configuration Interaction (CDFT-CI) calculations for electronic couplings between a triplet on the NC and a triplet on the ligand.

Ligand	Coupling to NC ( $\mu\text{Ha}$ )
An-COOH	4.6
An-PO <sub>3</sub> H <sub>2</sub>	9.9
An-Im	12.8
An-Py	0.9
An-PhNH <sub>2</sub>	7.7
An-NH <sub>2</sub>	48.3
An-SH	0.2

The upconversion QY is correlated with the binding affinity of ligands to CdSe NCs. Here, we compare the pK<sub>b</sub> of 4 ligands where the binding group X is aromatic.  $\Phi_{UC}$  decreases from 12.5% to 6.7%, 3.9% and 3.6% from X = imidazole (Im), pyridine (Py), benzoic acid (PhCOOH)<sup>37</sup> and aniline (PhNH<sub>2</sub>) respectively. The pK<sub>b</sub> of Im, Py, PhCOO<sup>-</sup> (conjugated base of PhCOOH with pK<sub>a</sub> of 4.2) and PhNH<sub>2</sub> are 7.0 and 8.8, 9.8 and 9.1<sup>205</sup> respectively, consistent with  $\Phi_{UC}$ . A stronger base potentially enhances electronic coupling

by forming a stronger bond with the NC. In this series, imidazole is the strongest base and best nucleophile with the highest  $\Phi_{UC}$ . When X is aliphatic, An-PO<sub>3</sub>H<sub>2</sub> is the best performing transmitter likely because the phosphonic acid group binds CdSe NCs strongly. NMR experiments have shown that phosphonic acid displaces oleic acid ligands on CdSe NCs, and it is virtually impossible to displace all the phosphonic acid ligands in the presence of excess oleic acid even at high temperatures of ~300 °C.<sup>55,67,68</sup>

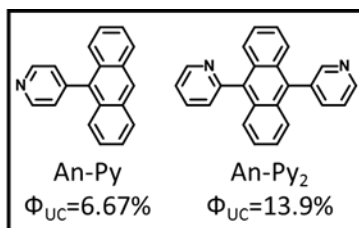


**Figure 7.4.** Structures of An-Py and An-Py<sub>2</sub> transmitters and their upconversion QYs,  $\Phi_{UC}$ , in the presence of CdSe light absorbers and DPA emitters.

The critical nature of transmitter conformation is seen when comparing An-Py and An-Py<sub>2</sub>, an anthracene ligand substituted at the 9 and 10 positions with two pyridines.<sup>73</sup> An-Py<sub>2</sub> as transmitter results in an upconversion QY of ~14%, more than double that of An-Py (6.7%). This is because An-Py<sub>2</sub> binds in a manner complementary to the NC surface, probably in a bidentate fashion that allows the anthracene core to be closer to the CdSe for better orbital overlap and hence improved TET. Indeed, anthracene isomers with the COOH and NHCSSH groups on 1, 2, and 9-position of the anthracene ring modulate the energy of the excitonic states in anthracene,<sup>206</sup> or the orbital overlap between anthracene and CdSe NCs, resulting in very different rates of TET and photon upconversion.<sup>80</sup>



## 7.4 Conclusion

In conclusion, this work demonstrates that TET from CdSe NCs to bound anthracenes are strongly affected by the binding affinity, docking geometry, sterics, intramolecular spin-orbit coupling and molecule-nanocrystal triplet-triplet coupling of the anchoring groups. The best performing anthracene ligands with phosphonic acid, carboxylic acid and imidazole have upconversion QYs of 12.5-13.5%. The upconversion QY correlates with the TET efficiency,  $\Phi_{TET}$ , and is inversely proportional to the ligand induced quenching of the CdSe NC, but not with the energy levels of the HOMOs or LUMOs, or the rate of TET,  $k_{TET}$ . TDDFT and CDFT-CI calculations performed on these anthracene ligands indicate that a good triplet acceptor should have weak internal conversion ( $S_1/S_0$  coupling), slow intersystem crossing ( $T_1/S_0$  coupling), and an electronic coupling of the triplet states between ligands and CdSe NCs that is 'just right' for efficient TET. This work provides a guide to the rational design of the triplet acceptors for efficient TET, a key bottleneck for triplet fusion based photon upconversion for applications in solar energy, photocatalysis and bioimaging.

## **Chapter 8    Supporting Information**

### **8.1    Chemicals**

Chemical reagents were purchased from Aldrich Chemical Co, Strem, TCI America, or Alfa Aesar and were used as received. Dry and degassed acetonitrile, THF, toluene were obtained from JC Meyer's solvent purification system. Dry and degassed hexane and methanol were purchased from Sigma-Aldrich and bubbled with argon before use. Acetone was purchased from Fisher Scientific, dried and degassed before use.

### **8.2    Instrument**

Absorption spectra were recorded on a Jasco-V670 UV-Vis absorption spectrophotometer. Ensemble fluorescence spectra were recorded on a HORIBA FluoroMax-3 fluorometer. Upconversion fluorescence spectra were recorded on an Ocean Optics Inc. JAZ spectrometer. Upconversion fluorescence signals for the power-dependence and quantum yield measurements were acquired using a Hamamatsu H5783 photomultiplier tube equipped with interference and edge filters to isolate the RUB and DPA emission wavelengths. Lasers used: 532 nm light was obtained from a Coherent Sapphire diode laser, with an output power of 10 mW. 800 nm laser light was obtained from a Kapteyn-Murnane Labs Ti:Sapphire laser pumped by a Spectra Physics Millennia laser. The laser was operated in cw mode. 980 nm laser light was obtained from a Amonics ALS-980-MM-1-SA fiber-coupled diode laser.

Time-resolved photoluminescence (TRPL) experiments for CdSe/CdS and CdSe/ZnS core-shell NCs were done on a HORIBA Fluorolog fluorometer with a 406 nm NanoLED-405LH pulse laser and HORIBA TBX picosecond photon detection module.

The quantitative analysis of Cd, Zn and Se of nanocrystals from ICP-AES was done on a Perkin-Elmer Optima 2000 DV inductively coupled plasma – atomic emission spectrometer (ICP-AES). TRPL for all other systems were done with a diode-pumped (Verdi, Coherent) Ti:Sapphire oscillator (Vitesse, Coherent) and Nd:YLF pumped (Evolution, Coherent) regenerative amplifier (Libra) yields 800 nm 100 fs pulses at 1 kHz (3.8 W). PbSe/RUB and RUB-only samples were excited with the 800 nm fundamental. CdSe/ODPA, CdSe/9ACA/DPA and DPA-only samples were excited at 400 nm with frequency doubled 800 nm (BBO). The sample (1 cm capped quartz cuvette) was placed such that the incident excitation beam (0.1 W) was focused (focal length = 20 cm) on the sample. The fluorescence was collected using front-face detection at an angle of ~10 degrees with respect to the excitation beam. The emission was collected with a lens (f = 20 cm) and then imaged (f= 5 cm) into a Hamamatsu C4334 streak camera detector. Residual 800 nm and 400 nm were removed with a hot-mirror and a long-wave pass 420 nm filter before the detector, respectively. Time-resolved data for the CdSe/ODPA, CdSe/9ACA/DPA and DPA-only samples were collected using 1 ns and 100 ns sweep windows with a center collection wavelength of 570 nm. PbSe/RUB and RUB-only time-resolved data were collected at 100 ns and 500 ns sweep windows with a center collection wavelength of 600 nm.

Transmission electron microscopy was performed on a Tecnai12 TEM. NMR spectra were recorded on a Varian Inova-400MHz NMR spectrometer at room temperature. The  $^1\text{H}$  Chemical shifts ( $\delta$ ) are reported in parts per million with residual solvent ( $\text{CHCl}_3$ ) peak as an internal standard.

The femtosecond transient absorption is based on a regenerative amplified Ti:Sapphire femtosecond laser system (Coherent Legend, 1 kHz repetition rate, ~150 fs pulse duration and 2.4 mJ/pulse 800 nm fundamental pulse energy). The data collection used Helios system from Ultrafast Systems, Inc. In short, the fundamental pulse was split in two parts with a 90:10 beam splitter. An 800 nm pulse with ~200  $\mu$ J, after being adjusted by a variable ND filter and an iris, was focused into a crystal window to generate a white light continuum (WLC) probe. In this experiment, the transient absorption data within 1 ns time window was studied by two crystals with different probe ranges. Then the WLC was split by a 70:30 beam splitter to provide the probe for the sample and reference to correct for the intrinsic fluctuation. The probe beam was focused onto the sample and eventually focused into an optical fiber entrance. The optical fiber is coupled with visible spectrometer and then a 1024 elements CMOS camera. The 400 nm pump pulse was generated by passing 0.2 mJ 800 nm pulse into a type 1 BBO crystal to generate ~30  $\mu$ J 400 nm pulse. A chopper modulated the pump by 500 Hz to cut off every other pump pulse to provide transient absorption signal. The diameter on the sample for pump and probe, is 400  $\mu$ m and 100  $\mu$ m, respectively. The typical instrument response is well fitted by a Gaussian function with ~200 fs FWHM. The chirp was corrected by fitting the solvent response in all data set.

The nanosecond transient absorption data was collected using EOS system from Ultrafast Systems, Inc. In short, the pump pulse was provided the same way as in the femtosecond setup. The probe pulse was generated by 20 kHz WLC laser (STM-2-UV, Leukos).

The sample was contained in 1 mm quartz cell (Starna) and was constantly stirred during the experiment to avoid photodegradation. The sample was loaded in glovebox (M Braun) and was air-tight during experiments. All experiments were performed at room temperature.

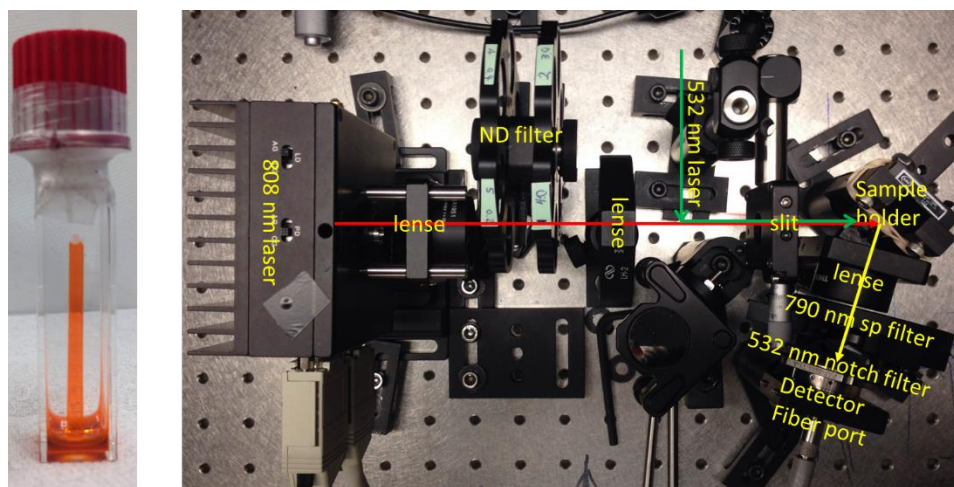


**Figure 8.1.** Setup of NIR upconversion measurements. Photos of a cuvette containing the sample in a 100  $\mu\text{m}$  thick capillary tube (left) and the upconversion measurement setup (right). Each part is described under the Instrumentation section.

### 8.3 Nanocrystal synthesis

#### 8.3.1 Synthesis of CdSe nanocrystals

CdSe nanocrystals (NCs) were synthesized and purified by the procedure published by Carbone et al.<sup>207</sup> Trioctylphosphine oxide (TOPO) (3.0g), octadecylphosphonic acid (ODPA) (0.280g) and CdO (0.060g) were mixed in a 25mL three neck flask, heated to ca. 150°C and exposed to vacuum for 1 hour. Then, under Ar (g), the solution was heated to above 300°C to dissolve the CdO until it formed a clear light yellow solution. At this point, 1.5 g of trioctylphosphine (TOP) was injected and the temperature was allowed to recover to the value required for the injection of the Se:TOP solution (0.058g Se + 0.360g TOP) to

create a NC with a specific diameter. For example, for the synthesis of 3.28 nm diameter CdSe, the injection temperature was 375 °C. Immediately after injection, the reaction flask was cooled down quickly with compressed air. After the synthesis, as-prepared CdSe NCs were transferred to the glove box and cleaned with methanol and toluene at least three times. The final pellet was dissolved in toluene and stored inside a nitrogen glove box for future use. The NC concentration and diameter was determined by measuring the absorbance at the first exciton absorption maxima and calculated according to Yu et. al<sup>108</sup>. The photoluminescence quantum yield of the 3.28 nm diameter particles was measured to be 0.12 using Rhodamine6G (quantum yield = 0.95) as the standard.

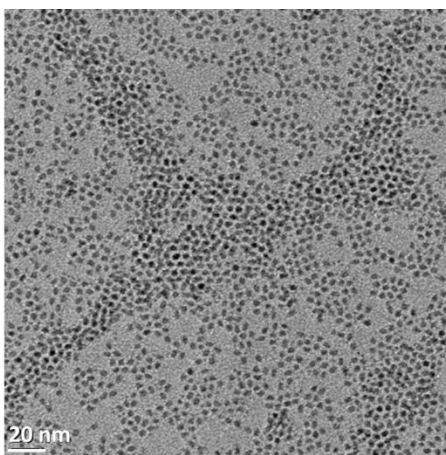


**Figure 8.2.** TEM of the 3.28 nm diameter CdSe NCs.

### 8.3.2 Synthesis of PbS nanocrystals<sup>208</sup>

PbO (0.45 g), oleic acid (OA, 10 mL), and 1-octadecene (ODE, 10 mL) were mixed in a 50 ml three-neck flask and heated to 110 °C under vacuum for an hour. Pb oleate is formed, indicated by the discoloration of the reaction to a clear light yellow solution. Then, the reaction flask was backfilled with Ar (g), and heated to 150 °C. At 150 °C, the sulfide

precursor, containing 0.21 mL of bis(trimethylsilyl)sulfide in 10 mL of anhydrous ODE, was injected, and the temperature dropped to about 130 °C. The reaction flask was allowed to cool down to 100°C for 3 min by turning off the heater. Then the reaction flask was kept at 100 °C for 5 min. The PbS NCs were transferred to a glovebox and washed 3 times by adding 1:1 hexanes/ethanol mixture; followed by centrifuging at 7000 rpm for 5 min. The supernatant was discarded. The final pellet was dissolved in hexane and stored in the dark inside the glovebox for future use. The PbS NC size (3.1 nm diameter) was determined by measuring the energy of the first exciton peak. The concentration of the PbS NCs was determined from the absorption at 400 nm<sup>107</sup>.

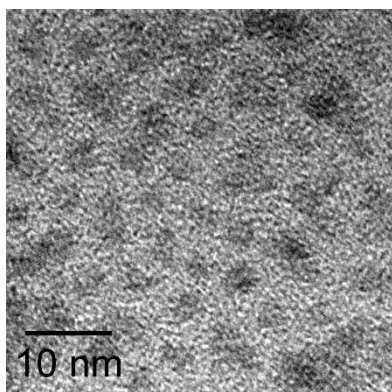


**Figure 8.3.** TEM image of the 3.10 nm diameter PbS nanoparticles.

### 8.3.3 Synthesis of PbSe nanocrystals

The same general method as above was used, with the only difference being that a selenide precursor was used, i.e. 0.21 ml bis(trimethylsilyl)selenide instead of 0.21 ml bis(trimethylsilyl)sulfide. The size and concentration of PbSe nanocrystals were determined by measuring the energy of the first exciton peak and the absorption at 400 nm respectively<sup>8</sup>.

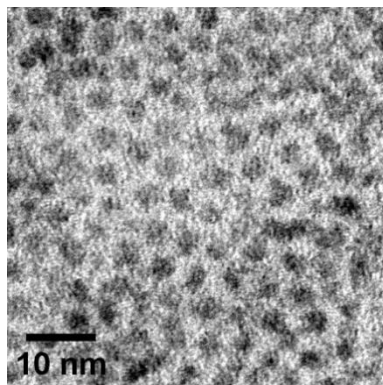


**Figure 8.4.** TEM image of 2.10 nm diameter PbSe nanoparticles.

#### 8.3.4 Synthesis of CdSe/CdS and CdSe/ZnS core-shell NCs

CdSe cores with diameter of 2.9 nm was synthesized following the procedure published by Carbone *et al.*<sup>209</sup> CdSe/CdS,<sup>210</sup> and CdSe/ZnS<sup>211</sup> core-shell NCs were synthesized by following the methods published by the Bawendi group. The amount of precursor was calculated based on the size and concentration of CdSe core<sup>212</sup>, the expected shell thickness, and the bulk density of CdS and ZnS.<sup>205</sup> The extinction coefficient of core-shell NCs at absorption maxima are taken from that for CdSe core.<sup>212</sup>



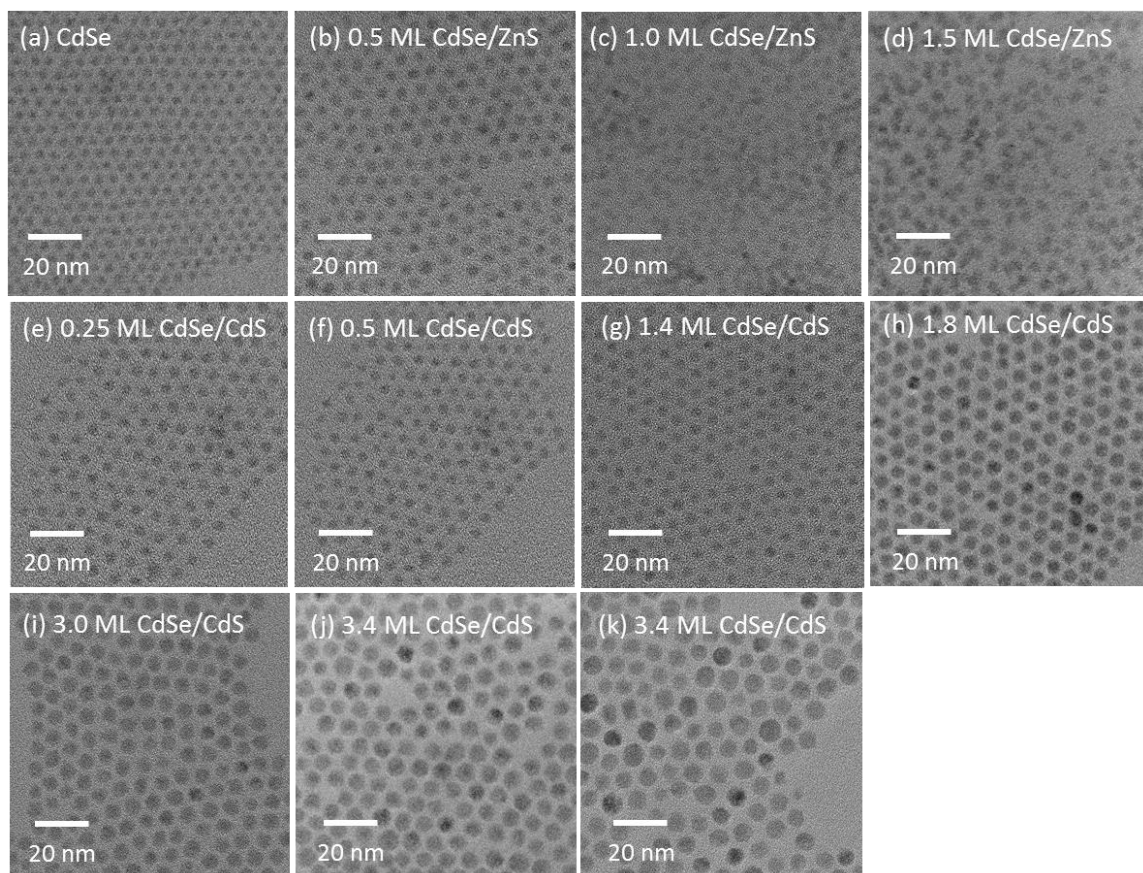


**Figure 8.5.** The TEM images of (a) 2.9 nm diameter CdSe core, (b-d) CdSe/ZnS and (e-k) CdSe/CdS core-shell NCs of different shell thickness.

### 8.3.5 Synthesis of PbS and PbS/CdS QD.

2.7 nm diameter PbS QD were synthesized following the method of Hines and Scholes.<sup>1</sup>

3.2 nm diameter PbS/CdS core-shell QD was synthesized with cation exchange.<sup>2</sup> First, a cadmium-oleate stock solution was made by dissolving 30 mg of  $\text{Cd}(\text{OAc})_2 \cdot \text{H}_2\text{O}$  in 88.7  $\mu\text{L}$  of oleic acid and 347.9  $\mu\text{L}$  of 1-octadecene at 120 °C until a clear solution forms. 176  $\mu\text{L}$  of this Cd-oleate stock solution was transferred into 4 mL vials. Then 277  $\mu\text{L}$  of 30 mg/mL of 3.2 nm diameter PbS core solution was injected to the Cd-oleate solution while stirring at 90 °C. Right after injection, the temperature was set to 80 °C. After 19 min,

0.416 mL of hexane was injected to quench the reaction. The QD were precipitated with acetone and centrifuging at 7800 rpm for 5 min. The black pellet was then redispersed in hexane. The precipitation/redispersion procedure was repeated three more times with a combination of methanol/ hexane. After the final precipitation, the QD were dissolved in 1 mL toluene and stored in the glovebox in the dark. The thickness of the CdS shell on the QD was determined by the difference of the QD sizes before and after cation exchange reaction based on the absorption  $\lambda_{\max}$  of the PbS core. The concentration of QD were determined by the absorption at 400 nm.<sup>3</sup>

## 8.4 Synthesis of transmitter ligands

### 8.4.1 Synthesis of 5-CPT

#### 1) synthesis of ethyl 4-(tetracen-5-yl) benzoate<sup>6</sup>

To a mixture of 5-Bromo-tetracene<sup>7</sup> (0.5g, 1.63mmol), 4-(ethoxycarbonyl) phenylboronic acid (380mg, 1.96mmol, 1.2 mol amt.), cesium carbonate (2.12g, 6.53mmol, 4 mol amt.), toluene (19.4ml) and H<sub>2</sub>O (6.536ml) were added. The reaction was bubbled under argon for 20 min, followed by the addition of 1,1'-Bis diphenylphosphinoferrocene-palladium(II)dichloride dichloromethane complex (133.4mg, 0.1634mmol, 0.1 mol amt.) the mixture was then stirred at 60°C overnight. The reaction was cooled then washed with H<sub>2</sub>O, and extracted with ethyl acetate four times. The organic layer was washed with brine, dried with magnesium sulfate, filtered and then concentrated using the rotary evaporator. The crude product was purified by flash column chromatography using silica gel and dichloromethane as the eluent to give an orange powder with 61% yield. <sup>1</sup>H NMR (400MHz, CDCl<sub>3</sub>):  $\delta$  1.49 (t, 3H), 4.52 (q, 2H), 7.42-7.31 (m, 4H), 7.62-7.57 (m,

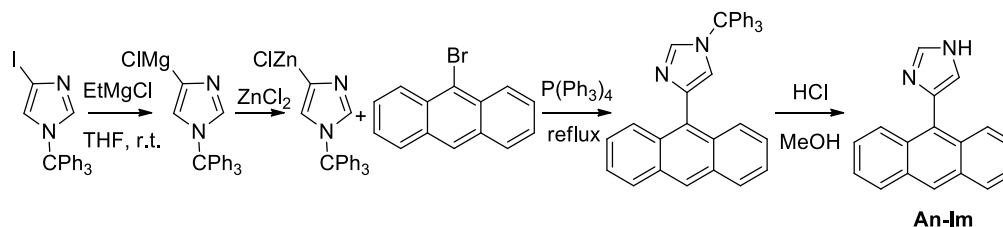
3H), 7.80 (d, 1H), 7.99 (d, 1H), 8.06 (d, 1H), 8.20 (s, 1H), 8.34 (d, 2H), 8.72 (s, 1H), 8.76 (s, 1H) ppm.  $^{13}\text{C}$  NMR (400MHz,  $\text{CDCl}_3$ ):  $\delta$  14.61, 61.32, 125.05, 125.28, 125.43, 125.61, 125.66, 126.50, 126.72, 127.41, 128.10, 128.76, 128.79, 129.11, 129.53, 129.90, 129.91, 130.01, 130.05, 131.22, 131.36, 131.77, 135.72, 144.23, 166.84 ppm; HRMS (ESI) Calcd. for  $\text{C}_{27}\text{H}_{20}\text{O}_2$  ( $\text{MH}^+$ ) 377.1536, Found 377.1551.

## 2) synthesis of 4-(tetracen-5-yl) benzoic acid (CPT)<sup>8</sup>

To a suspension of ethyl 4-(tetracen-5-yl) benzoate (0.5g, 1.32mmol) in 154.4ml of tetrahydrofuran-methanol (1:1), 3.32ml of a 2M KOH aqueous solution was added. The mixture was then bubbled for 20min under argon, then allowed to reflux for 3 hours. THF was removed and the resulting suspension was acidified with 2M of HCl. The crude solid was filtered and washed with  $\text{H}_2\text{O}$  then hot chloroform to give the desired product (orange powder) at 64% yield.  $^1\text{H}$  NMR (400MHz, DMSO):  $\delta$  7.29-7.42 (m, 4H), 7.61 (d, 1H), 7.68 (d, 2H), 7.82 (d, 1H), 8.08 (d, 2H), 8.21 (s, 1H), 8.42 (d, 2H), 8.73 (s, 1H), 8.79 (s, 1H) ppm.  $^{13}\text{C}$  NMR (400MHz, DMSO):  $\delta$  125.05, 125.76, 126.34, 126.35, 126.72, 127.42, 127.94, 128.52, 128.94, 129.13, 129.31, 129.46, 129.97, 130.40, 130.97, 131.30, 131.43, 131.83, 132.11, 132.14, 135.80, 143.61, 167.96 ppm. HRMS (ESI) Calcd. for  $\text{C}_{25}\text{H}_{16}\text{O}_2$  ( $\text{M}^{*+}$ ) 348.1145, Found 348.1160.

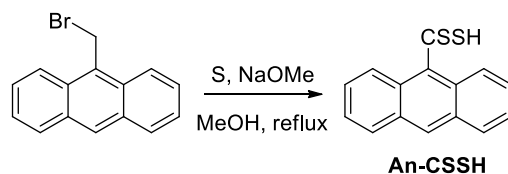
### 8.4.2 Synthesis of CdSe NCs and anthracene ligands with different functional groups.

2.4 nm diameter CdSe NCs,<sup>209</sup> An-NH<sub>2</sub>,<sup>213</sup> An-SH,<sup>214</sup> An-NHCSSH,<sup>80</sup> An-PhNH<sub>2</sub>,<sup>191</sup> An-PO<sub>3</sub>H<sub>2</sub>,<sup>215,216</sup> An-Py<sup>217</sup> were synthesized by following the reported methods. All synthesized anthracene ligands are recrystallized in THF/hexane three times before use. An-COOH was purchased from TCI America and used as received.



An-Im was synthesized following published work<sup>218</sup> with modifications:

2 M EtMgCl in EtO<sub>2</sub> (2.75 mmol, 1.38 mL) was added slowly to a solution of 4-iodo-1-trityl-1H-imidazole (1.00 g, 2.29 mmol) in THF (20.8 mL). The mixture was stirred at r.t for 30 min. Then ZnCl<sub>2</sub> (62.5 mg, 0.46 mmol) was added and the solution was stirred at r.t. for 1 h, which is then treated with 9-bromoanthracene (107.2 mg, 0.42 mmol) and Pd(PPh<sub>3</sub>)<sub>4</sub> (24.1 mg, 0.2 mmol). The reaction was heated at reflux for 12 h, then the solution was cooled and quenched with NH<sub>4</sub>Cl aqueous solution, and then washed with water. The organic layer was dried with MgSO<sub>4</sub>, filtered and evaporated in vacuum. The residue was purified by flash chromatography (EtOAc: hexane= 8:2), and then detritylated by reflux in HCl (3.0 equiv.)/MeOH (20 mL). The product was washed with NaHCO<sub>3</sub> (aq), extracted with Et<sub>2</sub>O, dried with MgSO<sub>4</sub>. After removing the solvent by vacuum, the product An-Im was formed with the total yield of 50.7%. <sup>1</sup>H NMR (400 MHz, (CD<sub>3</sub>)<sub>2</sub>SO): δ<sub>H</sub> = 8.55 (s, 1H), 8.07 (d, 4H, J=1.0 Hz), 7.81 (s, 1H), 7.49 (m, 2H), 7.42 (m, 2H), 7.23 (s, 1H) ppm. <sup>13</sup>C NMR (400 MHz, (CD<sub>3</sub>)<sub>2</sub>SO): δ<sub>C</sub> = 144.25, 135.99, 133.75, 131.63, 130.16, 129.19, 128.75, 127.77, 124.94, 123.69, 123.17 ppm. HRMS (-ESI/APCI) (mass m/z): 245.0979 [M+H]<sup>+</sup>.



An-CSSH was synthesized following published work<sup>219</sup> with modifications:

S (364.4 mg, 10.8 mmol, Sigma-Aldrich, used as received) and NaOMe in methanol (5.4 M, 2 mL) were mixed and refluxed for 2 hrs, then 9-bromomethylanthracene<sup>220</sup> (254.4 mg, 0.94 mmol) was added, and reflux for another 15 hrs. Then, solvent was evaporated by vacuum and the crude product was dissolved in H<sub>2</sub>O to form a dark red solution. After filtering out the undissolved solid, the filtrate was dried on vacuum. The product was then transferred into an argon glovebox, dissolved in the mixture of acetone and dichloromethane (1:1 v/v) and filtered by silica gel. The solvent was removed by vacuum to provide dark red solid with the yield of 91.1%. <sup>1</sup>H NMR (400 MHz, D<sub>2</sub>O): δ<sub>H</sub> = 10.76 (s, 1H), 9.20 (d, 2H, J=8.0 Hz), 8.81 (d, 2H, J=8.8 Hz), 7.62 (m, 2H), 7.47 (m, 2H) ppm. <sup>13</sup>C NMR (400 MHz, D<sub>2</sub>O): δ<sub>C</sub> = 192.31, 132.43, 132.28, 129.49, 125.80, 124.02, 123.82, 123.46, 122.72 ppm. HRMS (-ESI/APCI) (mass m/z): 255.1400 [M+H]<sup>+</sup> (weak).

As with the color of anthracene ligands, An-SH is light orange, and An-NH<sub>2</sub> is a brown solid, as opposed to the yellow powder for the other anthracene ligands. An-CSSH is a dark red solid and is easily oxidized in the acid form. Therefore, workup and purification was done in the deprotonated form under the protection of inert gas.

## 8.5 Preparation of samples for upconversion, TA and TRPL measurements

CdSe: 0.797 ml of 3.28 nm diameter CdSe NCs in toluene (with a concentration of 2.51\*10<sup>-5</sup>M) and 1.96 ml of 9-ACA in a mixture of acetonitrile:toluene = 3:11(v/v) solution

(with a concentration of 0.0216 M) were mixed and stirred for 1.5 hours. An equal volume of acetone was added. The resulting solution was centrifuged at 7830 rpm for 10 min. The resulting pellet was redispersed in 0.98 ml toluene, followed by adding 20  $\mu$ L of a 0.05M DPA toluene solution. The entire procedure was performed in a nitrogen glovebox. Note that the solubility of 9-ACA reaches a limit of 0.0216M in 3:11(v/v) acetonitrile: toluene. Upconversion samples were prepared in a N<sub>2</sub> glovebox with air-free cuvettes sealed with parafilm.

PbS: Ligand exchange reaction was performed by mixing 10  $\mu$ M QD with 500  $\mu$ M **5-CT** in toluene (total volume 0.3 mL) and stirring for 40 min. 1.2 mL acetone was added to precipitate the QD//**5-CT** complex following centrifuging for 5 min at 7830 rpm. The clear supernatant was discarded. For the upconversion sample, the pellet was redispersed in 20 mM rubrene/toluene solution and then transferred to 1 cm by 1 cm path length Starna cuvettes containing 100  $\mu$ m thick borosilicate capillary tubes adhered to the wall. The solution diffused up through the space inside the capillary tube. The final concentration of QD was 10  $\mu$ M. For transient absorption measurements, the pellet was redispersed in toluene and transferred to a 1 mm path length cuvette sealed with a greased Teflon cap and electrical tape. The final concentration of QD was 50  $\mu$ M. All samples were prepared in an argon glovebox.

PbS/CdS: methods and conditions are the same as those for PbS//**5-CT** except that the concentration of **5-CT** in the ligand exchange solution was 300  $\mu$ M, and methanol was used as precipitant rather than acetone.

CdSe/CdS and CdSe/ZnS: 9-ACA transmitter ligands were bound on NCs via ligand exchange in glovebox: NCs and 9-ACA were dissolved in THF resulting in a mixture with total volume of 500  $\mu$ L containing 10  $\mu$ M NCs. The concentration of 9-ACA was varied. The mixture was stirred for 12 h at room temperature. 1 mL acetonitrile as bad solvent was added to the ligand exchange solution to crash out the NC/9-ACA complex by centrifugation at 7830 rpm for 15 min. Then the clear supernatant was discarded. For photon upconversion measurements, the pellet was redispersed in 1 mL of 2.15 mM DPA in hexanes. For lifetime and transient absorption measurements, the pellet was redispersed in hexane. The photon upconversion and lifetime measurements were done with 1x1 cm cuvette, and transient absorption measurements with a 2 mm path length cuvette. All samples were prepared in an argon glovebox.

## 8.6 Quantum yield calculation

### 8.6.1 Absolute Quantum Yield Calculation for CdSe

The upconversion quantum yield ( $\Phi_{uc}$ ) is calculated by equation 8. 1

$$\Phi_{uc} = 2 \times \Phi_{R6G} \times \frac{n_{DPA}^2}{n_{R6G}^2} \times \frac{[Area]_{DPA}}{[Area]_{R6G}} \times \frac{1 - 10^{-A_{R6G}}}{1 - 10^{-A_{CdSe}}} \quad (8. 1)$$

where  $\Phi_{R6G}$  is the quantum yield of R6G,  $n_{DPA}$  and  $n_{R6G}$  represent the refractive indices of the solvents for the DPA upconversion sample and R6G, which are hexane and ethanol, respectively.  $[Area]_{DPA}$  and  $[Area]_{R6G}$  are the integrated areas of the fluorescence peaks of DPA and R6G.  $A_{CdSe}$  and  $A_{R6G}$  stand for the absorbance of CdSe NCs and R6G at 532nm.

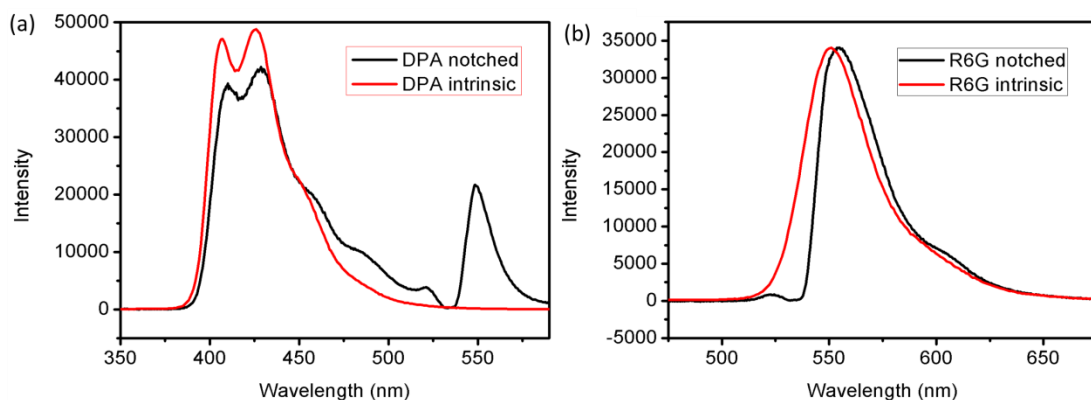


**Figure 8.6.** (a) Intrinsic (red) and detected (black) upconversion fluorescence spectra of DPA. The intrinsic fluorescence spectrum is scaled to match the upconversion spectrum at 450 nm. (b) Intrinsic (red) and detected (black) Rhodamine 6G fluorescence spectra. The intrinsic spectrum of the Rhodamine 6G standard is scaled to match the experimental spectrum at 550 nm.

The detected upconversion fluorescence spectrum of DPA and the fluorescence spectrum of the R6G standard are distorted by the presence of the 532 notch filter that is necessary to block scattered 532 nm laser light. To correct for these distortions, we scale the intrinsic fluorescence spectra so they match the detected spectra at specific wavelengths, as shown in Fig. 8.6. We then use values  $\Phi_{R6G} = 0.95$ ,  $n_{DPA} = 1.375$  and  $n_{R6G} = 1.360$ ,  $[Area]_{DPA} = 51896$  (after dividing by 50 to account for integration time),  $[Area]_{R6G} = 1555077$ ,  $A_{CdSe} = 0.192$  and  $A_{R6G} = 0.312$ . Plugging these values into Equation 8.1 leads to a value of 0.093 for the upconversion quantum yield  $\Phi_{uc}$ . Different spectral scaling methods could change this value, leading to a conservative error range of  $\pm 0.02$ .

### 8.6.2 Quantum Yield Calculation for PbSe (800 nm)

These measurements were done on samples with a PbSe nanoparticle concentration of  $5.5 \times 10^{-5}$  and  $[RUB] = 3.8 \times 10^{-3}$  M. A demountable cell (Pike Technologies 162-1100)



with a pathlength of 100  $\mu\text{m}$  was used in order to make the sample optically thin and ensure a uniform beam intensity. The 800 nm beam was reflected off a dichroic mirror and focused to spot size of  $\sim 150 \mu\text{m}$  diameter. The 800 nm power was adjusted to put the upconverted fluorescence signal well into the linear regime with an intensity of 1000  $\text{W}/\text{cm}^2$ . For the reference sample (RUB in toluene), the sample was excited at 400 nm using the frequency doubled output of a Ti:Sapphire laser. The laser beams were chopped and the output of the photomultiplier tube was detected on a lockin amplifier (SRS 810). Both the RUB and PbSe/RUB fluorescence signals were checked for linearity.

$$\Phi_{UC} = 2\Phi_{ref} \times \frac{(\textit{photons absorbed by reference})}{(\textit{photons absorbed by UC sample})} \times \frac{\textit{signal(UC sample)}}{\textit{signal(reference)}} \quad (8.2)$$

$\Phi_{ref}$  is the quantum yield of RUB and is 0.98. The detected signals were 6.00 mV for a 18  $\mu\text{W}$  of 400 nm laser power, and 2.46 mV for 192.2 mW of 800 nm laser power. Note that we use 1000x more 800 nm laser power. The absorbance of the RUB sample at 400 nm was measured to be 0.0295 using a process of serial dilution. The absorbance of the PbSe sample at 800 nm was measured to be 0.0116. The number of photons absorbed is calculated using the relation

$$\textit{photons absorbed} / s = \frac{\textit{Laser Power}}{hc / \lambda} (1 - 10^{-Abs}) \quad (8.3)$$

$h$  is Planck's constant,  $c$  is the speed of light, and  $Abs$  is the sample absorption. Using Equation 8.3 for  $\lambda=400$  nm and  $\lambda=800$  nm with the given powers and absorbances, we then substitute these values into Equation 8.2 to obtain  $\Phi_{UC} = 9.3 \cdot 10^{-5}$ . By taking possible

errors in laser power, detection, and background into account, we can find a variation of roughly  $0.5 \times 10^{-5}$ , leading to our reported value  $\Phi_{UC} = 1.0 (\pm 0.5) \times 10^{-4}$ .

### 8.6.3 Quantum Yield Estimation for PbSe (980 nm)

The 980 nm output from the fiber laser could not be focused tightly at the same location as the 800 nm beam, so we attenuated the 800 nm laser in order to put both upconversion efficiencies into the quadratic regime. We used a 1 cm cuvette that ensured that 100% of both beams was absorbed in the sample and detected the fluorescence from the front face using a photomultiplier tube. In this regime, the upconverted signal is proportional to the intensity squared multiplied by the laser spot size.

$$\frac{\Phi_{980}}{\Phi_{800}} = \frac{((800 \text{ nm power}) / A_{800})^2}{((980 \text{ nm power}) / A_{980})^2} \times \frac{A_{800}}{A_{980}} \times \frac{\text{signal}(980 \text{ nm})}{\text{signal}(800 \text{ nm})} \quad (8.4)$$

$A_{800}$  is the area of the 800 nm beam, and  $A_{980}$  is the area of the 980 nm beam. We measured the 800 nm power to be 7.19 mW, the 980 nm power to be 79.1 mW, the signal from the 980 nm was 25.4 mV, the signal from the 800 nm was 17.0 mV, the 800 nm beam radius was 0.074 mm, and the 980 nm beam radius was 0.54 mm. The area is proportional to the spot radius squared. Plugging all these values into Equation 8.4 yielded a quantum

yield ratio  $\frac{\Phi_{980}}{\Phi_{800}} = 0.64$ , but we emphasize that there is quite a bit of uncertainty in this

ratio due to the nonuniform excitation intensity as the beams are absorbed in the 1 cm

cuvette, and it could be a factor of 2 higher or lower. A factor of 2 lower leads to  $\frac{\Phi_{980}}{\Phi_{800}} =$

0.32, and so we conservatively estimate that  $\Phi_{980}$  is within a factor of 3 of  $\Phi_{800}$ .

## 8.7 Time-resolved photoluminescence measurement

### 8.7.1 Characterization of delayed fluorescence from PbSe/RUB.

When 800 nm femtosecond pulses excite the PbSe/RUB sample, there are both prompt (ns) and delayed ( $\mu$ s) fluorescence components. The spectra of both components are almost identical, as shown in Fig. 8.7, and correspond to the RUB singlet emission.

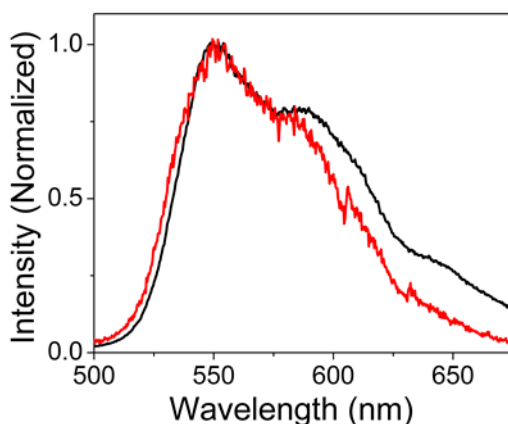


**Figure 8.7.** Comparison of early time (0-100 ns, black) and late time (0.6-390  $\mu$ s, red) fluorescence from the PbSe/RUB sample after excitation with 800 nm laser pulse. The early spectrum reflects prompt fluorescence due to nonresonant two-photon excitation of the RUB, while the delayed fluorescence is due to upconverted signal after TTA by RUB molecules sensitized by PbSe NC's. The slightly different spectral shapes reflect additional self absorption of the prompt (two-photon) fluorescence due to the deeper penetration of the two-photon excitation mode into the sample cuvette.

### 8.7.2 Characterization of quenching of CdSe photoluminescence by 9-ACA ligand.

Lastly, the photoluminescence decay of a CdSe/9-ACA sample was compared to that of a CdSe/ODPA sample (no DPA acceptor in either sample). For the CdSe/9-ACA sample, the 400 nm beam excited a significant amount of free 9-ACA ligands in solution, and the narrow CdSe peak at 570 nm had to be isolated from the 9-ACA emission that stretches from 450 to 550 nm. An example of the spectral data, along with its

decomposition into 9-ACA and CdSe components, is shown in Figure 8.9a. The acceleration of the CdSe component is shown in Figure 8.9b in the 100 ns window.

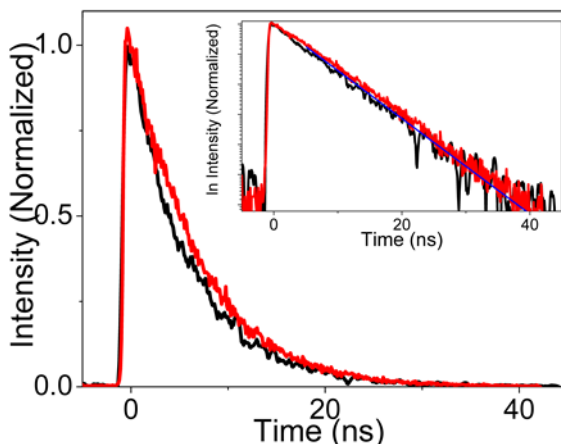


**Figure 8.8.** Comparison of the fluorescence decays of DPA by itself (black) and the CdSe/9-ACA/DPA sample (red). Inset: Logarithmic comparison of the decay. Both are single exponential with a lifetime of  $6.5 \pm 0.1$  ns for the CdSe/9-ACA/DPA sample and  $6.3 \pm 0.1$  ns for the DPA sample.

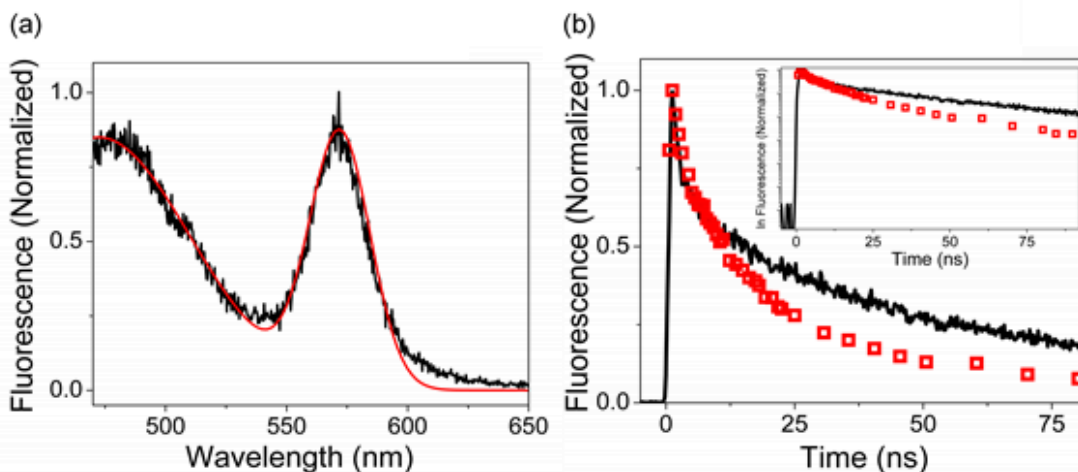


**Figure 8.9.** (a) The CdSe emission peak (centered at 570 nm) with overlapping 9-ACA fluorescence (centered at 490 nm) is fit with a dual Gaussian fit (red line) in the time window 54-75 ns. The amplitude of the Gaussian centered at 570 nm is taken to be the amplitude of the CdSe luminescence in this time window. (b) Decay of the CdSe/ODPA sample (black) and extracted CdSe component from the CdSe/9-ACA sample (red). Inset: Logarithmic comparison of the decays. Both decays are multiexponential, as typically seen

for CdSe NCs, but the CdSe/9-ACA sample diverges from the CdSe/ODPA sample after 10 ns and decays more rapidly.

### 8.7.3 TRPL measurement of CdSe/CdS and CdSe/ZnS core-shell NCs with 9-ACA

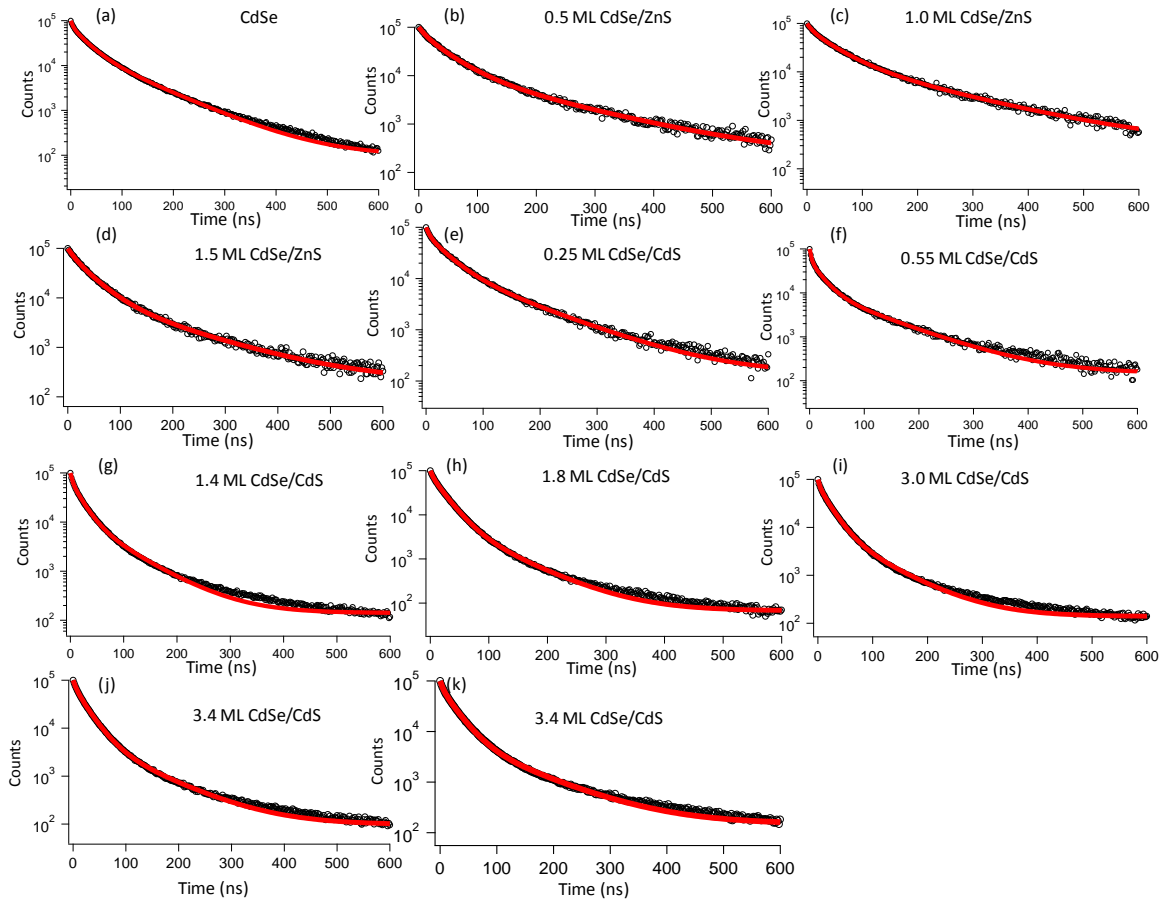


**Figure 8.10.** Photoluminescence decay of (a) 2.9 nm diameter CdSe core, (b-d) CdSe/ZnS and (e-k) CdSe/CdS core-shell NCs of different shell thickness. Samples are dissolved in hexane and excited with a 406 nm pulsed laser. The raw data is shown as black hollow circle, with the red curves the triexponential fits.

The photoluminescence decay of CdSe core and CdSe/CdS, CdSe/ZnS core-shell NCs are fitted with triexponential decay with a y-offset:

$$I(t) = A_0 + A_1 \times e^{-t/\tau_1} + A_2 \times e^{-t/\tau_2} + A_3 \times e^{-t/\tau_3} \quad (8.5)$$

where  $I(t)$  is the photoluminescence intensity at decay time  $t$ ,  $A_1$ ,  $A_2$ ,  $A_3$ , and  $\tau_1$ ,  $\tau_2$ ,  $\tau_3$  are the prefactors and time constants.  $A_0$  is the y-offset. The intensity weighted average lifetime  $\bar{\tau}$  is calculated by:

$$\bar{\tau} = \frac{\sum_i A_i \tau_i^2}{\sum_i A_i \tau_i}. \quad (8.6)$$

With the intensity weighted averaged lifetime  $\bar{\tau}$  and photoluminescence quantum yield  $\Phi_{PL}$ , we are able to calculate the radiative rate constant  $k_r$ , and nonradiative decay rate constant  $k_{nr}$  by:

$$\Phi_{PL} = \frac{k_r}{k_r + k_{nr}} = k_r \bar{\tau} \quad (8.7)$$

**Table 8.1.** Parameters from the triexponential fits of the photoluminescence decay for CdSe core and CdSe/ZnS, CdSe/CdS core-shell nanocrystals.  $n$  is the shell thickness in monolayers (ML);  $A_1$ ,  $A_2$ ,  $A_3$  and  $\tau_1$ ,  $\tau_2$ ,  $\tau_3$  are the amplitudes and time constants,  $A_0$  is the y-offset of the decay.

NC	$n/ML$	$A_0$	$A_1$	$\tau_1/ ns$	$A_2$	$\tau_2/ ns$	$A_3$	$\tau_3/ ns$	$\bar{\tau} / ns$
CdSe	-	9.7E-04	0.229	4.0	0.542	27.8	0.227	88.6	61.05
CdSe/ZnS	0.5	1.9E-03	0.230	10.8	0.627	40.8	0.141	142.9	81.84
	1.0	2.9E-03	0.220	9.1	0.585	44.7	0.192	154.1	99.47
	1.5	2.0E-03	0.217	12.3	0.665	37.5	0.116	130.1	68.74
CdSe/CdS	0.25	1.3E-03	0.269	5.6	0.548	32.0	0.182	103.1	66.21
	0.5	1.5E-03	0.443	2.9	0.442	20.6	0.114	93.3	56.35
	1.4	1.4E-03	0.282	3.3	0.589	19.3	0.127	67.5	38.36
	1.8	6.7E-04	0.187	4.1	0.732	22.3	0.081	70.7	33.78
	3.0	1.4E-03	0.247	3.1	0.658	20.5	0.094	70.0	35.48
	3.4	9.7E-04	0.245	5.7	0.685	23.2	0.070	83.7	37.39
	3.4	1.5E-03	0.236	4.5	0.679	24.4	0.083	93.7	44.74

## 8.8 Transient absorption measurements and analysis for CdSe/An-X

### 8.8.1 Power dependence

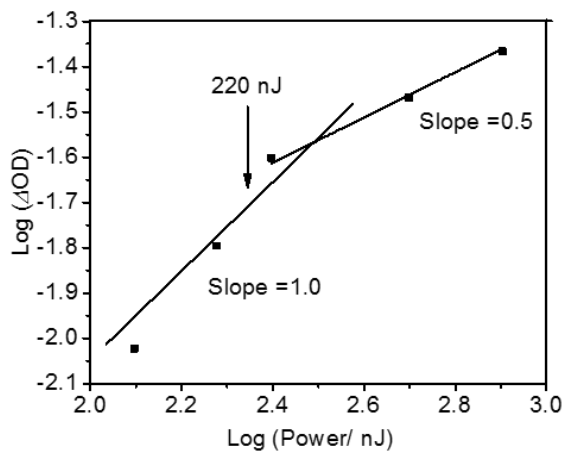


**Figure 8.11.** The absorption intensity of CdSe/ODPA NCs at 463 nm versus the excitation power plotted in log scale obtained from the TA difference spectra. The laser power of 220 nJ was used to excite all samples to avoid exciton-exciton annihilation processes observed at higher powers (slope=0.5). Samples were excited at 505 nm.

## 8.8.2 Transient absorption spectra

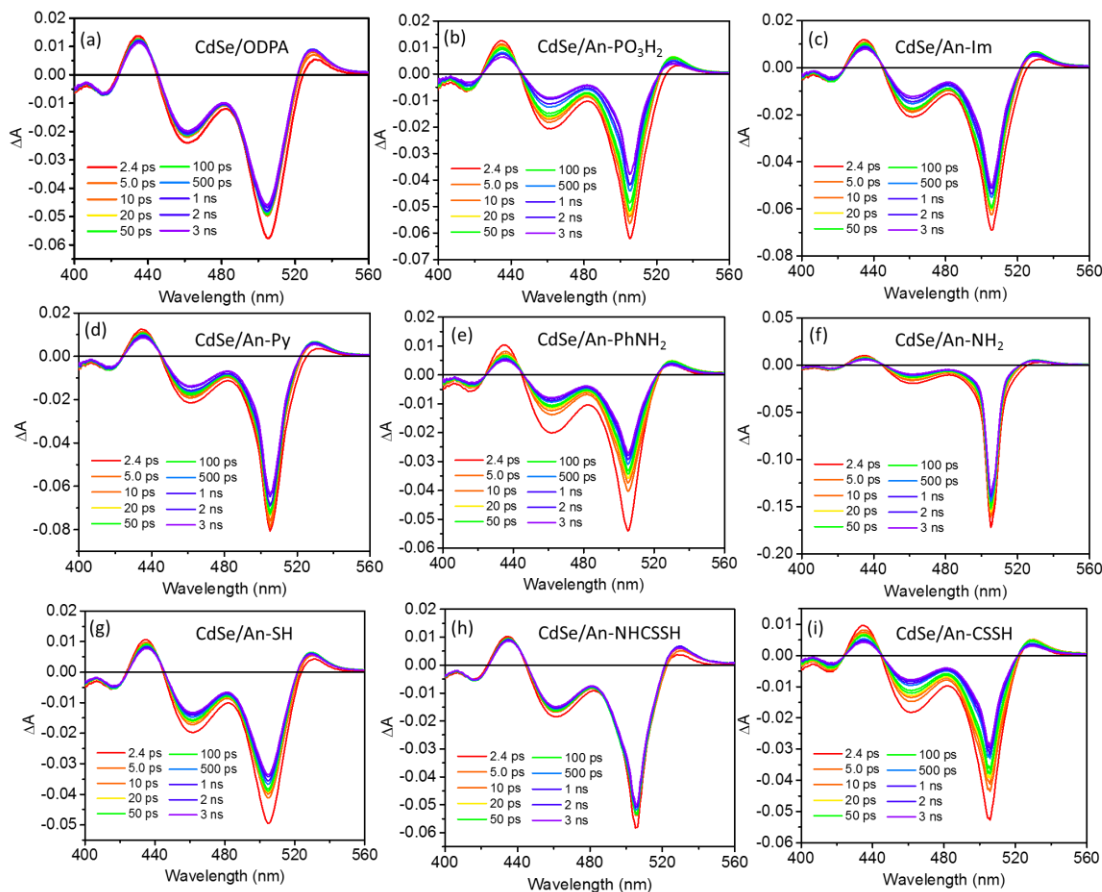


**Figure 8.12.** Picosecond TA difference spectra of CdSe NCs capped with (a) native octadecylphosphonic acid, CdSe/ODPA, (b) 9-anthracenephosphonic acid, CdSe/An-PO<sub>3</sub>H<sub>2</sub>, (c) 9-anthraceneimidazole, CdSe/An-Im, (d) 9-anthracenepyridine, CdSe/An-Py, (e) 9-anthracene-*p*-aniline, CdSe/An-PhNH<sub>2</sub>, (f) 9-anthraceneamine, CdSe/An-NH<sub>2</sub>, (g) 9-anthracenethiol, CdSe/An-SH, (h) 9-anthracenedithiolcarbamate CdSe/An-NHCSSH, and (i) 9-anthracenedithioic acid, CdSe/An-CSSH. Samples were selectively excited with a 505nm pulsed laser.



8.8.3 Analysis of the kinetics of triplet energy transfer (TET), extracting the rate constant,  $k_{TET}$ , and TET efficiency,  $\Phi_{TET}$  for the anthracene transmitters.

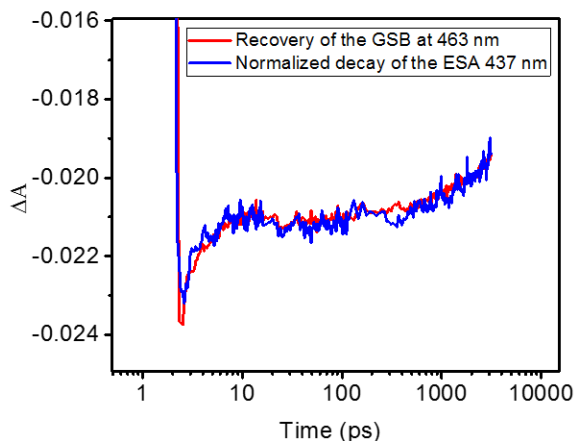


**Figure 8.13.** The recovery of the ground state bleach (GSB) at 463 nm (red) and the normalized decay of the excited state absorption (ESA) at 437 nm (blue) shows the same kinetics for unfunctionalized CdSe/ODPA. These trajectories are extracted from Fig. 8.12a and can be fit with two exponentials.

### 1) Fitting model for the kinetics at 437 nm (ESA) and 463 nm (GSB).

The  $T_1$ - $T_n$  absorption of bound An-COOH on CdSe NCs spans from 400 - 450 nm.<sup>27</sup> Here, we monitor the kinetics of the anthracene triplet state at 437 nm. At this wavelength, the  $T_1$ - $T_n$  transition of bound anthracene ligands overlaps with the excited state absorption (ESA) of CdSe NCs. Here, we extract the kinetics of  $T_1$ - $T_n$  transition of anthracene ligands at 437 nm by the global fitting of the decays at 437 nm (ESA) and 463 nm (GSB) for CdSe/An-X.

For CdSe/An-X, the recovery of the GSB at 463 nm can be fit well with three exponentials, including the two intrinsic time constants observed in CdSe/ODPA NCs, and another exponent due to TET from NC donor to anthracene transmitter. Therefore, we can fit the recovery at 463 nm with:

$$F(t)=A_0*\exp(-(t+t_0)/\tau_0)+A_1*\exp(-(t+t_0)/\tau_1)+A_2*\exp(-(t+t_0)/\tau_2) \quad (8.8)$$

where  $A_0, A_1, \tau_0, \tau_1$  are the amplitudes and time constants from the intrinsic decays of CdSe NCs; and  $A_2, \tau_2$  are the amplitude and time constant stemming from TET.  $t_0$  is the correction for time zero from the TA measurement, which is 2.2 ps.

For CdSe/An-X, the decay of the ESA at 437 nm includes the same three decay channels and a rise channel. The rise channel is from the growth of the  $T_1-T_n$  transition of the anthracene ligands due to TET from NC to transmitter. The three decay channels should have the same time constants and amplitudes proportional to that extracted from the GSB at 463 nm. This is confirmed by the overlapping ESA and GSB for CdSe/ODPA as shown in Fig. 8.13 (Here the amplitude of the ESA has been normalized to match the GSB).

Therefore, the decay at 437 nm can be fit with:

$$F(t)=m*(-A_0)*\exp(-(t+t_0)/\tau_0)+m*(-A_1)*\exp(-(t+t_0)/\tau_1)+m*(-A_2)*\exp(-(t+t_0)/\tau_2)+A*\exp(-(t+t_0)/\tau_2)-A \quad (8.9)$$

where  $A_0, A_1, A_2, \tau_0, \tau_1, \tau_2$ , are the amplitudes and time constants corresponding to the three decay channels of GSB at 463 nm in Eq. (8.8),  $m$  is the proportionality constant between GSB and ESA,  $A$  is the amplitude, i.e. the maximum OD for the  $T_1-T_n$  transition of anthracene ligands.

Global fittings of the GSB and ESA are performed with the linked parameters of  $t_0, A_0, A_1, A_2, \tau_0, \tau_1, \tau_2$ . The fitting results and parameters are shown in Fig. 8.14 and Table 8.2.

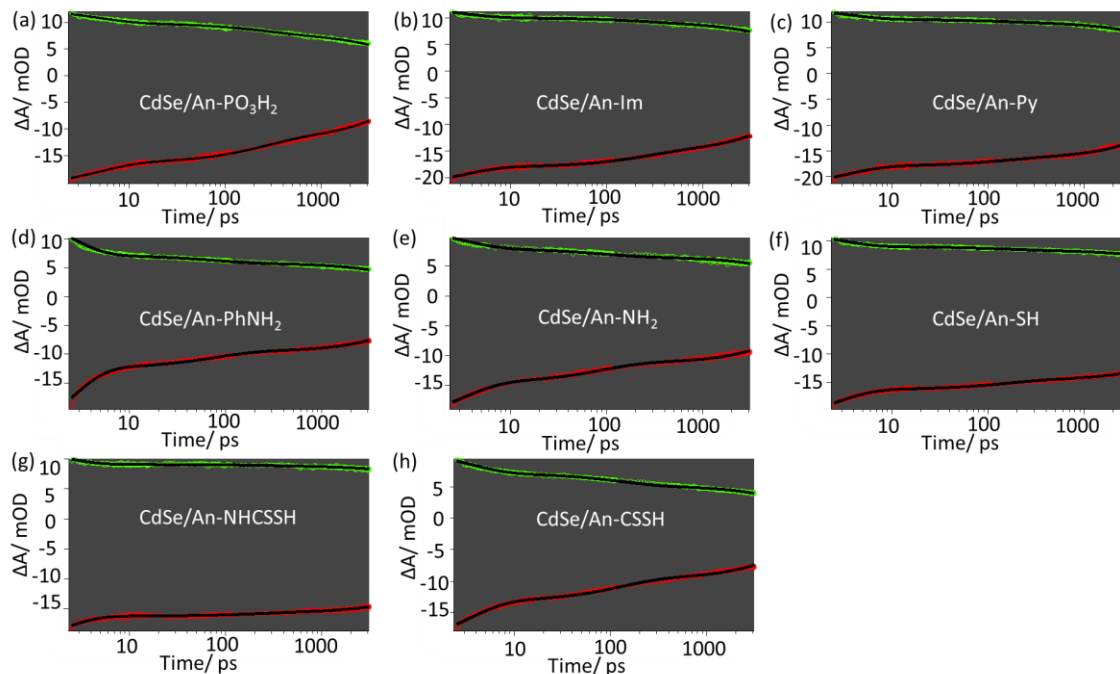


**Figure 8.14.** Global fitting (black) of the decay of the ESA at 437 nm (green) and recovery of the GSB at 463 nm (red) for CdSe NCs capped with (a) 9-anthracenephosphonic acid, CdSe/An-PO<sub>3</sub>H<sub>2</sub>, (b) 9-anthraceneimidazole, CdSe/An-Im, (c) 9-anthracenepyridine, CdSe/An-Py, (d) 9-anthracene-*p*-aniline, CdSe/An-PhNH<sub>2</sub>, (e) 9-anthraceneamine, CdSe/An-NH<sub>2</sub>, (f) 9-anthracenethiol, CdSe/An-SH, (g) 9-anthracenedithiolcarbamate CdSe/An-NHCSSH, and (h) 9-anthracenedithioic acid, CdSe/An-CSSH, based on Eq. 8.8 and Eq. 8.9. The measurements were performed in hexane at room temperature, with the excitation of 505 nm pulsed laser.

**Table 8.2:** Parameters from the global fits of the decay of the ESA at 437 nm (green) and rise of the GSB at 463 nm (red) for CdSe NCs capped with different anthracene ligands in Figure 8.14, based on Eq. 8.8 and Eq. 8.9.  $t_0$  is the correction for time zero.  $A_0$ ,  $A_1$ ,  $\tau_0$ ,  $\tau_1$  are the amplitudes and time constants of the intrinsic decays of CdSe NCs at 463 nm (from the GSB),  $A_2$ ,  $\tau_2$  are the amplitude and time constant for the decay due to TET at 463 nm (from the GSB).  $A$  is the amplitude of the rise of  $T_1$ - $T_n$  transition of anthracene ligands at 437 nm (ESA).  $m$  is the proportionality constant between ESA and GSB.  $k_{TET}$  is the TET rate constant.  $\Phi_{TET}$  is the TET efficiency. All the amplitudes are normalized by the concentration of CdSe NCs for different samples.

	An-PO <sub>3</sub> H <sub>2</sub>	An-Im	An-Py	An-PhNH <sub>2</sub>	An-NH <sub>2</sub>	An-SH	An-NHCSSH	An-CSSH
$t_0/\text{ps}$	2.2	2.2	2.2	2.2	2.2	2.2	2.2	2.2
$A_0$	-0.01013	-0.0109	-0.00984	-0.05982	-0.0101	-0.0101	-0.01739	-0.01828
$\tau_0/\text{ps}$	4.68	2.89	3.11	1.94	2.92	2.36	1.6	3.03
$A_1$	-0.01575	-0.01747	-0.01695	-0.00966	-0.00696	-0.00844	-0.00921	-0.01026
$\tau_1/\text{ps}$	8774.7	13201	14036	13074	14935	27644	45840	11666
$A_2$	-0.00564	-0.00317	-0.0015	-0.00293	-0.00209	-0.00096	-0.00033	-0.00381
$\tau_2/\text{ps}$	234.7	240.1	132.1	75.3	87.7	150.5	213	123
$m$	0.601	0.553	0.582	0.575	0.544	0.551	0.559	0.54
$A$	-0.000903	-0.000820	-0.000346	-0.000267	-0.000271	-0.000163	-0.000068	0.000074
$k_{TET}/\text{S}^{-1}$	4.26E+09	4.16E+09	7.57E+09	1.33E+10	1.14E+10	6.64E+09	4.69E+09	0
$\Phi_{TET}/\%$	12.34	11.20	4.73	3.65	3.70	2.23	0.93	0

2) Triplet energy transfer rate constant  $k_{TET}$ , and efficiency  $\Phi_{TET}$ .

Triplet energy transfer rate constants,  $k_{TET}$ , and efficiencies,  $\Phi_{TET}$ , for each transmitter ligand are listed in Table 8.2.  $k_{TET}$  is calculated based on the TET time constant  $\tau_2$  in Table 8.2. As with the efficiency, based on previous work,<sup>27</sup>  $\Phi_{TET}$  is defined as the concentration of triplet state of ligand [<sup>3</sup>An-X\*] over the concentration of the photoexcited exciton in CdSe NCs [CdSe\*]:

$$\phi_{TET} = \frac{[{}^3An-X^*]}{[CdSe^*]} = \frac{\Delta A({}^3An-x^*) / \varepsilon({}^3An-x^*)}{\Delta A(CdSe^*) / \varepsilon(CdSe)} \quad (8.10)$$

where  $\Delta A({}^3An-X^*)$  is the maximum  $\Delta A$  of the  $T_1-T_n$  transition, which is  $A$  in Table 8.2,  $\Delta A(CdSe^*)$  is the minimum  $\Delta A$  of the initial amplitude of CdSe/ODPA at 463 nm. The extinction coefficients are obtained based on the literature values ( $\mathcal{E}=10200 \text{ M}^{-1}\text{cm}^{-1}$  for  $T_1-T_n$  transition of An-COOH at 430 nm, and  $\mathcal{E}=37586.7 \text{ M}^{-1}\text{cm}^{-1}$  for  $S_0-S_1$  transition of CdSe NCs at 463 nm).<sup>27,212</sup> Here we assume that An-COOH and all other anthracene ligands have similar extinction coefficients for the  $T_1-T_n$  transition at 437 nm. Results are listed in Table 7.2 and Table 8.2. As summarized in Fig. 7.3a, ligands with high upconversion QYs show high TET efficiencies. This strong correlation between upconversion QY and  $\Phi_{TET}$  is expected because the upconversion QYs is the convolution of  $\Phi_{TET}$  and the efficiencies of singlet emission and triplet-triplet annihilation of DPA, which are constants in our upconversion experiments, i.e.  $\Phi_{UC} = \Phi_{TET} \times \Phi_{TTA(DPA)} \times \Phi_{F(DPA)}$ .

**8.8.4** Normalizing the initial amplitude of the CdSe NC's exciton bleach at 463 nm by the absorption of the excitation wavelength

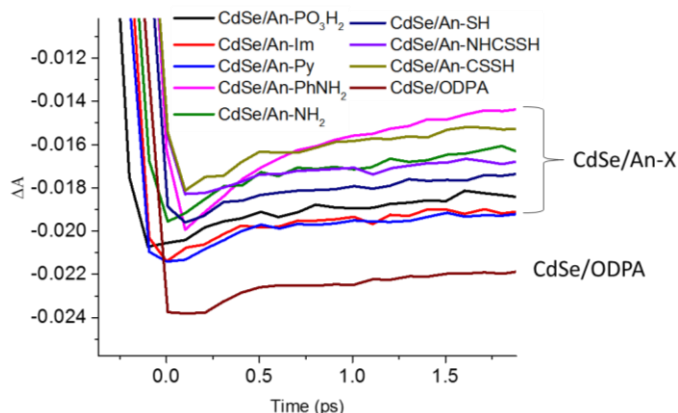


**Figure 8.15.** The initial ground state bleach at 463 nm corresponding to CdSe/ODPA, and CdSe NCs capped with different anthracene ligands. Measurements were performed in hexane at room temperature with the excitation of a 505 nm pulsed laser. All the data has been normalized by the O.D. at 505 nm in the steady state absorption spectra.

**8.9 Transient absorption for CdSe/ZnS//9-ACA and CdSe/CdS//9-ACA**

8.9.1 Power dependence

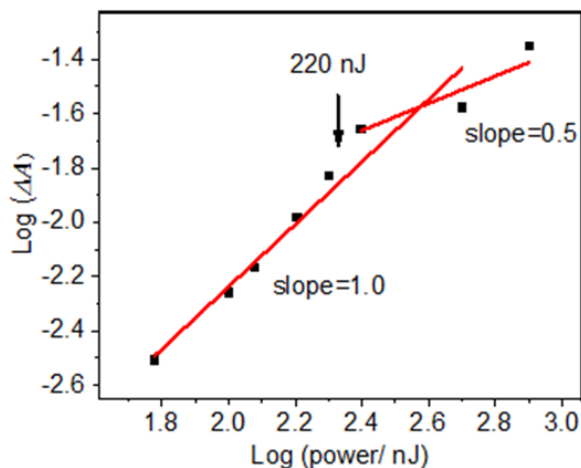


**Figure 8.16.** The absorption intensity of CdSe NCs at 441 nm at 3 ps versus the excitation power plotted in log scale obtained from the TA difference spectra. The laser power of 220 nJ was used to excite all samples to avoid exciton-exciton annihilation processes observed at higher powers (slope=0.5). Samples were dissolved in hexane and excited with a 540 nm pulsed laser at room temperature.

8.9.2 Analysis of the kinetics of triplet energy transfer (TET), extracting the rate constant,  $k_{TET}$ , and TET efficiency,  $\Phi_{TET}$ .

1) Triplet energy transfer from 0.5 ML CdSe/CdS NCs to 9-ACA

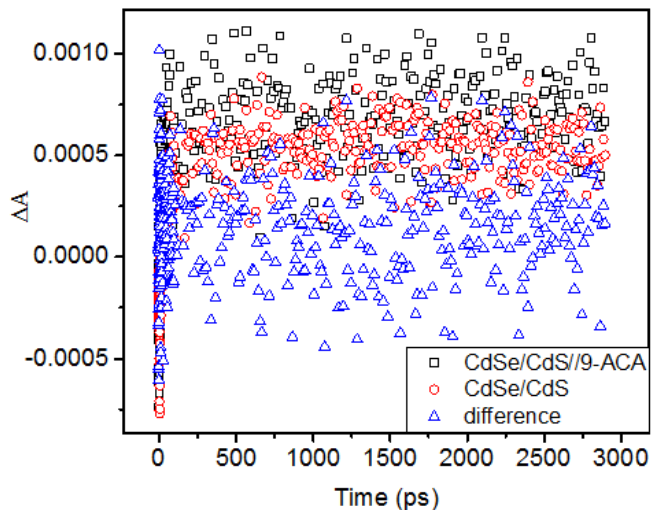


**Figure 8.17.** Kinetic traces at 433 nm for 0.5 ML CdSe/CdS with (black hollow square) and without (red hollow circle) surface bound 9-ACA. The subtraction of the decay for CdSe/CdS only (as background signal) from CdSe/CdS//9-ACA yields the 9-ACA triplet (blue hollow triangle).

The  $T_1$ - $T_n$  absorption of bound 9-ACA on CdSe NCs centers at 433 nm.<sup>27</sup> Therefore, we monitor the kinetics of the 9-ACA triplet state at 433 nm. The TA spectrum of 0.5 ML CdSe/CdS shows an isobestic point at 433 nm where the  $\Delta A$  is zero. So, the  $\Delta A$  at 433 nm for CdSe/CdS//9-ACA is from the 9-ACA  $T_1$ - $T_n$  transition only, without the contribution of NCs. As shown in Fig. 8.17, the subtraction of the kinetic trace at 433 nm for CdSe/CdS NC (as background signal) from that for CdSe/CdS//9-ACA complex yields the signal for the 9-ACA triplet. However, fitting the blue curve with a single exponential function for a rise component doesn't converge, which indicates there is barely any 9-ACA triplet present. Therefore we conclude TET from 0.5 ML CdSe/CdS to 9-ACA is not observed.

2) Triplet energy transfer from CdSe core and 0.5 ML CdSe/ZnS core-shell NCs to 9-ACA

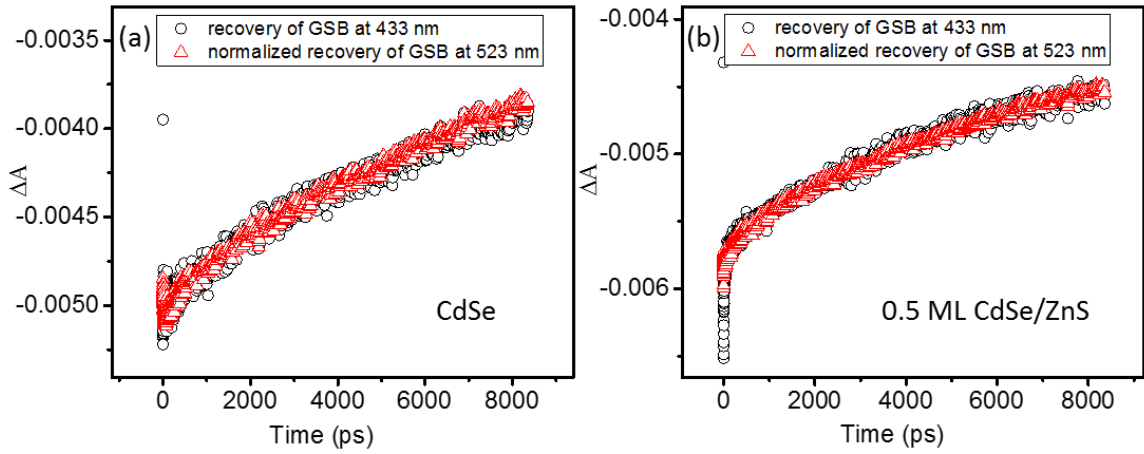


**Figure 8.18.** The recovery of the ground state bleach (GSB) at 433 nm (black hollow circle, averaged over 430-435 nm) and the normalized GSB at 523 nm (red hollow triangle, averaged over 520-525 nm) show the same kinetics for CdSe core (a) and CdSe/ZnS core shell NCs (b). The normalization was performed based on the O.D. at 433 nm at 100 ps.

For CdSe/9-ACA and 0.5 ML CdSe/ZnSA, at 433 nm the absorption of 9-ACA triplet overlaps with the GSB of NCs. Therefore, the isolation of the kinetics of 9-ACA triplet needs to be performed in order to calculate  $k_{TET}$  and  $\Phi_{TET}$ . As shown in Fig. 8.18, for both CdSe and 0.5 ML CdSe/ZnS NCs, the recovery of GSB at 433 nm show the same kinetics as the normalized GSB recovery at 523 nm. This means for CdSe/9-ACA and 0.5 ML CdSe/ZnS/9-ACA, at 433 nm the contribution from the GSB of NCs can be obtained by scaling the recovery of GSB at 523 nm. Therefore, the kinetics of the 9-ACA triplet can be isolated by the global fitting of the kinetics at 433 nm and 523 nm.

For CdSe/An-X, the recovery of the GSB at 523 nm can be fit well with three exponentials, including the two intrinsic time constants from NCs, and another exponent due to TET from NC to 9-ACA. Therefore, we can fit the recovery at 463 nm with:

$$F(t)=A_0*\exp(-(t+t_0)/\tau_0)+A_1*\exp(-(t+t_0)/\tau_1)+A_2*\exp(-(t+t_0)/\tau_2) \quad (8.11)$$



where  $A_0$ ,  $A_1$ ,  $\tau_0$ ,  $\tau_1$  are the amplitudes and time constants from the intrinsic decays of CdSe NCs; and  $A_2$ ,  $\tau_2$  are the amplitude and time constant stemming from TET.  $t_0$  is the correction for time zero from the TA measurement, which is 0.2 ps.

For CdSe//9-ACA and 0.5 ML CdSe/ZnS//9-ACA, the kinetic trace at 433 nm includes the three recovery channels from due to the GSB of NCs, and a rise channel due to the growth of the 9-ACA triplet. Based on Fig. 8.18, three channels from NCs at 433 nm should have the same time constants and amplitudes proportional to that extracted from the GSB at 523 nm in Eq. 8.11. Therefore, the decay at 433 nm can be fit with:

$$F(t) = m * (-A_0) * \exp(-(t+t_0)/\tau_0) + m * (-A_1) * \exp(-(t+t_0)/\tau_1) + m * (-A_2) * \exp(-(t+t_0)/\tau_2) + A * \exp(-(t+t_0)/\tau_2) - A \quad (8.12)$$

where  $A_0$ ,  $A_1$ ,  $A_2$ ,  $\tau_0$ ,  $\tau_1$ ,  $\tau_2$ , are the amplitudes and time constants corresponding to the three decay channels of GSB at 523 nm in Eq. 8.11,  $m$  is the proportionality constant between GSB at 433 nm and 523 nm,  $A$  is the amplitude, i.e. the maximum OD for the  $T_1$ - $T_n$  transition of 9-ACA.

Global fittings of the GSB and ESA are performed with the linked parameters of  $t_0$ ,  $A_0$ ,  $A_1$ ,  $A_2$ ,  $\tau_0$ ,  $\tau_1$ ,  $\tau_2$ . The fitting results and parameters are shown in Fig. 8.19 and Table 8.3.

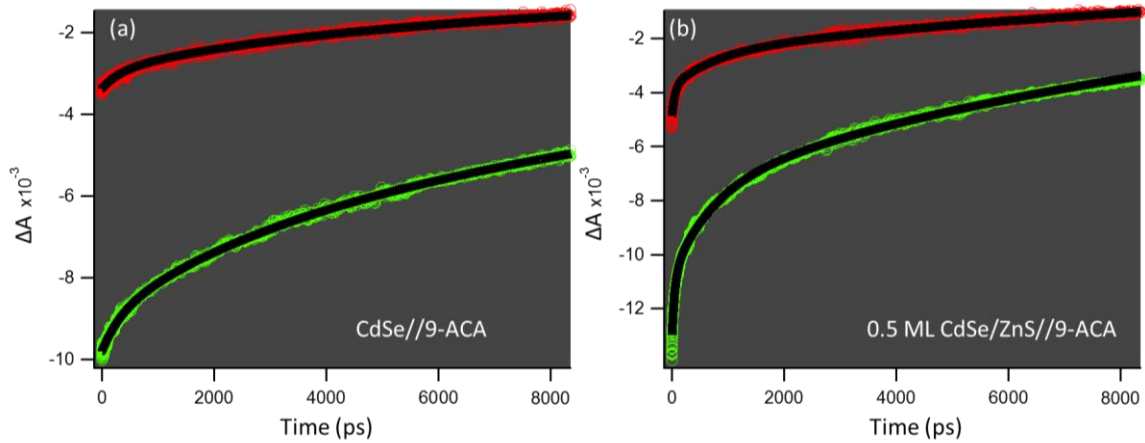


**Figure 8.19.** Global fitting (black) of the decay of the ESA at 433 nm (red) and 523 nm (green) for CdSe//9-ACA (a) and 0.5 ML CdSe/ZnS//9-ACA (b) based on Eq. 8.11 and Eq. 8.12. The measurements were performed in hexane at room temperature, with the excitation of 540 nm pulsed laser.

3) Triplet energy transfer rate constant  $k_{TET}$ , and efficiency  $\Phi_{TET}$  from CdSe and 0.5 ML CdSe/ZnS to 9-ACA

Triplet energy transfer rate constants,  $k_{TET}$ , and efficiencies,  $\Phi_{TET}$ , are listed in Table 8.3.  $k_{TET}$  is calculated based on the TET time constant  $\tau_2$  in Table 8.3. As with the efficiency, based on previous work,<sup>27</sup>  $\Phi_{TET}$  is defined as the concentration of triplet state of 9-ACA [ $^39\text{-ACA}^*$ ] over the concentration of the photoexcited exciton in NCs [ $\text{NC}^*$ ]:

$$\phi_{TET} = \frac{[{}^39\text{-ACA}^*]}{[\text{NC}^*]} = \frac{\Delta A({}^39\text{-ACA}^*) / \varepsilon({}^39\text{-ACA}^*)}{\Delta A(\text{NC}^*) / \varepsilon(\text{NC})} \quad (8.13)$$

where  $\Delta A({}^39\text{-ACA}^*)$  is the maximum  $\Delta A$  of the  $T_1\text{-}T_n$  transition, which is  $A$  in Table 8.3,  $\Delta A(\text{NC}^*)$  is the minimum  $\Delta A$  of the initial amplitude of NC at 523 nm. The extinction coefficients are obtained based on the literature values ( $\varepsilon=10200 \text{ M}^{-1}\text{cm}^{-1}$  for  $T_1\text{-}T_n$  transition of An-COOH at 430 nm, and  $\varepsilon=5.96\text{E}4 \text{ M}^{-1}\text{cm}^{-1}$  and  $7.42\text{E}4 \text{ M}^{-1}\text{cm}^{-1}$  for  $S_0\text{-}S_1$  transition of CdSe and 0.5 ML CdSe/ZnS NCs at 523 nm respectively.  $\varepsilon$  of 0.5 ML

CdSe/ZnS core-shell NCs at absorption maxima was referred to the value of CdSe core).<sup>27,212</sup>

**Table 8.3:** Parameters from the global fits of the kinetics at 433 nm (green) and 523 nm (red) for CdSe//9-ACA and 0.5 ML CdSe/ZnS//9-ACA.  $t_0$  is the correction for time zero.  $A_0$ ,  $A_1$ ,  $\tau_0$ ,  $\tau_1$  are the amplitudes and time constants of the intrinsic decays of NCs at 523 nm (from the GSB),  $A_2$ ,  $\tau_2$  are the amplitude and time constant for the decay due to TET at 523 nm (from the GSB).  $A$  is the amplitude of the rise of  $T_1$ - $T_n$  transition of 9-ACA at 433 nm.  $m$  is the proportionality constant between GSB of NCs at 433 nm and 523 nm.  $k_{TET}$  is the TET rate constant.  $\Phi_{TET}$  is the TET efficiency. All the amplitudes are normalized by the concentration of CdSe NCs for different samples.

	<b>CdSe/9-ACA</b>	<b>CdSe/ZnS//9-ACA</b>
$t_0/\text{ps}$	0.2	0.2
$A_0$	-0.006977	-0.0075515
$\tau_0/\text{ps}$	23232	10413
$A_1$	-0.0020403	-0.0032165
$\tau_1/\text{ps}$	2729.8	739.68
$A_2$	-0.00078849	-0.0022662
$\tau_2/\text{ps}$	324.95	52.966
$m$	0.34381	0.37604
$A$	-0.00012763	-0.00024527
$k_{TET}/\text{S}^{-1}$	3.08E9	1.89E10
$\Phi_{TET}/\%$	6.28	10.3

## 8.10 Transient absorption of PbS/5-CT and PbS/CdS/5-CT

### 8.10.1 Transient absorption spectra of 5-carboxylic acid tetracene (5-CT)

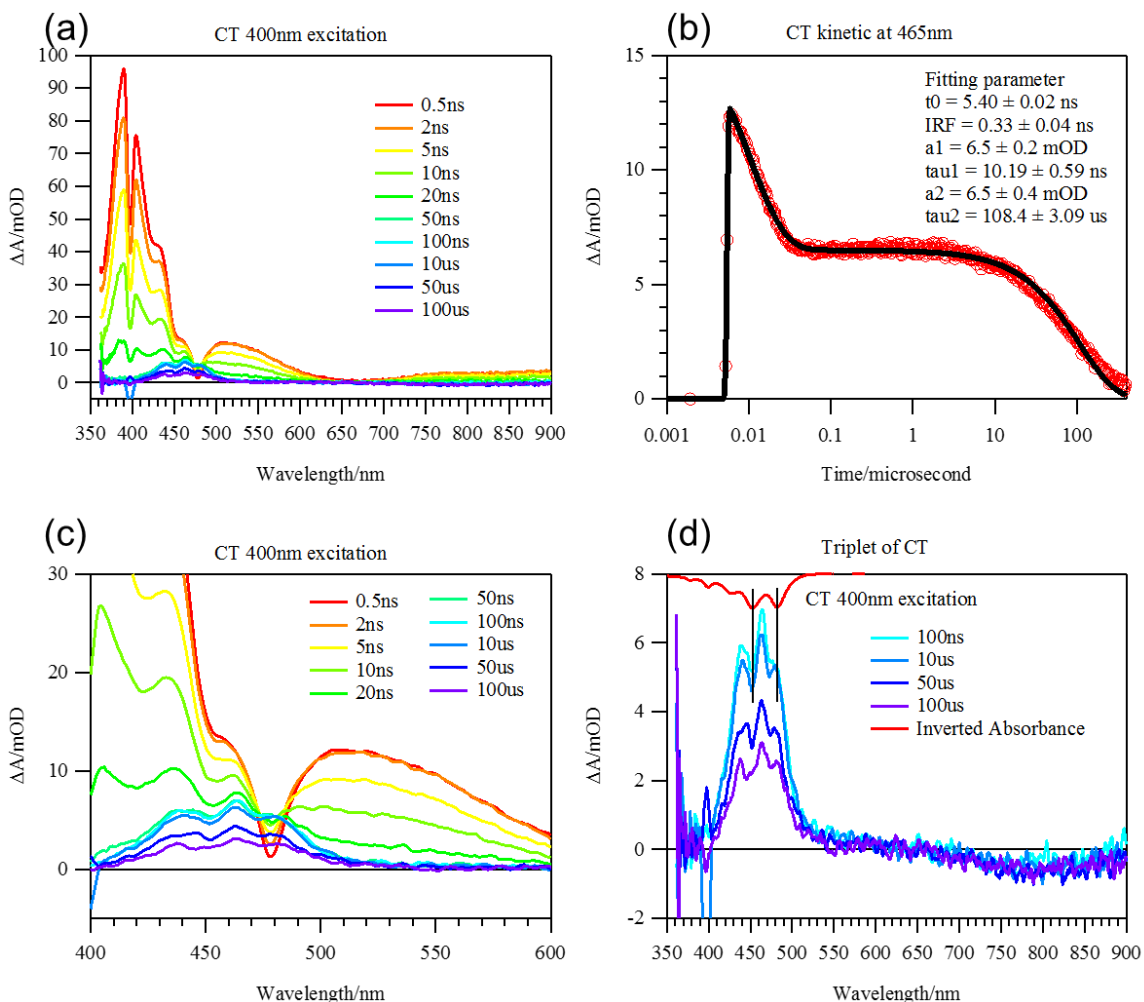


**Figure 8.20.** TA spectra and kinetics of 5-carboxylic acid tetracene (**5-CT**) in solution. (a) Nanosecond transient absorption spectra of **5-CT** in tetrahydrofuran at room temperature measured with 400 nm excitation. (b) Transient kinetics of **5-CT** probed at 465 nm (open symbols) and biexponential fit (solid line), yielding a singlet lifetime of 10.19 ns and triplet lifetime of 108.4  $\mu$ s (c) and (d) provide an expanded view of triplet excited state absorption of **5-CT**.

### 8.10.2 Spectrum fit for relative population

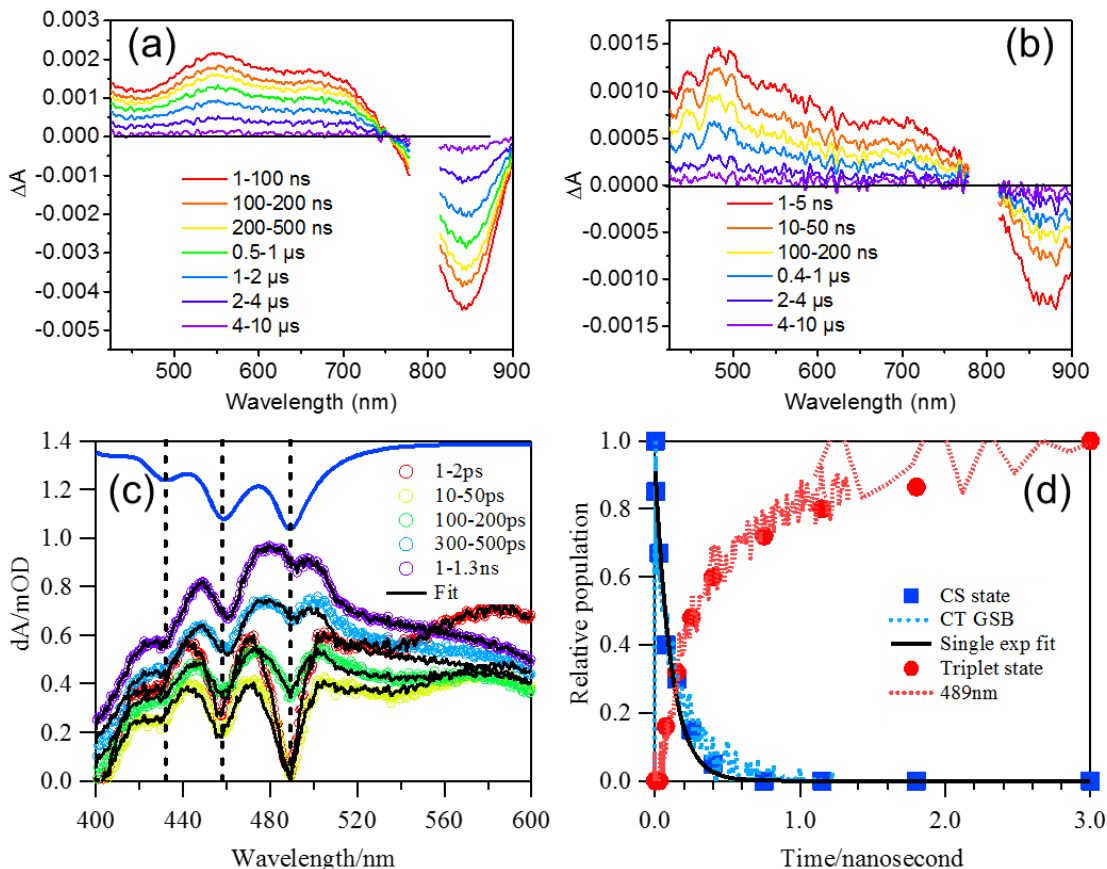


**Figure 8.21.** Nanosecond TA spectra of **5-CT** in a) PbS//OA and b) PbS//**5-CT**. (c) Double difference spectra of PbS//**5-CT** obtained by subtracting the PbS/OA TA signal from the TA signal of PbS//**5-CT**. Also shown for comparison is the static absorption spectra of **5-CT** on PbS QD (blue line, inverted). Vertical lines indicate the position of the ground state bleach. (d) Relative population of the charge separated state (blue square) and **5-CT** triplet excited state (red dot) in PbS//**5-CT**. These populations were obtained by fitting double difference spectra to a model that accounts for both charge separated state and triplet state (see below for details). The black solid line represents a single exponential fit of the decay of the charge separated state. The dashed blue line represented the kinetics of **5-CT** ground state bleach extracted directly from the double difference spectra of PbS//**5-CT**. The red dashed line is the 489 nm kinetics obtained from double difference TA spectrum in (c).

The double difference TA spectrum is dominated by the triplet excited state centered at 463 nm at long delay times. The spectra at early delay time can be attributed to oxidized **5-CT** generated by hole transfer from the QD. The difference spectra at other

delay times can be well fit to a sum of these two species (Fig. 8.21c). The relative populations of these species are plotted in Fig. 8.21d. The decay constant of the charge separated state ( $k_{CS}=8.94\pm 0.98\text{ns}^{-1}$ ) does not agree with the growth of the triplet excited state ( $k_{ET}=3.35\pm 0.06\text{ns}^{-1}$ ), suggesting that the decay of charge separated state does not lead to the formation of the triplet state. Because of negligible TA signals of the CS separated state at 489 nm, the kinetics at this wavelength agrees well with the formation kinetics of triplet (Fig. 8.21d) obtained from spectral fitting and can be used to represent the kinetics of triplet state (see Fig. 5.4).

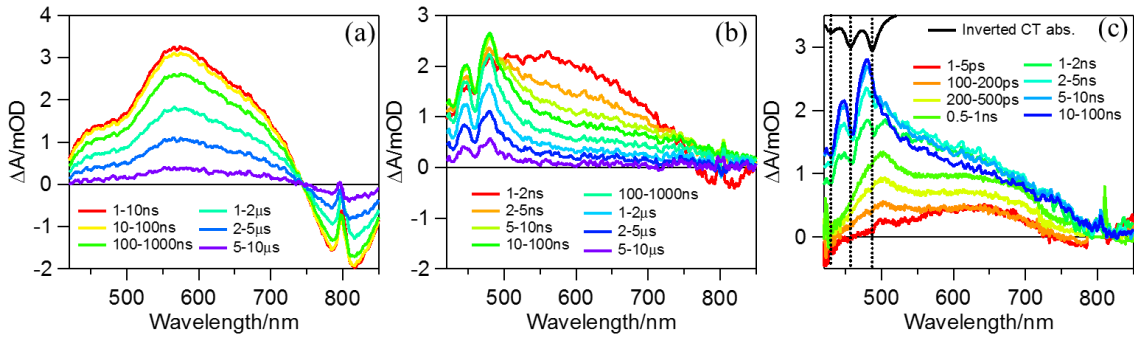


**Figure 8.22.** Comparison of microsecond time range TA spectra of (a) PbS/CdS//OA and (b) PbS/CdS //5-CT. (c) Double difference TA spectrum of PbS/CdS //5-CT.

Fig. 8.22 shows the time evolution of the double difference TA spectra of PbS/CdS//5-CT. Unlike the spectra of PbS//5-CT, the early time spectrum (1-5 ps) shows no ground bleach of 5-CT, suggesting that hot hole transfer is suppressed by the CdS shell.

### 8.10.3 Fitting model for transient kinetics.

The intrinsic decay of free quantum dots can be well fit by three decays, with amplitudes and time constants of  $a_i$  and  $k_i$  ( $i=1-3$ ), respectively.

$$[QD^*](t) = [QD^*](0) \sum_{i=1}^3 a_i e^{-k_i t} \quad (8.14)$$

In QD//**5-CT** complexes, due to triplet energy transfer (with rate constant  $k_{ET}$ ) to **5-CT**, the decay kinetics of the QD becomes:

$$[QD^*//CT](t) = [QD^*//CT](0) \sum_{i=1}^3 A a_i e^{-(k_i + k_{ET})t} \quad (8.15)$$

In Eq. 8.15, the coefficient  $A$  represents the percentage of QDs excitons that undergo triplet energy transfer to **5-CT**. The remaining portion  $(1-A)$  accounts for the initial fast charge transfer pathway observed in PbS//**5-CT**.

The kinetics of the formation and decay of the **5-CT** triplet excited state is given by:

$$[QD//CT^*](t) = \sum_{i=1}^3 \frac{\varepsilon A a_i [QD^*//CT](0) k_{ET}}{k_{ET} + k_i - k_T} [e^{-k_T t} - e^{-(k_{ET} + k_i)t}] \quad (8.16)$$

In Eq. 8.16,  $k_T$  is the decay of rate constant of triplet excited state.

In Fig. 5.4, the exciton bleach kinetics represent the QD excited state, and the **5-CT** triplet excited state is represented by the amplitude of triplet ESA peak at 489 nm of the double difference spectra.  $\varepsilon$  accounts for the ratio of extinction coefficients between these wavelengths. The fitting results are shown as black lines in Fig. 5.4 and the fitting parameters are listed in Table 8.4.

The TET efficiency is given by:

$$\sum_{i=1}^3 \frac{A a_i k_{ET}}{k_{ET} + k_i} \quad (8.17)$$

The calculated efficiencies are shown in Table 8.5.

#### 8.10.4 Fitting parameters

**Table 8.4.** Parameters obtained from fitting kinetics traces displayed in Fig. 5.4

	<b>PbS//5-CT</b>	<b>PbS/CdS//5-CT</b>
[QD] (0)	-5.62±0.03mOD	-3.35±0.03mOD
$a_1$	18.5±0.5%	23.9±0.9%
$a_2$	19.9±0.43%	9.0±0.3%
$a_3$	61.6±3.9%	67.2±0.1%
$k_1$	0.146±0.009ps <sup>-1</sup>	0.161±0.02ps <sup>-1</sup>
$k_2$	48.4±3.0μs <sup>-1</sup>	0.44±0.07ns <sup>-1</sup>
$k_3$	0.525±0.018μs <sup>-1</sup>	0.26±0.00μs <sup>-1</sup>
$A$	0.712±0.011	0.995±0.006
$k_{ET}$	3.35±0.06ns <sup>-1</sup>	0.934±0.020ns <sup>-1</sup>
$k_{CS}$	8.94±0.98ns <sup>-1</sup>	-
$k_T$	1.01±0.07μs <sup>-1</sup>	0.318±0.017μs <sup>-1</sup>
$\varepsilon$	-0.311±0.004	-0.811±0.008
IRF	0.293±0.009ps <sup>-1</sup>	0.293±0.009ps <sup>-1</sup>
$t_0$	0.301±0.003ps <sup>-1</sup>	0.301±0.003ps <sup>-1</sup>
Triplet	1.02mOD	1.99mOD
TET%	58.1%	73.1%

**Table 8.5.** Component corresponded TET efficiency

<b>PbSCT</b>			<b>PbSCdS CT</b>		
Component	Percent	TET/%	Component	Percent	TET/%
$a_1$	18.5±0.5%	2.24	$a_1$	23.9±0.9%	0.58
$a_2$	19.9±0.43%	98.6	$a_2$	9.0±0.3%	68.0



$a_3$        $61.6 \pm 3.9\%$       100      |       $a_3$        $67.2 \pm 0.1\%$       100

### 8.11 Phosphorescence spectra of anthracene ligands with different functional groups

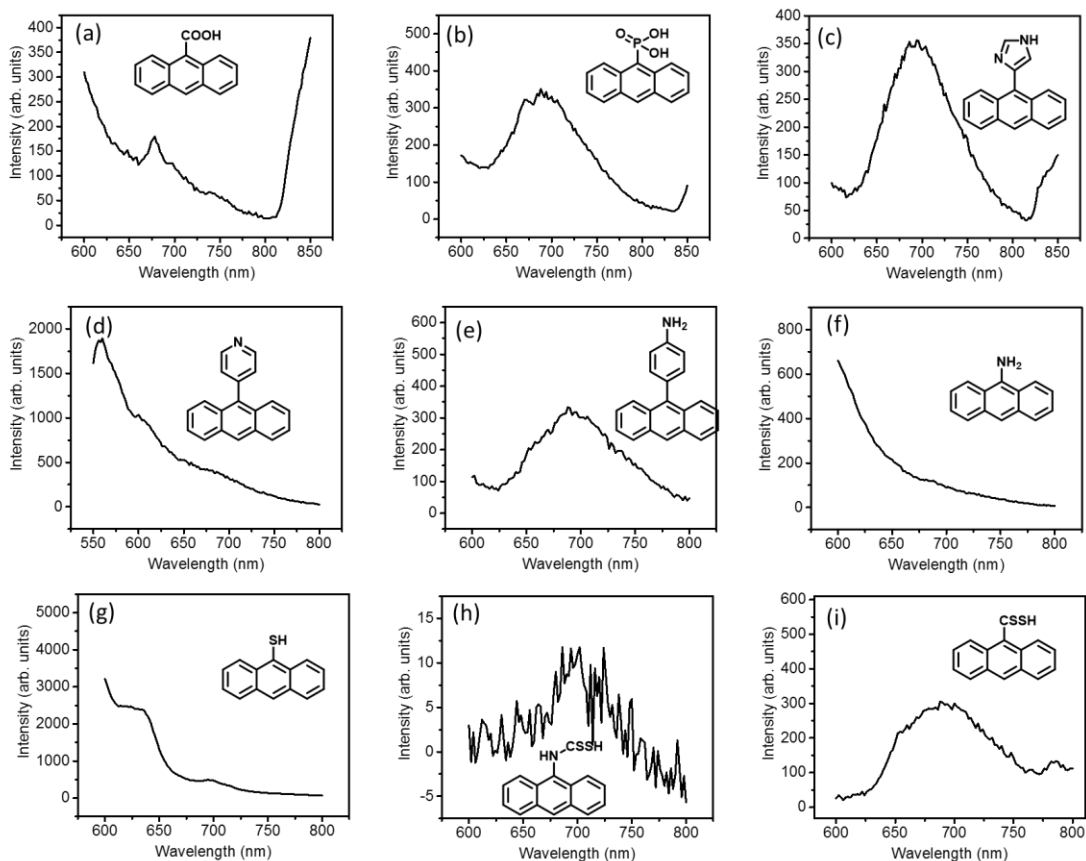


**Figure 8.23.** Phosphorescence spectra of anthracene ligands measured in a glass of 2-methyltetrahydrofuran at 77K.

### 8.12 Cyclic voltammetry (CV) measurements of the highest occupied molecular orbital (HOMO) and lowest unoccupied molecular orbital (LUMO) of NCs and ligands

Cyclic voltammetry measurements were conducted on a Gamry interface 1000 electrochemical analyzer with a three-electrode system in an argon glove box in an anhydrous dichloromethane (DCM) solution containing tetra-*n*-butylammonium hexafluorophosphate (0.1 M) as electrolyte. A glassy carbon electrode was used as a working electrode, a platinum-wire was used as the counter electrode, and an Ag/AgCl electrode was used as the reference electrode. The CV curves were calibrated with the ferrocene/ferrocenium (Fc/Fc<sup>+</sup>) redox couple as a standard measured under the same conditions. The energy level of Fc/Fc<sup>+</sup> was assumed at to be – 4.8 eV with respect to vacuum.<sup>221</sup> The LUMO of the ligands were calculated accordingly after taking into account their optical gaps. Energy levels for An-COOH and An-NHCSSH are obtained from reported values.<sup>80</sup>

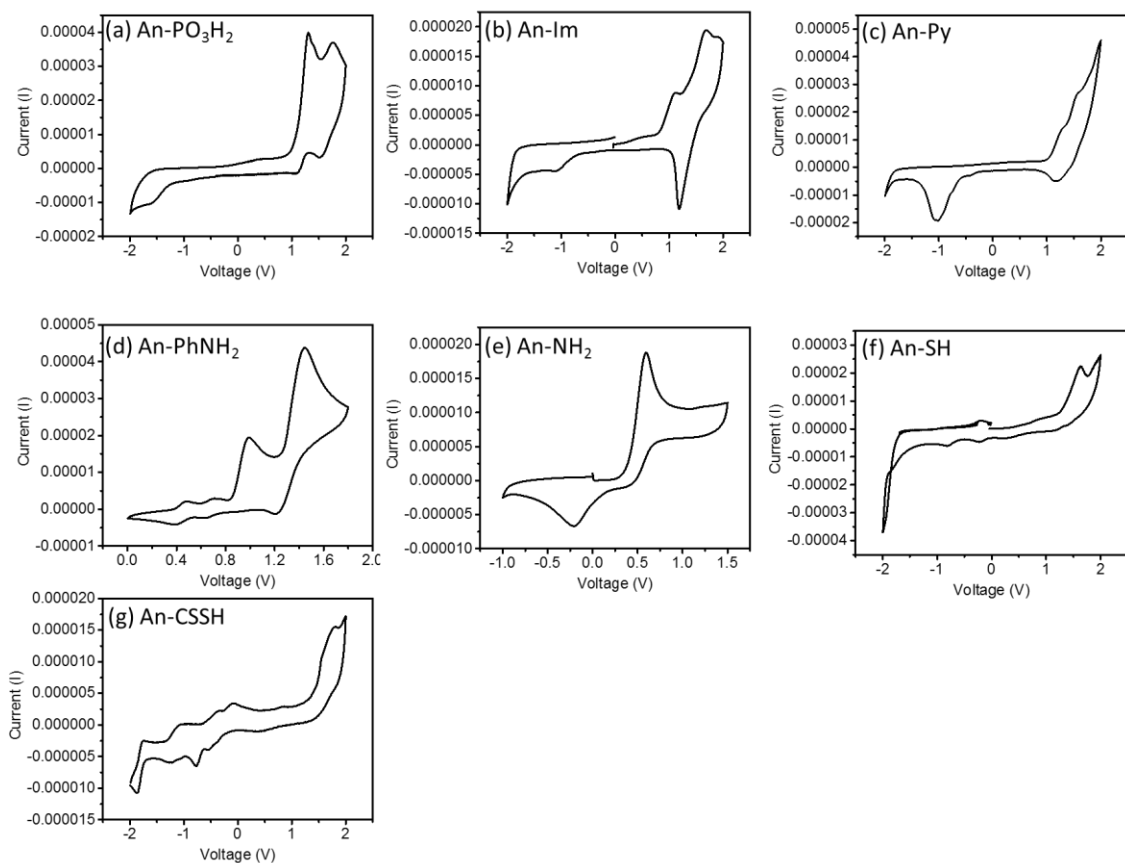


**Figure 8.24.** Cyclic voltammogram (CV) of anthracene transmitter ligands with different functional groups in an anhydrous dichloromethane (DCM) solution containing tetra-*n*-butylammonium hexafluorophosphate (0.1 M) as electrolyte. CV measurements were performed at room temperature at a scan speed of  $100 \text{ mV s}^{-1}$ . The phosphorescence from An-Py, An-NH<sub>2</sub> and An-SH could not be obtained. The energy of T<sub>1</sub> state for these three ligands are calculated as the average of the values for other ligands.

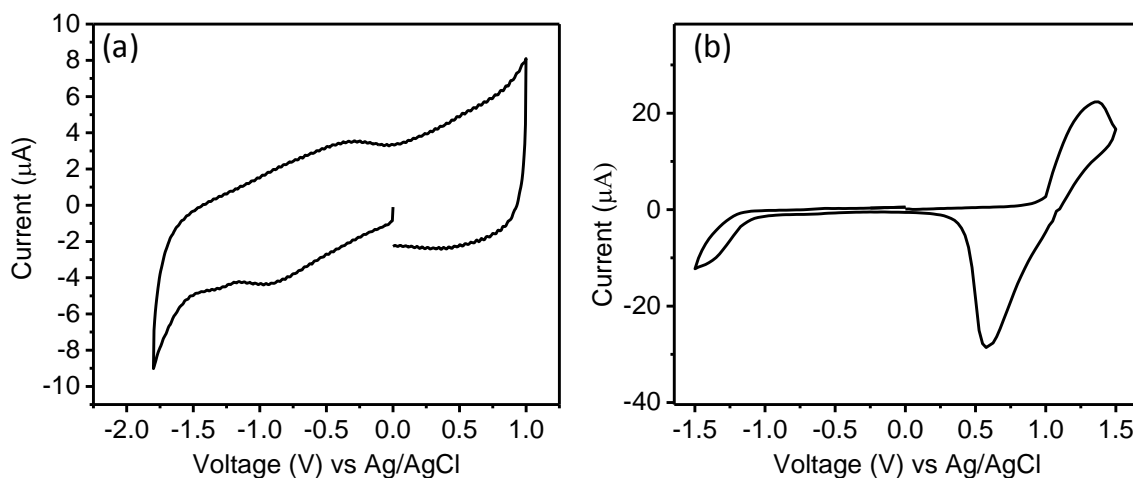


**Figure 8.25.** Cyclic voltammogram (CV) of (a) PbS/CdS core-shell QD measured at  $-50^{\circ}\text{C}$  and (b) 5-carboxylic acid tetracene measured RT. Both CVs were performed in dichloromethane at a scan speed of  $100\text{ mV s}^{-1}$ .

### 8.13 Electronic Structure Calculations

Electronic structure calculations were performed using the QChem 5.0.<sup>196</sup>

#### 8.13.1 Time-Dependent Density Functional Theory (TDDFT) Calculations

TDDFT calculations were performed at the  $S_0$ ,  $T_1$ , and  $S_1$  geometries, optimized on the DFT or TDDFT potential energy surfaces, respectively. These calculations were performed with the wB97x-D3 functional,<sup>197</sup> a 6-31G\* basis, and the Tamm-Dancoff approximation in the case of the TDDFT calculations.<sup>198</sup>

**Table 8.6.** TDDFT calculations of  $S_0/S_1$  and  $S_0/T_1$  energy gaps, activation energies for  $T_1-S_0$  transitions, and spin-orbit couplings (SOC) of  $S_0$  and  $S_1$  to triplet states for different anthracene ligands.

	An- PO <sub>3</sub> H 2	An- Im	An- Py	An- PhN H <sub>2</sub>	An- NH <sub>2</sub>	An- SH	An- NHC SSH	An- CSS H
$S_0/S_1$ Gap at $S_0$ Geometry (eV)	3.94	3.98	4.03	4.02	3.74	3.95	3.65	2.62
$S_0/T_1$ Gap at $S_0$ Geometry (eV)	2.23	2.26	2.29	2.29	2.11	2.23	2.27	2.21
$S_0/S_1$ Gap at $S_1$ Geometry (eV)	3.40	3.31	3.47	3.38	3.20	3.35	1.42	1.92
$S_0/T_1$ Gap at $T_1$ Geometry (eV)	1.41	1.44	1.53	1.52	1.40	1.43	1.53	1.52
Activation Energy from $T_1$ at the $T_1$ Geometry to $T_1$ at the $S_0/T_1$ MECP (eV)	0.53	0.40	0.43	0.43	0.79	0.54	0.70	0.18
Largest $S_0$ SOC at $S_0$ Geometry (cm <sup>-1</sup> )	2.7 (T <sub>3</sub> )	2.2 (T <sub>2</sub> )	2.3 (T <sub>2</sub> )	2.3 (T <sub>2</sub> )	1.9 (T <sub>2</sub> )	25 (T <sub>5</sub> )	169 (T <sub>2</sub> )	203 (T <sub>1</sub> )
Largest $S_1$ SOC at $S_0$ Geometry (cm <sup>-1</sup> )	1.8 (T <sub>4</sub> )	2.4 (T <sub>4</sub> )	2.6 (T <sub>4</sub> )	2.6 (T <sub>5</sub> )	1.6 (T <sub>4</sub> )	15 (T <sub>8</sub> )	170 (T <sub>3</sub> )	148 (T <sub>3</sub> )

### 8.13.2 Constrained Density Functional Theory with Configuration Interaction (CDFT-CI) Calculations

CDFT-CI couplings were calculated following our previously published methodology,<sup>182</sup> on a CdSe structure obtained from our previous molecular dynamics study.<sup>202</sup> One of the passivating ligands was replaced by the functional ligands of this study. The structure was then optimized using LANL2DZ/PBE0 as the basis set and functional respectively,<sup>203,204</sup> until the  $S^2$  of the triplet showed no spin contamination. A CDFT-CI calculation was performed between a CDFT state which restricted the spin difference on the CdSe atoms to be 2, and a second CDFT state restricting the spin difference on the functional ligand to be 2.

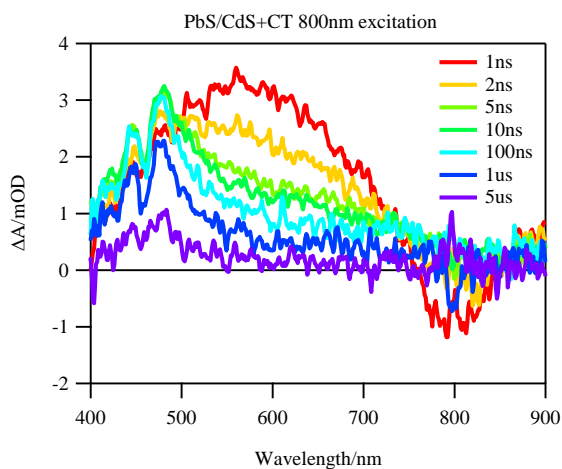
## 8.14 Methods and techniques

### 8.14.1 How to average transient absorption spectra

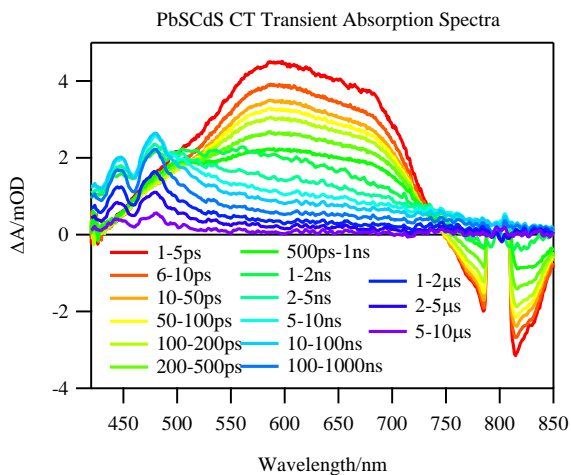
If the transient spectra are very noisy (due to low sample concentration or short integration time during measurement), the OD at each wavelength is accurate, which limits the further data process and analysis. Therefore, we need to average the spectra over a period of time so we can enhance S/N ratio.

Here is an example of the spectra before and after average:



Before:



After:



To average the spectra, you just need to average all the OD at each wavelength within the time window you select. As shown in the figure below, the first column in red is the wavelength, and the first row is the decay time. The column highlighted in yellow is the average from column B to L, which is the averaged spectra from 1 ps to 2 ps. You can plot the column M vs column A to get each curve in the figure above.

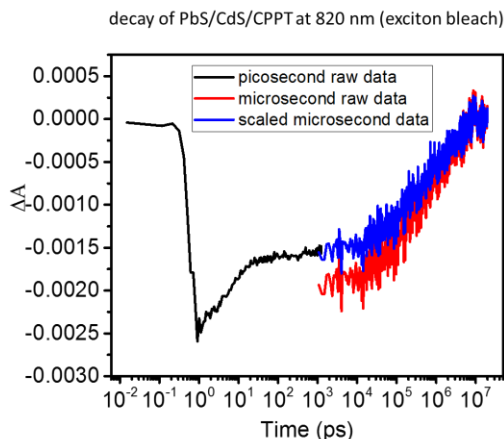
		Decay time 												
		A	B	C	D	E	F	G	H	I	J	K	L	M
Wavelength 	1		1.01ps	1.11ps	1.21ps	1.31ps	1.41ps	1.51ps	1.61ps	1.71ps	1.81ps	1.91ps	2.01ps	average
	2	406.791	-2.65E-03	-5.00E-03	3.83E-05	-1.09E-04	3.26E-03	3.74E-04	3.27E-03	5.50E-03	8.16E-03	4.25E-03	3.03E-03	1.83E-03
	3	407.376	-1.14E-03	-1.45E-03	-1.35E-03	6.46E-04	2.73E-03	2.09E-03	1.66E-03	2.10E-03	3.14E-03	-3.28E-04	1.32E-03	8.57E-04
	4	407.96	NaN	-1.24E-03	-2.10E-03	-1.19E-03	2.01E-04	-3.90E-04	-3.20E-03	-3.58E-03	-3.83E-03	-1.45E-03	-2.23E-03	-1.90E-03
	5	408.544	-1.69E-03	-1.06E-03	1.12E-03	5.30E-04	-2.07E-03	-6.89E-05	-1.72E-03	-3.27E-03	-9.11E-04	-9.64E-04	-1.83E-03	-1.08E-03
	6	409.713	6.70E-04	4.49E-03	3.35E-03	5.16E-03	6.93E-04	-4.33E-03	2.00E-03	-1.94E-04	1.20E-04	-2.20E-03	6.63E-03	1.49E-03
	7	410.297	-4.27E-03	4.04E-03	4.62E-04	2.38E-03	1.95E-04	-6.63E-05	-2.92E-03	2.07E-03	3.43E-04	2.04E-03	9.49E-04	4.74E-04
	8	410.882	6.48E-04	-2.11E-04	-1.51E-03	4.15E-04	-6.65E-04	-3.08E-03	-1.12E-03	2.50E-03	-2.86E-04	9.82E-04	2.23E-03	-8.13E-06
	9	411.466	1.12E-03	2.09E-04	-6.67E-04	1.86E-03	2.20E-03	-2.00E-04	-2.62E-04	-9.45E-04	1.82E-03	2.24E-03	-2.98E-03	3.99E-04
	10	412.051	2.75E-03	4.24E-03	3.28E-03	7.23E-04	2.48E-05	2.46E-04	-1.84E-05	-8.46E-04	8.42E-04	-1.53E-03	-3.85E-03	5.32E-04
	11	412.635	1.01E-03	2.99E-03	2.93E-03	2.40E-03	2.55E-03	3.13E-03	2.56E-03	8.68E-04	2.10E-03	1.66E-03	-1.94E-04	2.00E-03
	12	413.22	-9.88E-04	8.32E-04	2.81E-03	3.18E-03	-1.52E-03	-1.20E-03	7.59E-04	-6.57E-04	6.97E-04	9.72E-04	4.30E-04	4.83E-04
	13	413.804	-1.53E-03	6.18E-04	8.28E-04	1.72E-03	-8.19E-04	7.49E-04	-1.98E-05	-1.18E-03	2.08E-04	-8.21E-04	1.07E-03	7.58E-05
	14	414.389	-2.14E-03	-7.43E-04	-9.55E-04	-9.58E-04	-3.90E-04	3.11E-03	-2.72E-04	-2.10E-03	-1.71E-03	2.96E-05	-2.34E-03	-7.70E-04
	15	414.974	1.31E-03	3.37E-03	3.49E-04	1.53E-03	1.12E-03	2.95E-03	5.74E-04	2.22E-04	-1.25E-04	2.89E-03	-8.91E-04	1.21E-03
	16	415.558	2.62E-03	-1.62E-04	5.69E-04	2.01E-03	-2.02E-04	6.47E-04	7.22E-06	-4.81E-04	2.60E-04	9.97E-04	8.73E-04	6.49E-04
	17	416.143	5.31E-04	-9.01E-04	-2.35E-04	-1.37E-03	1.20E-05	5.95E-04	-1.63E-03	-3.31E-04	2.53E-03	1.25E-03	6.11E-05	4.68E-05
	18	416.728	-1.06E-03	-6.24E-04	-4.25E-04	-8.78E-04	-3.58E-05	9.80E-04	7.34E-04	9.96E-05	1.16E-03	-1.25E-04	1.11E-04	-5.08E-06
	19	417.312	3.70E-05	1.29E-04	1.26E-03	1.28E-03	-1.83E-04	5.18E-04	-3.91E-04	-6.52E-04	2.36E-04	-7.55E-04	-4.56E-05	1.30E-04
	20	417.897	9.31E-04	6.25E-04	2.35E-04	-1.17E-04	3.09E-04	3.58E-04	-3.75E-04	1.10E-04	5.88E-04	4.20E-04	3.98E-04	3.17E-04
	21	418.482	9.44E-04	3.04E-04	-1.16E-03	-1.01E-03	3.81E-04	5.07E-04	-3.07E-04	-4.57E-04	-7.04E-04	1.90E-04	1.54E-03	2.07E-05
	22	419.067	-1.11E-04	2.35E-04	-8.57E-04	-1.41E-03	2.20E-04	1.43E-03	7.20E-05	-1.11E-03	-6.31E-04	-1.24E-03	6.51E-05	-3.04E-04
	23	419.652	-4.98E-04	3.84E-04	5.87E-04	-3.66E-04	-7.04E-06	5.89E-04	-7.67E-05	-2.56E-04	-3.24E-04	4.23E-05	-6.38E-04	

Principles to select time window for average:

1. Don't choose the time within the instrument response. Let's say for femtosecond laser, you should start average the data after tens of picosecond.
2. The time interval is chosen based on the S/N ratio. S/N will increase if more spectra are averaged. Also, you should choose the interval to make the curves evenly spaced in the overlay plot to make the figure looks nice.

### 8.14.2 How to combine the decay in picosecond and microsecond time scales in transient absorption spectra

In transient absorption spectra, data in picosecond and microsecond timescale are obtained with the excitation of femtosecond and nanosecond lasers. Because of the different laser intensities and beam sizes, even measured with the same sample, the two sets of data cannot be directly combined without normalization, such as the black and red curves in the figure below. Therefore, if we want to study the decay throughout the picosecond and microsecond timescale, we need to combine these two sets of data with normalization.

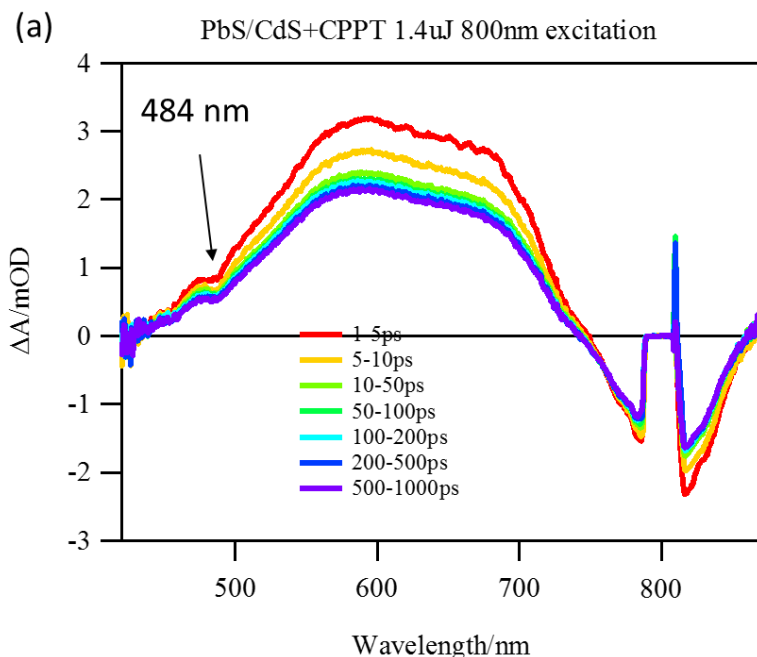


In this figure, the black and red curves are the decays of the sample at 820 nm in picosecond and microsecond time scales respectively. To combine the two curves, we just need to scale the red curve so that the scaled curve (blue curve) has the same  $\Delta A$  value as the black curve at a specific decay time. This decay time is chosen where the picosecond and microsecond data should have overlap on time scale, 1 ns in this case. In this way, the decays in picosecond and microsecond time scales are combined.



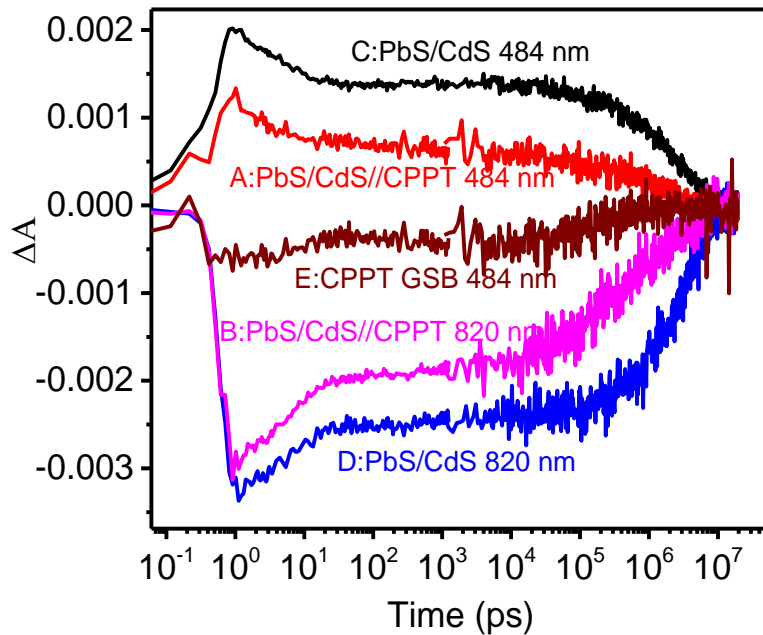
### 8.14.3 How to extract the individual decay from a mixture of two decays

In transient absorption spectra, sometimes at a specific wavelength the overall decay is the accumulative results of two individual decay processes. For example, figure (a) below shows the transient absorption spectra of PbS/CdS core-shell nanocrystals (NCs) capped with 5-carboxylphenylphenyltetracene (CPPT). At 484 nm, the negative peak pointed by the arrow is the ground state bleach of CPPT, which overlaps with the broad excited state absorption of NCs. So, if we plot the decay at 484 nm, the overall decay contains the decay of CPPT ground state bleach and NC excited state absorption. In this case, if we want to study the kinetics of the CPPT ground state bleach only, we need to separate this decay process out of the overall decay.



Generally, if these two overlapped decay processes are independent and not correlated, we can just subtract the decay at 484 nm for NC without CPPT from that for

NC/CPPT, so that we obtain the decay of CPPT ground state bleach. It's a little bit complicated if these two processes are correlated. For example, in this case the presence of CPPT makes NCs decay faster comparing to the situation without CPPT. Therefore, the idea is to use the ratio of decays at 820 nm (exciton bleach) for NCs with and without CPPT as a correction term to get rid of the different NC decay due to the presence of CPPT. In this case, to extract the decay of CPPT ground state bleach, we need:



Curve A: the decay of NC/CPPT at 484 nm

Curve B: the decay of NC/CPPT at 820 nm (NC exciton bleach)

Curve C: decay of NC without CPPT at 484 nm, obtained from the transient absorption data of NC only.

Curve D: decay of NC without CPPT at 820 nm, obtained from the transient absorption data of NC only.

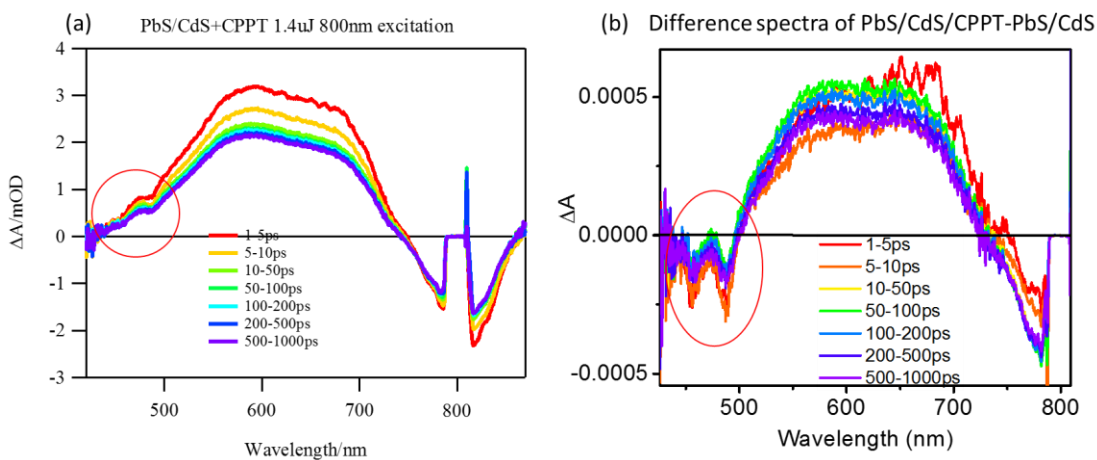
Note that the four curves have been normalized by the OD at 820 nm of the NCs with and without CPPT obtained from steady state absorption spectra to get rid of the influence of different concentrations of nanocrystals in these two samples.

The separated decay of CPPT ground state bleach  $\text{curve E} = \text{curve A} - \text{curve C} * (\text{curve B} / \text{curve D})$

#### 8.14.4 Extract transient absorption difference spectra

What is difference spectra and why do we need difference spectra?

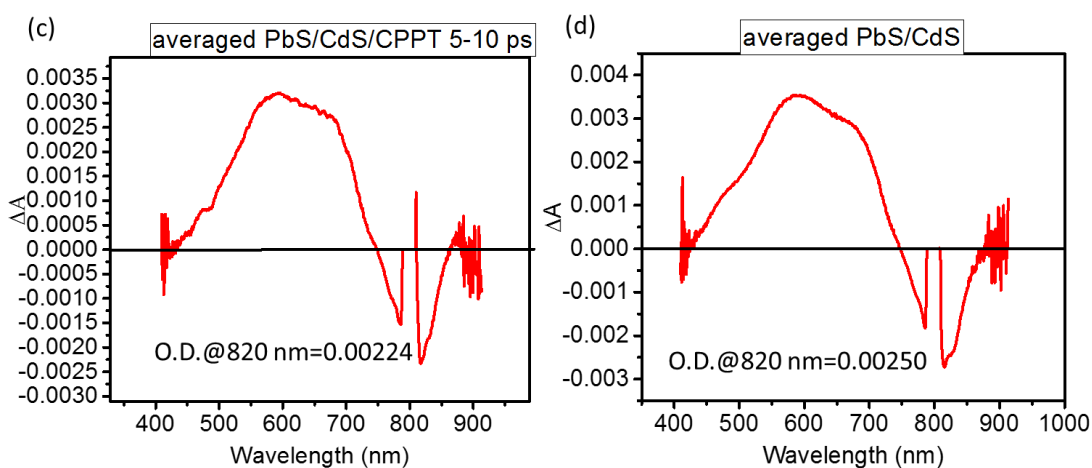
Difference spectra is the spectra obtained by the subtraction between two spectra. In transient absorption, if the spectra of two components are superimposed, it's hard to distinguish the absorption feature of a certain component from the mixture. In this case, we need to do the subtraction between the superimposed spectra and the spectrum of one component that you've already known, to extract the spectrum of the other one.



For example, figure (a) is the transient absorption spectra of PbS/CdS core-shell nanocrystal capped with 5-carboxylphenylphenyltetracene (CPPT). In the region of 450-500 nm (circled in red), the excited state absorption of nanocrystal and ground state bleach

of CPPT overlaps. In this case, it's not clear to see if there is CPPT ground state bleach. But if we remove the contribution of nanocrystals from the superimposed spectra by subtracting the spectra of PbS/CdS from that of PbS/CdS/CPPT, we can clearly see the ground state bleach of CPPT. The difference spectra are shown in figure (b).

Procedure of obtaining difference spectra, taking PbS/CdS/CPPT as an example:

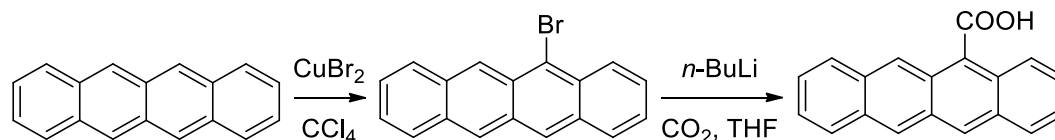


1. Plot the transient absorption spectra of PbS/CdS/CPPT and PbS/CdS, shown in figure (c) and (d) respectively. If the transient absorption spectra are noisy, you need to use the averaged spectra (see SOP “How to average spectra”).

2. Scale the spectra in figure (d) to (c) based on the O.D. at 820 nm (nanocrystal exciton bleach).

3. Subtract the scaled (d) from (c) to get the difference spectrum (the orange curve in figure (b)). In this case, difference spectra= (curve in figure c)-(curve in figure d)/0.00250\*0.00224

#### 8.14.5 Synthesis and purification of 5-tetracene carboxylic acid (5-CT)



Tricks:

Step 1:

After the reaction is done, transfer the reaction solution (no workup needed) on alumina column and flush the column with 10/1 hexane/ethyl acetate. You will see three separated yellow bands when running the column: 5,12-dibromotetracene, the minor component which comes out first; 5-bromotetracene, the target and major product; tetracene which comes out last. Collect the second component.

If using the largest 3" diameter column, then pack 4" height of alumina.

Step 2:

Reaction: after adding  $n\text{-BuLi}$ , bubble the solution with  $\text{CO}_2$  for 30 min at  $-78\text{ }^\circ\text{C}$  and another 1h at room temperature. TLC is used to monitor the reaction.

Workup: after the reaction is done, remove THF on rotavap and dissolve the crude product in 1 M NaOH aqueous solution. Filter out the undissolved solid and collect the filtrate. Here after the first filtration, we drop the filter paper with the solid residue inside the Buchner funnel into 1 M NaOH aqueous solution, sonicate and filter again. Combine the filtrate with the previous one and acidify with HCl.

As 5-CT are not fully basified by NaOH, there is still some residue on the filter paper after the first filtration. The sonication of the filter paper with the solid in NaOH allows us to collect more product.

Recrystallization: for upconversion use, recrystallize three times with THF/hexane. Dissolve crude product in minimum amount of THF (~0.5 mL for 1g 5-CT). Add hexane dropwise. You will see white precipitant. Stop adding hexane until you just see the red precipitant. Filter out the solid and put the filtrate in freezer overnight. Collect the red crystals.

Don't use any heat. We found every time we heat the solution, there's more white precipitant generated. As the solution is not heated, no need to do in glovebox. Another trick is that THF is such a good solvent for 5-CT that you may not see any precipitant when adding hexane if you add a little excessive amount THF. In this case, you can remove some THF on rotar-vap till you see the precipitant.

## References

- (1) Holder, E.; Tessler, N.; Rogach, A. L. *Journal of Materials Chemistry* **2008**, *18*, 1064.
- (2) Yoshida, T.; Zhang, J.; Komatsu, D.; Sawatani, S.; Minoura, H.; Pauporté, T.; Lincot, D.; Oekermann, T.; Schlettwein, D.; Tada, H. *Advanced Functional Materials* **2009**, *19*, 17.
- (3) Larson, D. R.; Zipfel, W. R.; Williams, R. M.; Clark, S. W.; Bruchez, M. P.; Wise, F. W.; Webb, W. W. *Science* **2003**, *300*, 1434.
- (4) Fan, X.; Zhang, M.; Wang, X.; Yang, F.; Meng, X. *Journal of Materials Chemistry A* **2013**, *1*, 8694.
- (5) O'Regan, B.; Gratzel, M. *Nature* **1991**, *353*, 737.
- (6) From NREL efficiency chart by Sharp certified by AIST in 2013.
- (7) Leatherdale, C. A.; Woo, W.-K.; Mikulec, F. V.; Bawendi, M. G. *The Journal of Physical Chemistry B* **2002**, *106*, 7619.
- (8) Moreels, I.; Lambert, K.; De Muynck, D.; Vanhaecke, F.; Poelman, D.; Martins, J. C.; Allan, G.; Hens, Z. *Chemistry of Materials* **2007**, *19*, 6101.
- (9) Moreels, I.; Lambert, K.; Smeets, D.; De Muynck, D.; Nollet, T.; Martins, J. C.; Vanhaecke, F.; Vantomme, A.; Delerue, C.; Allan, G. *ACS nano* **2009**, *3*, 3023.
- (10) Cademartiri, L.; Montanari, E.; Calestani, G.; Migliori, A.; Guagliardi, A.; Ozin, G. A. *Journal of the American Chemical Society* **2006**, *128*, 10337.
- (11) Singh-Rachford, T. N.; Castellano, F. N. *Coordination Chemistry Reviews* **2010**, *254*, 2560.
- (12) Auzel, F. *C. R. Acad. Sci. Paris* **1966**, *B262*, 1016.
- (13) Martín-Rodríguez, R.; Fischer, S.; Ivaturi, A.; Froehlich, B.; Krämer, K. W.; Goldschmidt, J. C.; Richards, B. S.; Meijerink, A. *Chemistry of Materials* **2013**, *25*, 1912.
- (14) Boyer, J.-C.; van Veggel, F. C. J. M. *Nanoscale* **2010**, *2*, 1417.

- (15) Huang, P.; Zheng, W.; Zhou, S.; Tu, D.; Chen, Z.; Zhu, H.; Li, R.; Ma, E.; Huang, M.; Chen, X. *Angewandte Chemie International Edition* **2014**, *53*, 1252.
- (16) Nadort, A.; Zhao, J.; Goldys, E. M. *Nanoscale* **2016**.
- (17) Zhang, L.; Leng, Y.; Zhang, J.; Hu, L. *Journal of Materials Science & Technology* **2010**, *26*, 921.
- (18) Chen, G.; Qiu, H.; Prasad, P. N.; Chen, X. *Chemical reviews* **2014**, *114*, 5161.
- (19) Dou, L.; Liu, Y.; Hong, Z.; Li, G.; Yang, Y. *Chemical reviews* **2015**, *115*, 12633.
- (20) Englman, R.; Jortner, J. *Molecular Physics* **1970**, *18*, 145.
- (21) Smith, M. B.; Michl, J. *Chemical Reviews* **2010**, *110*, 6891.
- (22) Bardeen, C. J. *Nat Mater* **2014**, *13*, 1001.
- (23) Thompson, N. J.; Wilson, M. W. B.; Congreve, D. N.; Brown, P. R.; Scherer, J. M.; Bischof, Thomas S.; Wu, M.; Geva, N.; Welborn, M.; Voorhis, T. V.; Bulović, V.; Bawendi, M. G.; Baldo, Marc A. *Nat Mater* **2014**, *13*, 1039.
- (24) Tabachnyk, M.; Ehrler, B.; Gélinas, S.; Böhm, M. L.; Walker, B. J.; Musselman, K. P.; Greenham, N. C.; Friend, R. H.; Rao, A. *Nature materials* **2014**, *13*, 1033.
- (25) Huang, Z.; Li, X.; Mahboub, M.; Hanson, K. M.; Nichols, V. M.; Le, H.; Tang, M. L.; Bardeen, C. J. *Nano Lett.* **2015**, *15*, 5552.
- (26) Wu, M.; Congreve, D. N.; Wilson, M. W.; Jean, J.; Geva, N.; Welborn, M.; Van Voorhis, T.; Bulović, V.; Bawendi, M. G.; Baldo, M. A. *Nature Photonics* **2016**, *10*, 31.
- (27) Mongin, C.; Garakyaraghi, S.; Razgoniaeva, N.; Zamkov, M.; Castellano, F. N. *Science* **2016**, *351*, 369.
- (28) Piland, G. B.; Huang, Z.; Lee Tang, M.; Bardeen, C. J. *The Journal of Physical Chemistry C* **2016**, *120*, 5883.
- (29) Okumura, K.; Mase, K.; Yanai, N.; Kimizuka, N. *Chemistry – A European Journal* **2016**, *22*, 7721.



- (30) Gray, V.; Xia, P.; Huang, Z.; Moses, E.; Fast, A.; Fishman, D. A.; Vullev, V. I.; Abrahamsson, M.; Moth-Poulsen, K.; Lee Tang, M. *Chemical Science* **2017**.
- (31) Singh-Rachford, T. N.; Castellano, F. N. *The Journal of Physical Chemistry A* **2009**, *113*, 5912.
- (32) Merkel, P. B.; Dinnocenzo, J. P. *Journal of Luminescence* **2009**, *129*, 303.
- (33) Mahboub, M.; Huang, Z.; Tang, M. L. *Nano Letters* **2016**, *16*, 7169.
- (34) Huang, Z.; Li, X.; Yip, B. D.; Rubalcava, J. M.; Bardeen, C. J.; Tang, M. L. *Chemistry of Materials* **2015**, *27*, 7503.
- (35) Mahboub, M.; Maghsoudiganjeh, H.; Pham, A. M.; Huang, Z.; Tang, M. L. *Advanced Functional Materials* **2016**.
- (36) Huang, Z.; Simpson, D. E.; Mahboub, M.; Li, X.; Tang, M. L. *Chemical Science* **2016**.
- (37) Li, X.; Huang, Z.; Zavala, R.; Tang, M. L. *The Journal of Physical Chemistry Letters* **2016**, *7*, 1955.
- (38) Schmidt, T. W.; Castellano, F. N. *The journal of physical chemistry letters* **2014**, *5*, 4062.
- (39) Feldt, S. M.; Lohse, P. W.; Kessler, F.; Nazeeruddin, M. K.; Grätzel, M.; Boschloo, G.; Hagfeldt, A. *Physical Chemistry Chemical Physics* **2013**, *15*, 7087.
- (40) Monguzzi, A.; Tubino, R.; Hoseinkhani, S.; Campione, M.; Meinardi, F. *Physical Chemistry Chemical Physics* **2012**, *14*, 4322.
- (41) Sripathy, K.; MacQueen, R. W.; Peterson, J. R.; Cheng, Y. Y.; Dvořák, M.; McCamey, D. R.; Treat, N. D.; Stingelin, N.; Schmidt, T. W. *Journal of Materials Chemistry C* **2015**, *3*, 616.
- (42) Cheng, Y. Y.; Khoury, T.; Clady, R. G. C. R.; Tayebjee, M. J. Y.; Ekins-Daukes, N. J.; Crossley, M. J.; Schmidt, T. W. *Physical Chemistry Chemical Physics* **2010**, *12*, 66.
- (43) Morris, J. V.; Mahaney, M. A.; Huber, J. R. *The Journal of Physical Chemistry* **1976**, *80*, 969.
- (44) Martinho, J.; Maçanita, A.; Berberan-Santos, M. *The Journal of chemical physics* **1989**, *90*, 53.

- (45) Montalti, M.; Credi, A.; Prodi, L.; Gandolfi, M. T. *Handbook of photochemistry*; CRC press, 2006.
- (46) Kohler, A.; Bassler, H. *Journal of Materials Chemistry* **2011**, *21*, 4003.
- (47) Cheng, M.; Yang, X.; Zhang, F.; Zhao, J.; Sun, L. *The Journal of Physical Chemistry C* **2013**, *117*, 9076.
- (48) Hagberg, D. P.; Marinado, T.; Karlsson, K. M.; Nonomura, K.; Qin, P.; Boschloo, G.; Brinck, T.; Hagfeldt, A.; Sun, L. *The Journal of organic chemistry* **2007**, *72*, 9550.
- (49) Zöphel, L.; Enkelmann, V.; Müllen, K. *Organic letters* **2013**, *15*, 804.
- (50) Shi, M.; Li, F.; Yi, T.; Zhang, D.; Hu, H.; Huang, C. *Inorganic Chemistry* **2005**, *44*, 8929.
- (51) Hagfeldt, A.; Boschloo, G.; Sun, L.; Kloo, L.; Pettersson, H. *Chemical reviews* **2010**, *110*, 6595.
- (52) Heinecke, E.; Hartmann, D.; Muller, R.; Hese, A. *Journal of Chemical Physics* **1998**, *109*, 906.
- (53) Burgos, J.; Pope, M.; Swenberg, C. E.; Alfano, R. *physica status solidi (b)* **1977**, *83*, 249.
- (54) Uejima, M.; Sato, T.; Tanaka, K.; Kaji, H. *Chemical Physics* **2014**, *430*, 47.
- (55) Ding, T. X.; Olshansky, J. H.; Leone, S. R.; Alivisatos, A. P. *Journal of the American Chemical Society* **2015**, *137*, 2021.
- (56) Wenger, O. S. *Chemical Society Reviews* **2011**, *40*, 3538.
- (57) Welter, S.; Salluce, N.; Belser, P.; Groeneveld, M.; De Cola, L. *Coordination Chemistry Reviews* **2005**, *249*, 1360.
- (58) Barigelletti, F.; Flamigni, L.; Guardigli, M.; Juris, A.; Beley, M.; Chodorowski-Kimmes, S.; Collin, J.-P.; Sauvage, J.-P. *Inorganic Chemistry* **1996**, *35*, 136.
- (59) Skourtis, S. S.; Liu, C.; Antoniou, P.; Virshup, A. M.; Beratan, D. N. *Proceedings of the National Academy of Sciences* **2016**, *113*, 8115.

- (60) Closs, G. L.; Johnson, M. D.; Miller, J. R.; Piotrowiak, P. *Journal of the American Chemical Society* **1989**, *111*, 3751.
- (61) Brutchey, R.; Hens, Z.; Kovalenko, M. V. In *Chemistry of Organo-Hybrids*; John Wiley & Sons, Inc.: 2014, p 233.
- (62) Donakowski, M. D.; Godbe, J. M.; Sknepnek, R.; Knowles, K. E.; Olvera de la Cruz, M.; Weiss, E. A. *The Journal of Physical Chemistry C* **2010**, *114*, 22526.
- (63) Bullen, C.; Mulvaney, P. *Langmuir* **2006**, *22*, 3007.
- (64) Ji, X.; Copenhaver, D.; Sichmeller, C.; Peng, X. *Journal of the American Chemical Society* **2008**, *130*, 5726.
- (65) Schapotschnikow, P.; Hommersom, B.; Vlugt, T. J. H. *The Journal of Physical Chemistry C* **2009**, *113*, 12690.
- (66) Puzder, A.; Williamson, A. J.; Zaitseva, N.; Galli, G.; Manna, L.; Alivisatos, A. P. *Nano Letters* **2004**, *4*, 2361.
- (67) Knauf, R. R.; Lennox, J. C.; Dempsey, J. L. *Chemistry of Materials* **2016**, *28*, 4762.
- (68) Gomes, R.; Hassinen, A.; Szczygiel, A.; Zhao, Q.; Vantomme, A.; Martins, J. C.; Hens, Z. *The Journal of Physical Chemistry Letters* **2011**, *2*, 145.
- (69) Koole, R.; Schapotschnikow, P.; de Mello Donegá, C.; Vlugt, T. J.; Meijerink, A. *Acs Nano* **2008**, *2*, 1703.
- (70) Wolfgang, J. P.; Daniele, G.; Teresa, P.; Daniela, Z.; Christine, M.; Shara, C. W.; Rosanne, B.; Mark, A. L. G.; Carolyn, A. L.; Alivisatos, A. P. *Nanotechnology* **2003**, *14*, R15.
- (71) Medintz, I. L.; Uyeda, H. T.; Goldman, E. R.; Mattoussi, H. *Nat Mater* **2005**, *4*, 435.
- (72) Mattoussi, H.; Mauro, J. M.; Goldman, E. R.; Anderson, G. P.; Sundar, V. C.; Mikulec, F. V.; Bawendi, M. G. *Journal of the American Chemical Society* **2000**, *122*, 12142.
- (73) Li, X.; Fast, A.; Huang, Z.; Fishman, D. A.; Tang, M. L. *Angewandte Chemie International Edition* **2017**, *56*, 5598.

- (74) Seker, F.; Meeker, K.; Kuech, T. F.; Ellis, A. B. *Chemical reviews* **2000**, *100*, 2505.
- (75) Kalyuzhny, G.; Murray, R. W. *The Journal of Physical Chemistry B* **2005**, *109*, 7012.
- (76) Wuister, S. F.; de Mello Donegá, C.; Meijerink, A. *The Journal of Physical Chemistry B* **2004**, *108*, 17393.
- (77) Lian, S.; Weinberg, D. J.; Harris, R. D.; Kodaimati, M. S.; Weiss, E. A. *ACS nano* **2016**.
- (78) Knowles, K. E.; Tice, D. B.; McArthur, E. A.; Solomon, G. C.; Weiss, E. A. *Journal of the American Chemical Society* **2010**, *132*, 1041.
- (79) Li, X.; Slyker, L. W.; Nichols, V. M.; Pau, G. S. H.; Bardeen, C. J.; Tang, M. L. *The Journal of Physical Chemistry Letters* **2015**, *6*, 1709.
- (80) Xia, P.; Huang, Z.; Li, X.; Romero, J. J.; Vullev, V. I.; Pau, G. S. H.; Tang, M. L. *Chemical Communications* **2017**, *53*, 1241.
- (81) Zhang, L.; Cole, J. M. *ACS applied materials & interfaces* **2015**, *7*, 3427.
- (82) Guerrero, G.; Alauzun, J. G.; Granier, M.; Laurencin, D.; Mutin, P. H. *Dalton Transactions* **2013**, *42*, 12569.
- (83) Murov, S. L.; Carmichael, I.; Hug, G. L. *Handbook of photochemistry*; CRC Press, 1993.
- (84) Maliakal, A.; Raghavachari, K.; Katz, H.; Chandross, E.; Siegrist, T. *Chemistry of materials* **2004**, *16*, 4980.
- (85) Anthony, J. E.; Brooks, J. S.; Eaton, D. L.; Parkin, S. R. *Journal of the American Chemical Society* **2001**, *123*, 9482.
- (86) Zhao, W.; Castellano, F. N. *The Journal of Physical Chemistry A* **2006**, *110*, 11440.
- (87) Hoseinkhani, S.; Tubino, R.; Meinardi, F.; Monguzzi, A. *Physical Chemistry Chemical Physics* **2015**, *17*, 4020.
- (88) Singh-Rachford, T. N.; Haeferle, A.; Ziesel, R.; Castellano, F. N. *Journal of the American Chemical Society* **2008**, *130*, 16164.

- (89) Park, Y. I.; Lee, K. T.; Suh, Y. D.; Hyeon, T. *Chem. Soc. Rev.* **2015**, *44*, 1302.
- (90) Zhu, Y.; Han, S.-T.; Chen, X.; Wang, F.; Tang, Y.-B.; Roy, V. A. L. *Nat. Comm.* **2014**, *5*, 4720 (1.
- (91) Schulze, T. F.; Schmidt, T. W. *Ener. Envir. Sci.* **2015**, *8*, 103.
- (92) Goldschmidt, J. C.; Fischer, S. *Adv. Opt. Mater.* **2015**, *3*, 510.
- (93) Singh-Rachford, T. N.; Castellano, F. N. *Coordination Chemistry Reviews* **2010**, *254*, 2560.
- (94) Balushev, S.; Miteva, T.; Yakutkin, V.; Nelles, G.; Yasuda, A.; Wegner, G. *Phys. Rev. Lett.* **2006**, *97*, 143903/1.
- (95) Hoseinkhani, S.; Tubino, R.; Meinardi, F.; Monguzzi, A. *Phys. Chem. Chem. Phys.* **2015**, *17*, 4020.
- (96) Zhou, J.; Liu, Q.; Feng, W.; Sun, Y.; Li, F. Y. *Chemical Reviews* **2015**, *115*, 395.
- (97) Yakutkin, V.; Aleshchenkov, S.; Chernov, S.; Miteva, T.; Nelles, G.; Cheprakov, A.; Balushev, S. *Chemistry-a European Journal* **2008**, *14*, 9846.
- (98) Wu, D. M.; Garcia-Etxarri, A.; Salleo, A.; Dionne, J. A. *Journal of Physical Chemistry Letters* **2014**, *5*, 4020.
- (99) Khetubol, A.; Snick, S. V.; Hassinen, A.; Fron, E.; Firdaus, Y.; Pandey, L.; David, C. C.; Duerinckx, K.; Dehaen, W.; Hens, Z.; Auweraer, M. V. d. *J. Appl. Phys.* **2013**, *113*, 083507.
- (100) Tabachnyk, M.; Ehrler, B.; Gelinas, S.; Bohm, M. L.; Walker, B. J.; Musselman, K. P.; Greenham, N. C.; Friend, R. H.; Rao, A. *Nature Materials* **2014**, *13*, 1033.
- (101) Thompson, N. J.; Wilson, M. W. B.; Congreve, D. N.; Brown, P. R.; Scherer, J. M.; Bischof, T. S.; Wu, M. F.; Geva, N.; Welborn, M.; Van Voorhis, T.; Bulovic, V.; Bawendi, M. G.; Baldo, M. A. *Nature Materials* **2014**, *13*, 1039.
- (102) Samia, A. C. S.; Chen, X.; Burda, C. *J. Am. Chem. Soc.* **2003**, *125*, 15736.
- (103) Cossairt, B. M.; Juhas, P.; Billinge, S. J. L.; Owen, J. S. *Journal of Physical Chemistry Letters* **2011**, *2*, 3075.

(104) Monguzzi, A.; Braga, D.; Gandini, M.; Holmberg, V. C.; Kim, D. K.; Sahu, A.; Norris, D. J.; Meinardi, F. *Nano Lett.* **2014**, *14*, 6644.

(105) Schmidt, T. W.; Castellano, F. N. *J. Phys. Chem. Lett.* **2014**, *5*, 4062.

(106) Montalti, M. C., A.; Prodi, L. *Handbook of photochemistry*; CRC Press, Boca Raton, FL, 2006.

(107) Moreels, I.; Lambert, K.; Smeets, D.; De Muynck, D.; Nollet, T.; Martins, J. C.; Vanhaecke, F.; Vantomme, A.; Delerue, C.; Allan, G.; Hens, Z. *Acs Nano* **2009**, *3*, 3023.

(108) Yu, W. W.; Qu, L. H.; Guo, W. Z.; Peng, X. G. *Chemistry of Materials* **2003**, *15*, 2854.

(109) Haefele, A.; Blumhoff, J.; Khnayzer, R. S.; Castellano, F. N. *J. Phys. Chem. Lett.* **2012**, *3*, 299.

(110) Boyer, J. C.; van Veggel, F. *Nanoscale* **2010**, *2*, 1417.

(111) Wehrenberg, B. L.; Wang, C. J.; Guyot-Sionnest, P. *Journal of Physical Chemistry B* **2002**, *106*, 10634.

(112) Burgdorff, G.; Kircher, T.; Lohmannsroben, H.-G. *Spectrochim. Acta A* **1988**, *44*, 1137.

(113) Nirmal, M.; Norris, D. J.; Kuno, M.; Bawendi, M. G.; Efros, A. L.; Rosen, M. *Physical Review Letters* **1995**, *75*, 3728.

(114) Efros, A. L.; Rosen, M.; Kuno, M.; Nirmal, M.; Norris, D. J.; Bawendi, M. *Physical Review B* **1996**, *54*, 4843.

(115) Kang, I.; Wise, F. W. *Journal of the Optical Society of America B-Optical Physics* **1997**, *14*, 1632.

(116) Talapin, D. V.; Murray, C. B. *Science* **2005**, *310*, 86.

(117) Semonin, O. E.; Luther, J. M.; Choi, S.; Chen, H.-Y.; Gao, J.; Nozik, A. J.; Beard, M. C. *Science* **2011**, *334*, 1530.

(118) Choi, J.-H.; Fafarman, A. T.; Oh, S. J.; Ko, D.-K.; Kim, D. K.; Diroll, B. T.; Muramoto, S.; Gillen, J. G.; Murray, C. B.; Kagan, C. R. *Nano Letters* **2012**, *12*, 2631.

- (119) Kowert, B. A.; Dang, N. C.; Sobush, K. T.; Seele, L. G. *J. Phys. Chem. A* **2001**, *105*, 12332.
- (120) Lissau, J. S.; Nauroozi, D.; Santoni, M.-P.; Edvinsson, T.; Ott, S.; Gardner, J. M.; Morandeira, A. *The Journal of Physical Chemistry C* **2015**, *119*, 4550.
- (121) Lissau, J. S.; Nauroozi, D.; Santoni, M.-P.; Ott, S.; Gardner, J. M.; Morandeira, A. *The Journal of Physical Chemistry C* **2013**, *117*, 14493.
- (122) Lissau, J. S.; Nauroozi, D.; Santoni, M.-P.; Ott, S.; Gardner, J. M.; Morandeira, A. *The Journal of Physical Chemistry C* **2015**, *119*, 25792.
- (123) Wu, M.; Congreve, D. N.; Wilson, M. W. B.; Jean, J.; Geva, N.; Welborn, M.; Van Voorhis, T.; Bulović, V.; Bawendi, M. G.; Baldo, M. A. *Nat Photon* **2016**, *10*, 31.
- (124) Haase, M.; Schäfer, H. *Angew. Chem. Int. Ed.* **2011**, *50*, 5808.
- (125) Kaiser, W.; Garrett, C. G. B. *Phys. Rev. Lett.* **1961**, *7*, 229.
- (126) Göppert-Mayer, M. *Annalen der Physik* **1931**, *401*, 273.
- (127) Denk, W.; Strickler, J.; Webb, W. *Science* **1990**, *248*, 73.
- (128) Schulze, T. F.; Schmidt, T. W. *Energy & Environmental Science* **2015**, *8*, 103.
- (129) Wang, H.-Q.; Batentschuk, M.; Osvet, A.; Pinna, L.; Brabec, C. J. *Adv. Mater.* **2011**, *23*, 2675.
- (130) Weifeng, Y.; Xiyan, L.; Dongzhi, C.; Hongjie, Z.; Xiaogang, L. *Nanotechnology* **2014**, *25*, 482001.
- (131) Shalav, A.; Richards, B. S.; Trupke, T.; Krämer, K. W.; Güdel, H. U. *Applied Physics Letters* **2005**, *86*, 013505.
- (132) Trupke, T.; Shalav, A.; Richards, B. S.; Würfel, P.; Green, M. A. *Solar Energy Materials and Solar Cells* **2006**, *90*, 3327.
- (133) Ahrens, B.; Löper, P.; Goldschmidt, J. C.; Glunz, S.; Henke, B.; Miclea, P.-T.; Schweizer, S. *physica status solidi (a)* **2008**, *205*, 2822.
- (134) Cheng, Y. Y.; Fückel, B.; MacQueen, R. W.; Khoury, T.; Clady, R. G.; Schulze, T. F.; Ekins-Daukes, N.; Crossley, M. J.; Stannowski, B.; Lips, K. *Energy & Environmental Science* **2012**, *5*, 6953.

- (135) Schulze, T. F.; Cheng, Y. Y.; Fückel, B.; MacQueen, R. W.; Danos, A.; Davis, N. J. L. K.; Tayebjee, M. J. Y.; Khoury, T.; Clady, R. G. C. R.; Ekins-Daukes, N. J.; Crossley, M. J.; Stannowski, B.; Lips, K.; Schmidt, T. W. *Australian Journal of Chemistry* **2012**, *65*, 480.
- (136) Zhou, J.; Liu, Q.; Feng, W.; Sun, Y.; Li, F. *Chemical reviews* **2014**, *115*, 395.
- (137) Park, Y. I.; Lee, K. T.; Suh, Y. D.; Hyeon, T. *Chem. Soc. Rev.* **2015**, *44*, 1302.
- (138) Helmchen, F.; Denk, W. *Nat Meth* **2005**, *2*, 932.
- (139) Auzel, F. *C. R. Acad. Sci. Paris* **1966**, *B262*, 1016.
- (140) Singh-Rachford, T. N.; Castellano, F. N. *Coord. Chem. Rev.* **2010**, *254*, 2560.
- (141) Yakutkin, V.; Aleshchenkov, S.; Chernov, S.; Miteva, T.; Nelles, G.; Cheprakov, A.; Balushev, S. *Chemistry-A European Journal* **2008**, *14*, 9846.
- (142) Alivisatos, A. P. *The Journal of Physical Chemistry* **1996**, *100*, 13226.
- (143) Monguzzi, A.; Mezyk, J.; Scotognella, F.; Tubino, R.; Meinardi, F. *Physical Review B* **2008**, *78*, 195112.
- (144) Lide, D. R. *CRC handbook of chemistry and physics*; CRC press, 2004.
- (145) Morris-Cohen, A. J.; Malicki, M.; Peterson, M. D.; Slavin, J. W. J.; Weiss, E. A. *Chemistry of Materials* **2013**, *25*, 1155.
- (146) Hens, Z.; Martins, J. C. *Chemistry of Materials* **2013**, *25*, 1211.
- (147) Turro, N. J.; Ramamurthy, V.; Scaiano, J. C.; Wiley Online Library: 2012.
- (148) Nirmal, M.; Norris, D. J.; Kuno, M.; Bawendi, M. G.; Efros, A. L.; Rosen, M. *Physical Review Letters* **1995**, *75*, 3728.
- (149) Kang, I.; Wise, F. W. *JOSA B* **1997**, *14*, 1632.
- (150) Galland, C.; Ghosh, Y.; Steinbruck, A.; Sykora, M.; Hollingsworth, J. A.; Klimov, V. I.; Htoon, H. *Nature* **2011**, *479*, 203.



- (151) Talapin, D. V.; Lee, J.-S.; Kovalenko, M. V.; Shevchenko, E. V. *Chemical Reviews* **2010**, *110*, 389.
- (152) Argeri, M.; Fraccarollo, A.; Grassi, F.; Marchese, L.; Cossi, M. *The Journal of Physical Chemistry C* **2011**, *115*, 11382.
- (153) Cossairt, B. M.; Juhas, P.; Billinge, S. J. L.; Owen, J. S. *The Journal of Physical Chemistry Letters* **2011**, *2*, 3075.
- (154) Hartmann, L.; Kumar, A.; Welker, M.; Fiore, A.; Julien-Rabant, C.; Gromova, M.; Bardet, M.; Reiss, P.; Baxter, P. N. W.; Chandezon, F.; Pansu, R. B. *ACS Nano* **2012**, *6*, 9033.
- (155) Hassinen, A.; Moreels, I.; De Nolf, K.; Smet, P. F.; Martins, J. C.; Hens, Z. *Journal of the American Chemical Society* **2012**, *134*, 20705.
- (156) Green, M. *Journal of Materials Chemistry* **2010**, *20*, 5797.
- (157) Guyot-Sionnest, P.; Wehrenberg, B.; Yu, D. *The Journal of chemical physics* **2005**, *123*, 074709.
- (158) Voznyy, O.; Zhitomirsky, D.; Stadler, P.; Ning, Z.; Hoogland, S.; Sargent, E. H. *ACS Nano* **2012**, *6*, 8448.
- (159) Ip, A. H.; Thon, S. M.; Hoogland, S.; Voznyy, O.; Zhitomirsky, D.; Debnath, R.; Levina, L.; Rollny, L. R.; Carey, G. H.; Fischer, A.; Kemp, K. W.; Kramer, I. J.; Ning, Z.; Labelle, A. J.; Chou, K. W.; Amassian, A.; Sargent, E. H. *Nat Nano* **2012**, *7*, 577.
- (160) Tang, J.; Kemp, K. W.; Hoogland, S.; Jeong, K. S.; Liu, H.; Levina, L.; Furukawa, M.; Wang, X.; Debnath, R.; Cha, D.; Chou, K. W.; Fischer, A.; Amassian, A.; Asbury, J. B.; Sargent, E. H. *Nat Mater* **2011**, *10*, 765.
- (161) Kim, D.; Kim, D.-H.; Lee, J.-H.; Grossman, J. C. *Physical Review Letters* **2013**, *110*, 196802.
- (162) Klimov, V. I. *Annu. Rev. Phys. Chem.* **2007**, *58*, 635.
- (163) Rabani, E.; Baer, R. *Nano letters* **2008**, *8*, 4488.
- (164) Cozzoli, P. D.; Pellegrino, T.; Manna, L. *Chemical Society Reviews* **2006**, *35*, 1195.
- (165) Colvin, V. L.; Schlamp, M. C.; Alivisatos, A. P. *Nature* **1994**, *370*, 354.

- (166) Kairdolf, B. A.; Smith, A. M.; Stokes, T. H.; Wang, M. D.; Young, A. N.; Nie, S. *Annual Review of Analytical Chemistry* **2013**, *6*, 143.
- (167) Carey, G. H.; Abdelhady, A. L.; Ning, Z.; Thon, S. M.; Bakr, O. M.; Sargent, E. H. *Chemical Reviews* **2015**, *115*, 12732.
- (168) Efros, A. L.; Rosen, M.; Kuno, M.; Nirmal, M.; Norris, D. J.; Bawendi, M. *Physical Review B* **1996**, *54*, 4843.
- (169) Zhu, H.; Lian, T. *Energy & Environmental Science* **2012**, *5*, 9406.
- (170) Hines, M. A.; Scholes, G. D. *Advanced Materials* **2003**, *15*, 1844.
- (171) Neo, D. C.; Cheng, C.; Stranks, S. D.; Fairclough, S. M.; Kim, J. S.; Kirkland, A. I.; Smith, J. M.; Snaith, H. J.; Assender, H. E.; Watt, A. A. *Chemistry of Materials* **2014**, *26*, 4004.
- (172) Yang, Y.; Rodríguez-Córdoba, W.; Lian, T. *Journal of the American Chemical Society* **2011**, *133*, 9246.
- (173) Shida, T.; Iwata, S. *Journal of the American Chemical Society* **1973**, *95*, 3473.
- (174) Kimura, K.; Yamazaki, T.; Katsumata, S. *The Journal of Physical Chemistry* **1971**, *75*, 1768.
- (175) Brodard, P.; Sarbach, A.; Gumy, J.-C.; Bally, T.; Vauthey, E. *The Journal of Physical Chemistry A* **2001**, *105*, 6594.
- (176) Green, M. A. *Third generation photovoltaics*; Springer, 2006.
- (177) Congreve, D. N.; Lee, J.; Thompson, N. J.; Hontz, E.; Yost, S. R.; Reuswig, P. D.; Bahlke, M. E.; Reineke, S.; Van Voorhis, T.; Baldo, M. A. *Science* **2013**, *340*, 334.
- (178) Tritsch, J. R.; Chan, W.-L.; Wu, X.; Monahan, N. R.; Zhu, X. *Nature communications* **2013**, *4*, 2679.
- (179) Lee, J.; Jadhav, P.; Reuswig, P. D.; Yost, S. R.; Thompson, N. J.; Congreve, D. N.; Hontz, E.; Van Voorhis, T.; Baldo, M. A. *Accounts of chemical research* **2013**, *46*, 1300.
- (180) Wu, T. C.; Thompson, N. J.; Congreve, D. N.; Hontz, E.; Yost, S. R.; Voorhis, T. V.; Baldo, M. A. *Applied Physics Letters* **2014**, *104*, 193901.

- (181) Jadhav, P. J.; Mohanty, A.; Sussman, J.; Lee, J.; Baldo, M. A. *Nano letters* **2011**, *11*, 1495.
- (182) Nienhaus, L.; Wu, M.; Geva, N.; Shepherd, J. J.; Wilson, M. W.; Bulović, V.; Van Voorhis, T.; Baldo, M. A.; Bawendi, M. G. *ACS nano* **2017**.
- (183) Clapp, A. R.; Medintz, I. L.; Mattoussi, H. *ChemPhysChem* **2006**, *7*, 47.
- (184) Rogach, A. L.; Klar, T. A.; Lupton, J. M.; Meijerink, A.; Feldmann, J. *Journal of Materials Chemistry* **2009**, *19*, 1208.
- (185) Li, X.; Nichols, V. M.; Zhou, D.; Lim, C.; Pau, G. S. H.; Bardeen, C. J.; Tang, M. L. *Nano Letters* **2014**, *14*, 3382.
- (186) Li, X.; Slyker, L. W.; Nichols, V. M.; Pau, G. S. H.; Bardeen, C. J.; Tang, M. L. *Journal of Physical Chemistry Letters* **2015**, *6*, 1709.
- (187) Anderson, N. C.; Hendricks, M. P.; Choi, J. J.; Owen, J. S. *Journal of the American Chemical Society* **2013**, *135*, 18536.
- (188) Werner, T.; Hercules, D. M. *The Journal of Physical Chemistry* **1969**, *73*, 2005.
- (189) Ghoneim, N.; Scherrer, D.; Suppan, P. *Journal of Luminescence* **1993**, *55*, 271.
- (190) Xu, C.; Liu, W.; Qin, W. *The Journal of Physical Chemistry A* **2011**, *115*, 4288.
- (191) Lee, S.; Arita, K.; Kajimoto, O.; Tamao, K. *The Journal of Physical Chemistry A* **1997**, *101*, 5228.
- (192) Kasha, M.; Rawls, H. R. *Photochemistry and Photobiology* **1968**, *7*, 561.
- (193) Lim, E. C.; Chakrabarti, S. K. *Chemical Physics Letters* **1967**, *1*, 28.
- (194) Adams, J. E.; Mantulin, W.; Huber, J. R. *Journal of the American Chemical Society* **1973**, *95*, 5477.
- (195) Stacy, W. T.; Swenberg, C. E. *The Journal of Chemical Physics* **1970**, *52*, 1962.
- (196) Shao, Y. *et al. Molecular Physics* **2015**, *113*, 184.

- (197) Chai, J.-D.; Head-Gordon, M. *Physical Chemistry Chemical Physics* **2008**, *10*, 6615.
- (198) Hirata, S.; Head-Gordon, M. *Chemical Physics Letters* **1999**, *314*, 291.
- (199) Querner, C.; Reiss, P.; Bleuse, J.; Pron, A. *Journal of the American Chemical Society* **2004**, *126*, 11574.
- (200) Behn, A.; Zimmerman, P. M.; Bell, A. T.; Head-Gordon, M. *The Journal of Chemical Physics* **2011**, *135*, 224108.
- (201) Levine, B. G.; Martínez, T. J. *Annual Review of Physical Chemistry* **2007**, *58*, 613.
- (202) Geva, N.; Shepherd, J. J.; Nienhaus, L.; Bawendi, M. G.; Van Voorhis, T. *arXiv preprint arXiv:1706.00844* **2017**.
- (203) Adamo, C.; Barone, V. *The Journal of Chemical Physics* **1999**, *110*, 6158.
- (204) Hay, P. J.; Wadt, W. R. *The Journal of Chemical Physics* **1985**, *82*, 299.
- (205) Haynes, W. M.; Taylor & Francis: 2016.
- (206) Kearvell, A.; Wilkinson, F. *Molecular Crystals* **1968**, *4*, 69.
- (207) Carbone, L.; Nobile, C.; Giorgi, M. D.; Sala, F. D.; Morello, G.; Pompa, P.; Hytch, M.; Snoeck, E.; Fiore, A.; Franchini, I. R.; Nadasan, M.; Silvestre, A. F.; Chiodo, L.; Kudera, S.; Cingolani, R.; Krahn, R.; Manna, L. *Nano Lett.* **2007**, *7*, 2942.
- (208) Lechner, R. T.; Fritz-Popovski, G.; Yarema, M.; Heiss, W.; Hoell, A.; Schulli, T. U.; Primetzhofer, D.; Eibelhuber, M.; Paris, O. *Chem. Mater.* **2014**, *26*, 5914.
- (209) Carbone, L.; Nobile, C.; De Giorgi, M.; Sala, F. D.; Morello, G.; Pompa, P.; Hytch, M.; Snoeck, E.; Fiore, A.; Franchini, I. R. *Nano letters* **2007**, *7*, 2942.
- (210) Chen, O.; Zhao, J.; Chauhan, V. P.; Cui, J.; Wong, C.; Harris, D. K.; Wei, H.; Han, H.-S.; Fukumura, D.; Jain, R. K.; Bawendi, M. G. *Nat Mater* **2013**, *12*, 445.
- (211) Dabbousi, B. O.; Rodriguez-Viejo, J.; Mikulec, F. V.; Heine, J. R.; Mattoussi, H.; Ober, R.; Jensen, K. F.; Bawendi, M. G. *The Journal of Physical Chemistry B* **1997**, *101*, 9463.

- (212) Yu, W. W.; Qu, L.; Guo, W.; Peng, X. *Chemistry of Materials* **2003**, *15*, 2854.
- (213) Hong, C.; Luo, W.; Yao, D.; Su, Y.-B.; Zhang, X.; Tian, R.-G.; Wang, C.-J. *Bioorganic & Medicinal Chemistry* **2014**, *22*, 3213.
- (214) Giarrusso, M. A.; Taylor, M. K.; Ziogas, J.; Brody, K. M.; Macdougall, P. E.; Schiesser, C. H. *Asian Journal of Organic Chemistry* **2012**, *1*, 274.
- (215) Cattani-Scholz, A.; Liao, K.-C.; Bora, A.; Pathak, A.; Hundschell, C.; Nickel, B.; Schwartz, J.; Abstreiter, G.; Tornow, M. *Langmuir* **2012**, *28*, 7889.
- (216) McDowell, M.; Hill, I. G.; McDermott, J. E.; Bernasek, S. L.; Schwartz, J. *Applied Physics Letters* **2006**, *88*, 073505.
- (217) Yamaguchi, I.; Higashi, H.; Shigesue, S.; Shingai, S.; Sato, M. *Tetrahedron Letters* **2007**, *48*, 7778.
- (218) Jetter, M. C.; Reitz, A. B. *Synthesis* **1998**, *1998*, 829.
- (219) Querner, C.; Benedetto, A.; Demadrille, R.; Rannou, P.; Reiss, P. *Chemistry of materials* **2006**, *18*, 4817.
- (220) Shu, C.; Chen, C.-B.; Chen, W.-X.; Ye, L.-W. *Organic letters* **2013**, *15*, 5542.
- (221) Liu, Y.; Liu, M.; Jen, A.-Y. *Acta polymerica* **1999**, *50*, 105.